IMPROVING AND EXPANDING PRECISION ORBIT DERIVED ATMOSPHERIC DENSITIES

BY

DHAVAL MYSORE KRISHNA

Submitted to the graduate degree program in Aerospace Engineering and the Graduate Faculty of the University of Kansas in partial fulfillment of the requirements for the degree of Master of Science.

_____

Chairperson: Dr. Craig A. McLaughlin

_____

Dr. Saeed Farokhi

_____

Dr. Ray Taghavi

Date Defended:

The Thesis Committee for Dhaval Mysore Krishna certifies that this is the approved version of the following thesis:

IMPROVING AND EXPANDING PRECISION ORBIT DERIVED ATMOSPHERIC DENSITIES

_____

Chairperson: Dr. Craig A. McLaughlin

Date approved:

ABSTRACT

Atmospheric drag is the most uncertain non-conservative force acting on a low Earth orbiting satellite. The existing atmospheric density models are not accurate enough to model the variations in density, which significantly affect the drag on satellites since drag is directly proportional to atmospheric density. In this research, precision orbit ephemerides (POE) are used as measurements in an optimal orbit determination scheme to estimate corrections to baseline atmospheric density models. These corrections improve the drag estimates, which in turn improve orbit determination and prediction and also provide a better understanding of the upper atmosphere.

The POE are used as measurements in a sequential measurement and filtering scheme using the Orbit Determination Tool Kit (ODTK) software, which provides the orbit determination. Five atmospheric density models are available in ODTK, which are used as baseline atmospheric density models to which corrections are made in the orbit determination. These density models are Jacchia 1971, Jacchia-Roberts, CIRA 1972, MSISE 1990, and NRLMSISE 2000. The user has the option to specify the ballistic coefficient (BC) correlated half-life and density correlated half-life. These half-lives are usually given values of 1.8, 18, or 180 minutes. If all five baseline density models are used along with three different combinations of ballistic coefficient and density correlated half-lives, then this would result in forty-five different cases. All the forty-five cases are examined in some studies and only a selected few are examined in others, the details of which are given in the appropriate sections.

The POE derived densities are validated by comparing them with accelerometer derived densities for satellites which have accelerometers onboard, such as the Challenging

Minisatellite Payload (CHAMP) and the Gravity Recovery and Climate Experiment (GRACE). The trend in the variation is compared quantitatively by calculating the cross correlation between the POE and accelerometer derived densities, and the magnitude is compared by calculating the root mean square between the two. The accelerometer derived densities for both CHAMP and GRACE are available from Sean Bruinsma of CNES and also from Eric Sutton of the United States Air Force Research Laboratory, and are used in this research.

The effect of different functions of geomagnetic planetary amplitude (a_p) as an input in orbit determination to estimate atmospheric density was investigated. The three different functions of input are 3-hourly a_p step functions, linear interpolated a_p functions, and a_p osculating spline functions. These three different types of functions were used as inputs for all the forty-five different combinations obtained by using the five different baseline atmospheric density models and three different combinations of ballistic coefficient and density correlated half-lives as stated earlier, and POE derived density was estimated for both CHAMP and GRACE. The POE derived densities were compared with the accelerometer derived densities by calculating the CC and RMS.

To create continuous data sets of POE derived densities that span a period of one week, the linear weighted blending technique was used to blend the 14 hour POE derived densities in their overlap periods. CIRA 1972 was used as the baseline atmospheric density model and a BC correlated half-life of 1.8 minutes and density correlated half-life of 180 minutes were used as inputs in ODTK to generate these POE derived density estimates. These one week continuous POE derived densities showed better correlation with accelerometer derived densities than HASDM densities for both CHAMP and GRACE.

The average cross-sectional area of the satellite that is normal to the velocity vector, the area facing the Sun, and the area facing the Earth, were determined so that these areas could be used to estimate the atmospheric drag, the force due to solar radiation pressure, and the force due to Earth radiation pressure (infrared and Earth albedo). This was done for both TerraSAR-X and ICESat.

For TerraSAR-X, the area normal to the velocity vector was assumed be a constant and equal to the frontal area, and the area facing the Earth was also assumed to be constant. However, the area facing the Sun varied with time. The average area facing the Sun for a period of 14 hours and also the annual average area were calculated and used to calculate the POE derived densities. The POE derived densities calculated using these two different average areas facing the Sun were found to be very similar. Since TerraSAR-X does not have an accelerometer onboard, the POE derived densities could not be compared with accelerometer derived densities, but instead were compared with Jacchia-71 densities since this was also one of the outputs from ODTK. The POE derived densities were also compared with NRLMSISE 2000 densities.

The attitude of ICESat as a function of beta angle was given in the literature and so was the average area of each side of the satellite when it was modeled as a rectangular box with two solar panels. This information was used to estimate the 30-hour average area normal to the velocity vector, area facing the Earth, and area facing the Sun, for ICESat. The POE derived densities using these areas were estimated by ODTK and compared with the Jacchai-71 density model.

ACKNOWLEDGEMENTS

I would like to thank Dr. Craig A. McLaughlin for providing me the opportunity to work on this research and for his constant guidance and patience throughout this research. I am very thankful to Dr. Saeed Farokhi and Dr. Ray Taghavi for being my thesis committee members.

This research is based upon work supported by the National Science Foundation under Grant No. 0832900 at the University of Kansas, Department of Aerospace Engineering. I wish to thank Jens Ramrath, Jim Wright, Jim Woodburn, and John Seago for help with this research and with Orbit Determination Tool Kit. David Vallado provided help with data conversion and ODTK. I also wish to thank Chris Sabol, Matt Wilkins, and Paul Cefola for discussions related to this work. Thanks to Bruce Bowman for access to HASDM densities. Sean Bruinsma, Jeff Forbes, and Eric Sutton provided accelerometer derived densities for CHAMP and GRACE.

I am thankful to my research predecessors Andrew Hiatt, Travis Lechtenberg, Eric Fattig, and Anoop Arudra for building a foundation for this research. I am also thankful to my current research colleagues, Travis Locke and Piyush Mehta, for their help in my research.

TABLE OF CONTENTS

NOMENCLATURE

Latin Symbol	Description	Units
A	Cross sectional Area	m^2
A_p	Geomagnetic daily planetary amplitude	gamma, 10^{-9} Telsa
a	Semi-major axis	km
$\vec{a}_{drag}$	Acceleration vector due to atmospheric drag	m/s^2
a_p	Geomagnetic 3-hourly planetary amplitude	gamma, 10^{-9} Telsa
apex	Satellite apex position	deg
$\Delta B/B$	Estimated ballistic coefficient correction	~
BC	Ballistic coefficient	m^2/kg
C_D	Satellite drag coefficient	~
$F_{10.7}$	Daily solar radio flux measured at 10.7 cm wavelength	SFU
$\bar{F}_{10.7}$	$F_{10.7}$ running 81-day centered smoothed data set	SFU
g_o	Gravitational acceleration	m/s^2
Δh	Altitude change	m
i	Inclination	deg
K_p	Geomagnetic planetary index	~
M	Mean molecular mass	amu
m	Satellite mass	kg
N	Number of elements	~
$\vec{n}$	Geodetic-nadir pointing vector	m

Δp	Atmospheric pressure change	N/m^2
p_o	Absolute pressure	N/m^2
$\hat{P}$	Filter covariance matrix	~
$\tilde{P}$	Smoother covariance matrix	~
$\bar{P}$	Differenced covariance matrix	~
R	Universal gas constant	$J\ K^{-1}\ mol^{-1}$
$\bar{R}$	McReynold's consistency test ratio	~
$\vec{r}$	Satellite position vector	m
t	Time	s
T	Temperature	K
u	Argument of latitude	
v_{rel}	Satellite velocity magnitude relative to Earth's atmosphere	m/s
$\vec{v}_{rel}$	Satellite velocity vector relative to Earth's atmosphere	m/s
$w(t)$	Gaussian white random variable	~
X	Satellite state vector	~
$\bar{X}$	Difference state vector	~
$\hat{X}$	filter state estimate	~
$\tilde{X}$	Smoother state estimate	~
$\bar{\bar{X}}$	Difference between filter and smoother state estimate	~
x	X component of satellite position vector	m
x	Gauss-Markov process dynamic scalar random variable	~

x	Cross correlation series	~
y	Y component of satellite position vector	m
y	Cross correlation series	~
Δy	Measurement residual	~
z	Z component of satellite position vector	m

Greek Symbol	**Description**	**Units**
α	Gauss-Markov process variable	~
β	Solar Beta Angle	deg
β'	Solar Beta Angle	deg
ζ	Angle of rotation of solar array	deg
ρ	Atmospheric density	kg/m^3
$\Delta\rho/\rho$	Estimated atmospheric density correction	~
$\vec{\sigma}$	Denominator for McReynold's consistency test ratio	~
σ_w^2	Variance of Gaussian white random variable	~
τ	User defined correlated half-life	minutes
φ_b	Pitch bias	rad
Φ	Transition function	~
ψ	Yaw angle	deg
Ω	Right ascension of the ascending node	deg
$\omega_\oplus$	Earth's angular velocity magnitude	rad/s

$\vec{\omega}_{\oplus}$	Earth's angular velocity vector	rad/s

Abbreviation/Acronym	**Definition**
AFSC	Air Force Space Command
ANDE	Atmospheric Neutral Density Experiment
BATC	Ball Aerospace and Technologies Corporation
CC	Cross Correlation
CHAMP	Challenging Minisatellite Payload
CIRA	COSPAR International Reference Atmosphere
CM	Center of Mass
COSPAR	Committee on Space Research
CNES	Centre National d'Études Spatiales
DCA	Dynamic Calibration of the Atmosphere
DORIS	Doppler Orbitography by Radiopositioning Integrated on Satellite
DTM	Drag Temperature Model
ESA	European Space Agency
EUV	Extreme Ultra-Violet
GCRF	Geocentric Celestial Reference Frame
GEOSAT	Geodetic Satellite
GFO	GEOSAT Follow-On
GLAS	Geoscience Laser Altimeter System

GPS	Global Positioning System
GRACE	Gravity Recovery And Climate Experiment
GSFC	Goddard Space Flight Center
HASDM	High Accuracy Satellite Drag Model
ICESat	Ice, Cloud, and Land Elevation Satellite
ICRF	International Celestial Reference Frame
JPL	Jet Propulsion Laboratory
LVLH	Local-vertical local-horizontal
MSISE	Mass Spectrometer Incoherent Scatter Extending from ground to space
NASA	National Aeronautics and Space Administration
NOAA	National Oceanic and Atmospheric Administration
NORAD	North American Aerospace Defense Command
NRL	Naval Research Laboratory
NRLMSISE	Naval Research Laboratory Mass Spectrometer Incoherent Scatter Extending from ground to space
ODTK	Orbit Determination Tool Kit
POD	Precision Orbit Determination
POE	Precision Orbit Ephemerides
PSO	Precision Science Orbit
RMS	Root Mean Square
RSO	Rapid Science Orbit
SAR	Synthetic Aperture Radar

SCS	Satellite Coordinate System
SETA	Satellite Electrostatic Triaxial Accelerometer
SFU	Solar Flux Units
SLR	Satellite Laser Ranging
STAR	Spatial Triaxial Accelerometer for Research
TanDEM-X	TerraSAR-X add on Digital Elevation Measurement
TLE	Two Line Element
TOO	Target of Opportunity
TSS	Thermal Synthesizer System

LIST OF FIGURES

LIST OF TABLES

1 INTRODUCTION

1.1 Objective

The objective of this research is to estimate corrections to existing atmospheric density models using orbit determination of low Earth orbit satellites. After these corrections are implemented, the density estimated by the models will be more accurate, which will improve the results of satellite drag calculations, improve orbit determination and prediction, and also help in better understanding of the atmospheric density in the thermosphere and exosphere. This research focuses on the short term variations of the atmospheric density due to solar and geomagnetic effects. The procedure for approximate attitude determination of two satellites, which are required for atmospheric drag and radiation force modeling are also examined.

1.2 Motivation

The atmospheric density is more variable than predicted by existing atmospheric density models. Therefore, the density estimated by these models when used to calculate the drag forces for orbit prediction results in significant errors.

Of all the non-conservative forces acting on low Earth orbit satellites, atmospheric drag is the most dominant, and also the most uncertain. This uncertainty in atmospheric drag force is primarily because the existing atmospheric density models are not accurate. Since the drag force is directly related to the atmospheric density, the influence of the latter becomes more important at lower altitudes, larger frontal area of the satellites, and lower satellite mass. Accurate estimation of atmospheric density is required for better prediction of the effect of satellite drag on satellite motion.

Atmospheric density and its variations are mostly influenced by the Sun. The Sun affects the density in two ways. The first is by direct heating of the atmosphere by the rays of the Sun in the extreme ultraviolet region. The second is through the charged particles ejected from the Sun, which interact with the magnetic field of the Earth and heat up the atmosphere upon contact. The current density models require some kind of input measurements of the Sun's electromagnetic radiation and the Earth's magnetic field to estimate the density. These measurements are available as averages taken over a day, or every 3 hours, and are global values. The time scale of these measurements are too large and thus the models fail to estimate the short term variations in the density, the knowledge of which is required for accurate satellite drag prediction.

Thus, the existing density models require corrections for high accurate orbit determination and predictions, as well as better understanding of the thermosphere and exosphere density variations. The corrections are estimated using precision orbit determination (POD). The results are then compared with actual values of density. Since no such "real" or actual measurements exist for density, the density derived from accelerometer measurements present on board certain satellites are used as the true value of densities. For the Challenging Minisatellite Payload (CHAMP) satellite, the accelerometer present on board, called the Spatial Triaxial Accelerometer for Research (STAR), is used to measure the non-conservative accelerations acting on the satellite. Sean Bruinsma at the Centre National d'Etudes Spatiales (CNES) has derived the density along the path of CHAMP using the accelerometer

measurements[*] [Ref.1], and Eric Sutton[†] from the United States Air Force Research Laboratory has also obtained density from the measurements from STAR [Ref. 2]. Accelerometer density for the Gravity Recovery And Climate Experiment (GRACE) is also obtained in this way [Ref. 3]. The accelerometer density for both CHAMP and GRACE are also compared with the density from the High Accuracy Satellite Drag Model (HASDM) obtained by Bruce Bowman[‡] of U. S. Air Force Space Command.

These corrected density values are then used in the drag equation to provide improved drag estimates. Thus, better density estimates result in better drag estimates, and since in low Earth orbit atmospheric drag is the most dominant non-conservative force, a better drag estimate results in better orbit determination and prediction. These in turn lead to improved accuracy in estimating the satellite lifetime, prediction of the time of reentry, and future state of the satellite. A more accurate value of atmospheric density will also help understand the effect of space environment and weather on atmospheric density and its variation.

1.3 Satellite Drag

Atmospheric drag is the third most dominant force acting on a low Earth orbiting satellite (depending on the altitude in low Earth orbit), after the forces due to central body and oblateness of the Earth. For satellites orbiting at higher altitudes, radiation pressure due to the Sun as well as third body effects become significant and dominant as well. Apart from the undesirable effects of satellite drag, other applications such as aerobraking and space tethers

[*] Sean Bruinsma shared the accelerometer derived density data with Dr. Craig A. McLaughlin, Assistant Professor, University of Kansas.

[†] Eric Sutton shared the accelerometer derived density data with Dr. Craig A. McLaughlin, Assistant Professor, University of Kansas.

[‡] Bruce Bowman shared the HASDM density data with Dr. Craig A. McLaughlin, Assistant Professor, University of Kansas.

require an accurate model of the atmosphere for high accuracy solutions. The three main areas under which drag is studied are for orbit determination under the influence of drag, satellite lifetime estimation, and to determine the physical properties of the upper atmosphere [Ref. 4].

When a satellite encounters atmospheric molecules, it experiences a retarding force, the drag force, due to momentum transfer from the latter. This results in a loss of energy of the satellite and thus drag is a non-conservative force. Other non-conservative forces acting on the satellite include the radiation forces due to the Sun, Earth albedo, and Earth infrared. The effect of the drag is to reduce the semimajor axis (due to loss of energy) and the eccentricity (making it less elliptical). Other orbital elements are also affected by drag but the effects are periodic in nature. Drag also results in some coupling effects with the aspherical potential.

According to Reference 4, the need for a rigorous model of the effects of atmospheric perturbations requires knowledge in the fields of molecular chemistry, thermodynamics, aerodynamics, hypersonics, meteorology, electromagnetics, planetary science, and orbital mechanics. Thus, study of astrodynamics in the presence of the atmosphere is very difficult. Nevertheless, accurate determination of atmospheric properties is essential for satellite drag studies.

The acceleration experienced by a satellite is given by the following equation, which relates the acceleration with atmospheric properties, geometrical properties of the satellite, and the relative velocity vector of the satellite [Ref. 4].

$$\vec{a}_{drag} = -\frac{1}{2}\frac{C_D A}{m}\rho v_{rel}^2 \frac{\vec{v}_{rel}}{|\vec{v}_{rel}|} \tag{1.1}$$

The first quantity in the above drag equation, C_D is the coefficient of drag, a dimensionless quantity which quantifies the resistance of a body. C_D depends on the temperature and

composition of the surrounding atmosphere, surface properties of the satellite including its temperature, surface geometry, and orientation. The drag coefficient for a flat plate is about 2.2 and about 2.0 to 2.1 for spheres, in the upper atmosphere [Ref. 4]. C_D is usually estimated up to three significant digits. ρ is the atmospheric density, which is the hardest to estimate. Several atmospheric models exist which are used to estimate neutral density, whose details will be discussed in future sections. A is the cross sectional area that is normal to the velocity vector. For a satellite whose attitude and geometry are known, determining A may be relatively easy. However, if the attitude of an aspherical satellite is not known, then determining the cross sectional area becomes difficult, especially if the satellite's attitude is rapidly changing, say a tumbling satellite. m is the mass of the satellite. The mass may be constant or changing during the mission depending on whether the onboard propellants (if any) are being consumed. $\vec{v}_{rel}$ is the velocity vector of the satellite relative to the atmosphere and v_{rel} is its magnitude.

The quantity $m/C_D A$ is called the ballistic coefficient (BC), which is another measure of a satellites susceptibility to drag. Higher BC means lower drag is experienced by the satellite. This is the traditional definition of the BC. In this research, the BC is defined as the inverse or the reciprocal of the conventional definition of the BC. Thus BC in this research refers to $C_D A/m$. In order to avoid ambiguity, this will be called as the inverse BC. Thus, higher the inverse BC means higher drag is experienced by the satellite.

The atmosphere is not stationary in the inertial frame but rotates with the Earth. However, the rotational rate is not the same as that of the Earth at higher altitudes but rather rotates with a profile; so the layer next to the surface has the same rotational speed as that of the Earth, and the ones above gradually decrease in speed. Often, this lag is ignored and the

atmosphere layer at the satellite altitude is assumed to rotate at the same rate as the surface of the Earth. Using this approximation, the expression for the relative velocity of the satellite in the inertial frame is give in Reference 4 and reproduced below.

$$\vec{v}_{rel} = \frac{d\vec{r}}{dt} - \vec{\omega}_{\oplus} \times \vec{r} = \left[\frac{dx}{dt} + \omega_{\oplus} y \quad \frac{dx}{dt} - \omega_{\oplus} x \quad \frac{dx}{dt} \right]^T \tag{1.2}$$

In the above equation, $\vec{r}$ is satellite position vector with x, y, and z components. $\vec{\omega}_{\oplus}$ is the angular velocity vector of the Earth and $\omega_{\oplus}$ is its magnitude. The above equation does not take into account the winds. In reality, winds are superimposed on the rotating motion of the atmosphere. The expressions involving winds are not discussed in this section, and several applications do not consider the effect of wind because information or measurements of additional parameters required for wind calculations are not available.

As mentioned earlier, atmospheric density is perhaps the hardest to estimate in the expression to calculate the drag. Because of complex interactions between three basic parameters, which are, the nature of the atmosphere's molecular composition, the incident solar flux, and geomagnetic interactions, the density in the upper atmosphere changes [Ref. 4]. The molecular composition indeed affects the atmospheric density as given by the ideal gas equation, discussed later in this section. The incident solar flux in the extreme ultraviolet (EUV) region heats the atmosphere directly and the effect is instantaneous. Due to geomagnetic activity, charged particles collide with the atmosphere and heat it up, resulting in delayed heating of the atmosphere. Since both of these heat up the atmosphere, this results in an expansion of the atmosphere because heating a gas at constant pressure increases its volume [Ref. 5]. This expansion causes the density to increase at higher altitudes.

Static and time-varying models are based on a few basic hydrostatic principles, and two such relations used are the ideal-gas law and the hydrostatic equation. The ideal-gas law relates the pressure, p, density, ρ, mean molecular mass of the gas mixture, M, and temperature, T, through the universal gas constant, R. The equation is given in Reference 4 and reproduced below.

$$\rho = \frac{pM}{RT} \tag{1.3}$$

The hydrostatic equation gives the relation of the change in pressure with the change in altitude. This relation is given in Reference 4 and reproduced below.

$$\Delta p = -\rho g \Delta h \tag{1.4}$$

These equations are used to develop atmospheric density models. The models can be broadly classified into two categories, static models and time-varying models. The static models are the simplest but least accurate because they do not take into account the density variations with respect to time. The time-varying models are more complex but most accurate since they take into account several time varying parameters which affect the density. Since orbit determination and prediction demands accurate drag modeling and thus accurate density models, time-varying models are required.

1.4 Neutral Atmosphere

The structure of the atmosphere is discussed first and then the characteristics of the two different types of atmospheric models–static atmospheric models and time varying atmospheric models–are discussed next. The structure of the atmosphere discussed here is derived from Reference 5 and 6.

1.4.1 Structure of the Neutral Atmosphere

The atmosphere is classified into different altitude regions or bands, called “spheres”, where each sphere can be thought of as a concentric shell of atmosphere with a thickness of tens of hundreds of kilometers depending on the sphere. The upper boundary of each of these spheres is termed a “pause”, and these boundaries vary over tens of kilometers. The figure below shows the various spheres of the atmosphere.

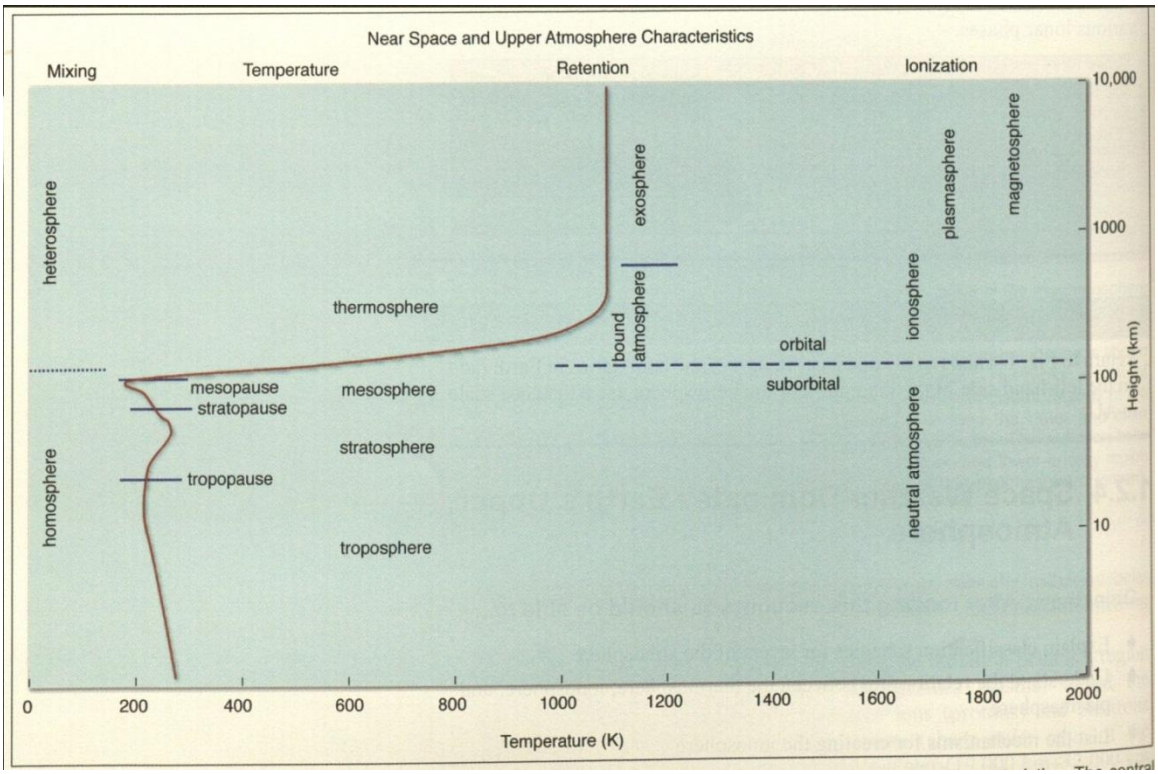

Figure 1.1: Layers of Atmosphere [Ref. 6].

The layer right above the Earth’s surface is the troposphere, which is characterized by decrease in temperature with increase in the altitude. This layer extends from the ground up to about 11 to 12 km, and the upper boundary is called the tropopause. The next layer is the stratosphere, which extends to about 45 km. The stratosphere is characterized by increasing temperature because the ozone present in this layer absorbs the incoming UV rays and this

heats up the layer. The next layer is the mesosphere, which extends from the stratopause to the mesopause, which is at an altitude of about 85 km. This region is characterized by decreasing temperature and reaches a low of about 180 K. This region is well above the reaches of high altitude balloon and too low for low Earth orbiting satellites.

Above the mesopause lies the thermosphere, so called because of the increasing temperature with altitude. This region extends up to about 600 km, and is the region where some of the low Earth orbiting satellites orbit and is thus of interest to orbit determination. This layer is the most absorptive layer in the atmosphere and hence absorbs solar UV and this heats up the layer resulting in an increase in temperature. This solar UV absorption causes destruction of ozone molecules and also splitting of oxygen molecules into atomic oxygen. Above the thermosphere lies the exosphere, where the density is so low that the molecules travel in ballistic trajectories influenced only by gravitational forces. The temperature of the exosphere is almost constant and equal to the asymptotic temperature that is reached toward the upper boundary of the thermosphere - the thermopause.

Nitrogen molecules are the dominant constituent from the ground up to about 175 km. Then atomic oxygen takes over as the most dominant species till about 600 km. Higher up, helium becomes the most prevalent molecule from about 650 km to 2,500 km, after which hydrogen becomes abundant above 2,500 km [Ref. 7].

1.4.2 Static Atmospheric Models

Even though static models are simple, since they do not consider variations of parameters with respect to time, there are certain changes that they do take into account. They are latitudinal variations and longitudinal variations.

An easy way to visualize latitudinal variations is to consider a circular orbit, inclined at an angle with respect to the equator. As the satellite travels along its orbit, it passes through different latitudes and since the Earth is not a perfect sphere but more of an oblate spheroid, the satellite encounters varying altitude as it passes through different latitudes. Thus, the satellite encounters different density along its trajectory and the drag varies accordingly.

The longitudinal variations are mainly due to the variation in local time (position of the Sun with respect to the surface of the Earth) and thus are not considered in static models. However, the atmosphere is not symmetrical about the axis of rotation because of the presence of different geological features such as the mountain ranges, oceans, and because of wind and temperature differences, which cause differences in atmospheric density and thus the drag experienced by the satellite as it moves through different longitudes.

1.4.3 Time Varying Atmospheric Models

Time varying models, though complex, take many time varying parameters into consideration. The variations in atmospheric properties are mostly influenced by the Sun–both by direct heating as well as through interaction of the charged particles emitted by the Sun with the Earth's atmosphere. The time varying effects must model the following real-world effects, which are derived from References 4 and 7.

i. Diurnal Variations
ii. Carrington Cycle
iii. 11 year Sunspot Cycle
iv. Semi-annual/Seasonal Variations
v. Cyclical Variations

vi. Rotating Atmosphere

vii. Winds

viii. Magnetic-storm Variations

ix. Irregular short-period variations

x. Tides

xi. Gravity Waves

Diurnal variations: This variation is due to the rotation of the Earth, which causes a bulge in the atmosphere on the Sun facing side (day time) and a depression in the opposite hemisphere (night time). But this bulge on the day time does not occur on the meridian exactly below the Sun, but lags it so that the bulge occurs at a local time of 2 to 2:30 PM. Depending on the season (and thus the Sun's declination), the bulge occurs at different latitude, and it occurs on the equator only during the equinoxes. Likewise, the minimum occurs at around 4:00 AM local time.

Carrington Cycle or 27-day cycle: The Sun rotates about its axis with an average period of about 27 days. This causes a change in the radio flux in the decimeter wavelength due to growth and decay of active solar regions. Uncertainty in determination of the pattern of these active regions makes the prediction of solar-flux harder.

11 year sunspot Cycle: Sunspots and solar flux undergo an 11 year cycle where they go from minimum to maximum and back again. During solar maximum, the solar flux is intense and the atmospheric density is higher and so are the variations, thus the variations are difficult to predict.

Semi-annual/Seasonal Variations: As the name suggests, these variations exist for about six months and this is because of the varying distance of the Earth from the Sun and also due to

variation in the declination of the Sun. The effect of this on Earth's atmosphere is usually small.

Cyclical Variations: There is another 11 year cycle, which parallels the 11 year sunspot cycle but lags behind the latter. Unlike the sunspot cycle, this 11 year cycle takes about 6-7 years to go from a minimum to a maximum, thus the minimum of this cycle is not exactly half way between two maxima. Even though the exact cause of this 11 year cycle is unknown, the sunspot activity is the most likely suspect.

Rotating atmosphere: As mentioned before, the atmosphere is not stationary in inertial space but rather rotates with the Earth. The layer closest to the surface rotates at about the same speed as Earth and the layers above these rotate at a lower speed and this creates a profile. This rotation causes variation in the density.

Winds: Winds at high altitudes cause variations in the temperature and thus in density too. Accounting for such winds in models is very difficult and complex. The dynamics of the upper atmosphere is not completely understood and requires further study.

Magnetic-storm variations: Changes in the atmosphere can be caused by variations in the Earth's magnetic field. These changes are usually small unless geomagnetic activity increases.

Irregular short-periodic variations: The causes for small short periodic variations are associated with various phenomena such as transient geomagnetic disturbances, solar flares, variation in hydrogen currents within the atmosphere.

Tides: Small variations in atmospheric density are caused by both ocean tides and atmospheric tides. Also, tides driven by solar heating cause diurnal tidal components that can reach a velocity upto 200 m/s.

Gravity Waves: Gravity waves transfer or propagate disturbances from the lower atmosphere to the upper atmosphere. These waves transfer energy from the lower to upper atmosphere–mostly the mesosphere and lower thermosphere. At higher altitudes, these waves die out due to viscous damping. This transfer of energy causes variation in the density.

1.5 Atmospheric Density Models

Several atmospheric density models exist today and some of them have been developed over the past few decades, and they have undergone several revisions to include new information and to make them more accurate. These models are developed using two main approaches. The first one is by combining conservation laws and atmospheric-constituent models into a physical model; the second one is by using simplified physical concepts that are developed from in-situ measurements and satellite-tracking data. The heritage of some of the models in a chronological order is shown in a figure in Reference 4 and reproduced below.

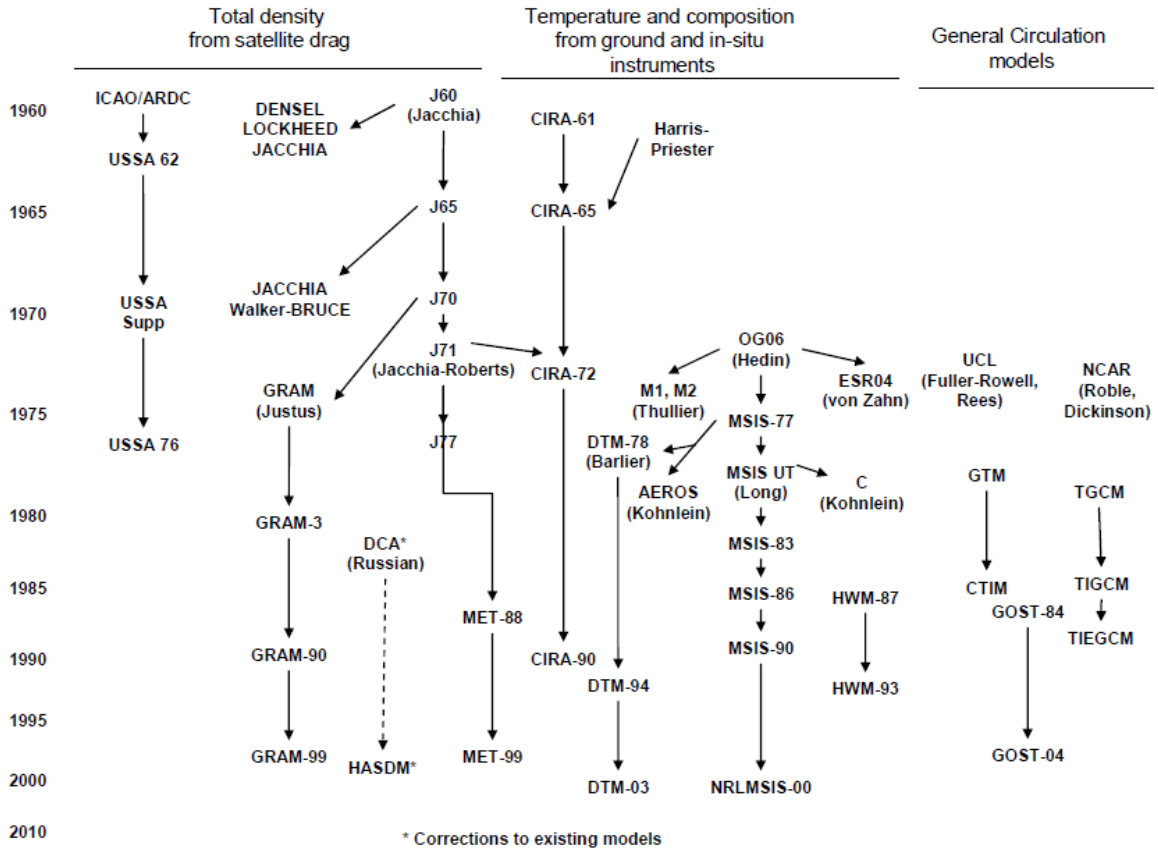

Figure 1.2: Development of atmospheric models shown with a timeline [Ref. 4].

Since orbit determination demands high accuracy models, time-varying models are to be used even though computational requirements are high. High fidelity models may demand high computational power, but they are most complete and need accurate data. Of several models available, no one model can be picked as the best, because each model will have some errors because of some physical reasons. Thus, a model is picked depending on the application and one that yields a best combination of speed, accuracy, and applicability.

Only the models that are used in this research are briefly discussed in this section. They are Jacchia 1971 [Ref.8], Jacchia-Roberts [Ref.9], Committee On Space Research (COSPAR) International Reference Atmosphere (CIRA-1972) [Ref.10], Mass Spectrometer Incohorent Scatter Extended (MSISE-1990) [Ref.11], and Naval Research Laboratory Mass Spectrometer

Incoherent Scatter Extended (NRLMSISE-2000) [Ref.12]. Each of these models is briefly described in the following subsections. But before that, a brief discussion of the solar and geomagnetic indices is presented, which is mostly from Reference 4.

1.5.1 Solar and Geomagnetic Indices

The main influence of the Sun on the Earth's atmospheric density is through direct heating by incoming solar radiation. The incoming solar radiation in Extreme Ultraviolet (EUV) heats up the upper atmosphere and causes it to expand, thus increasing the density. EUV cannot be measured from the Earth's surface since it is absorbed by the Earth's atmosphere. Thus, earlier models (including all the models that are used in this research and listed previously in the same section) were not modeled to use the EUV flux as one of their input parameters. Instead, they use a proxy solar flux with a wavelength of 10.7 cm ($F_{10.7}$) because scientists have determined that both EUV and 10.7 cm wavelength solar flux originate in the same layers of the Sun's chromospheres and corona, and also because Earth's atmosphere is transparent to $F_{10.7}$ radiation. Measurements of $F_{10.7}$ have existed since 1940 and these measurements are in Solar Flux Units (SFU), where one SFU is equal to 10^{-22} watt/m^2/Hz. The values of SFU can range anywhere from less than 70 to more than 300. The National Oceanic and Atmospheric Administration (NOAA) at the National Geophysical Data Center in Boulder, Colorado, distributes daily values of $F_{10.7}$, 81-day centered running average, $\bar{F}_{10.7}$, as well as other forms. The EUV flux is now measured by satellites and thus can be used directly in atmospheric models. Jacchia-Bowman 2006 [Ref.13] and a new revised version Jacchia-Bowman 2008 [Ref.14] are two such models which incorporate these new indices.

Magnetic variations of both the Sun and the Earth are related to variations in the Earth's atmospheric density. Magnetic disturbances cause charged particles to ionize the upper atmosphere, which changes the density and thus the satellite drag. When the solar wind interacting with the Earth's geomagnetic field collides with air molecules, the atmosphere gets heated up. Thus, it is essential to measure the geomagnetic activity so that a quantitative correlation can be obtained between the geomagnetic activity and the heat generated. The average geomagnetic activity below the auroral zones is measured by a quasi-logarithmic quantity or index called the geomagnetic planetary index, K_p, which is a global average. To get this global average, twelve stations around the world (which lie between 48 deg. N and 63 deg. S latitudes), each calculate their respective local values of geomagnetic index, K, once every three hours. These values are then used, along with latitude corrections to calculate the global average, K_p. K_p varies between 0.0 (low activity) to 9.0 (extreme geomagnetic activity), and is presented to the nearest third of an integer. Since K_p is quasi-logarithmic, a quantity called the geomagnetic planetary amplitude, a_p, is derived, which is a linear version of K_p. While some atmospheric density models such as Jacchia-Roberts use K_p as an input, others use a_p. The daily planetary amplitude, A_p is the average of a_p taken over the whole day. Since K_p (and therefore a_p) is measured once every 3 hours, there are eight global average values in a day, and the average of these eight values of a_p will be A_p. The unit of daily planetary amplitude is gamma, where one gamma is equal to 10^{-9} Telsa. The value of A_p ranges from 0 to 400, with 10-20 being the average and anything above 100 being rare. The trend in the variation of A_p follows the 11 year sunspot cycle and the semi-annual cycle, and any variation is due to solar flares, coronal holes, disappearing solar filaments, and the solar wind environment near the Earth.

Depending on the value of $F_{10.7}$ and A_p, solar and geomagnetic activity can be divided into different bins based on Picone et al.[Ref. 12]. These bins along with their respective range of solar and geomagnetic activity are shown in the table below.

Table 1.1: Solar and Geomagnetic activity bin definition.

Activity Bin	Definition Bin
Low Solar	$F_{10.7} < 75$
Moderate Solar	$75 \leq F_{10.7} < 150$
Elevated Solar	$150 \leq F_{10.7} < 190$
High Solar	$F_{10.7} \geq 190$
Quiet Geomagnetic	$A_p \leq 10$
Moderate Geomagnetic	$10 < A_p < 50$
Active Geomagnetic	$A_p \geq 50$

1.5.2 Jacchia 1971 Atmospheric Model

This is a revision of the Jacchia 1970 model, but includes more recent data and mass-spectrometer and EUV-absorption data. The procedure to calculate the density is very similar to that of the previous Jacchia model, by numerically integrating either the barometric equation or the diffusion equation, depending on the altitude. In the Jacchia 1970 model, the barometric equation is used when the altitude is between 90 km (at which the boundary conditions are specified) up to a 105 km, and the diffusion equation is used from 105 km and above. While in the Jacchia 1971 model, the barometric equation is used between 90 to 100 km, and diffusion equation above 100 km. Thus based on the equations used to obtain the density, the atmosphere in the Jacchia 1971 model can be divided into two regions, the lower region which is between 90 to 100 km, and the upper region above 100 km. However, based on the equations used to

calculate the temperature profile (thermosphere temperature), the lower region is between 90 to 125 km and the upper region is above 125 km. This is because at 125 km, there is an inflection in the temperature profile, and the temperature at this inflection point is a function of the exospheric temperature. Above this inflection point, an inverse tangent function is used for the temperature profile. Thus taking both the density and temperature criteria, one can say that the atmosphere in Jacchia's model is divided into three regions, the first one from 90 to 100 km, the second one from 100 to 125 km, and the last one above 125 km. Density from 0 to 90 km is mostly used for reentry studies and not considered in Jacchia's models, other than the fact that he assumed the composition of the individual species at 90 km to be same as that at the sea level.

The other differences between the Jacchia 1970 model and Jacchia 1971 model are in the equations that are used to calculate the average molecular mass of the atmosphere at altitudes below 100 km, equations to calculate the thermosphere temperature at the inflection height of 125 km, the equations to calculate the global exospheric temperatures, and a few others. The general procedure to calculate the atmospheric density using the Jacchia 1971 model is briefly explained below. This procedure is similar for all the Jacchia family models (Jacchia 1971, Jacchia-Roberts, CIRA 1972, Jacchia-Bowman 2006, Jacchia-Bowman 2008) and the differences are mainly in the way the exospheric temperature is calculated and other small differences in the calculations of corrections to density.

Before calculating the mass density or the density of the individual constituents, the first step is to calculate the exospheric temperature. The Jacchia 1971 model paper [Ref.8] recognizes the dependence of atmospheric properties (and also the exospheric temperature) on various phenomena, which are used to determine the exospheric temperature. The phenomena

are classified into: variations with the solar cycle, variations with the daily change in the activity on the solar disk, the diurnal variation, variations with the geomagnetic activity, the semiannual variation, seasonal-latitudinal variations of the lower thermosphere, seasonal-latitudinal variations of helium, and rapid density fluctuations probably connected with gravity waves. The variation in the solar activity is accounted for by calculating the global nighttime minimum exospheric temperature as a function of the 81-day running centered average of $F_{10.7}$, $\bar{F}_{10.7}$; provided that the geomagnetic planetary index, K_p is zero. Even if K_p is not zero, the geomagnetic effect on the exospheric temperature will be accounted for later. The reason for using $\bar{F}_{10.7}$ is to average out the differences caused by the solar-rotation cycle (Carrington cycle of 27 day), so $\bar{F}_{10.7}$ includes three rotations. Equations are used to correct global nighttime exospheric temperature to take into account the diurnal variations. The effect of geomagnetic activity is considered by calculating a correction temperature (and a density too) as a function of geomagnetic planetary index, Kp, and its 0.4 day mean, depending on the altitude. Unlike the previous Jacchia 1970 model, the semiannual variations for the Jacchia 1971 model are directly applied to the density and no corrections for the exospheric temperature are made. With all these, the exospheric temperature is calculated, and this in turn is used to calculate the temperature at the inflection point (altitude of 125 km), which provides the thermosphere temperature profiles using two different equations–one for below 125 km and the other for above 125 km. Now these thermospheric temperatures are used to calculate the mass density. For altitudes below 100 km, the mean molecular mass is calculated as a function of altitude only and then this, along with the temperature, is used to numerically integrate the barometric equation to obtain the mass density. For altitudes above 100 km, the diffusion equation is

numerically integrated to obtain the number density of the individual species, which are then used to get the mass density of the individual species, the summation of which gives the total mass density of the atmosphere at that altitude. Below 500 km, the number density of hydrogen is taken equal to zero, and above 500 km it is calculated and contributes to the total atmospheric density. Corrections to density such as the semiannual corrections, corrections due to seasonal-latitudinal variations of the lower thermosphere, and corrections due to seasonal-latitudinal variation of Helium are added. For more details, the reader is encouraged to refer to the Jacchia 1971 paper [Ref.8].

1.5.3 Jacchia-Roberts Atmospheric Model

The Jacchia-Roberts atmospheric model is an analytical representation of Jacchia 1970 model. Since the Jacchia 1970 model used numerical integration of the barometric and/or diffusion equation to determine the density, it is computationally intensive. For altitudes above 125 km Jacchia used an inverse tangent temperature function, while Roberts [Ref.9] used an exponential temperature profile. By doing so, analytical integration of the diffusion equation was possible. Roberts obtains the density between 90 to 125 km by integration using partial fractions rather than using numerical integration like Jacchia. Even though the original Jacchia-Roberts 1971 model was based on the Jacchia 1970 model and published by Roberts in 1971, changes have been made to this to incorporate some of the features from the Jacchia 1971 model as well.

1.5.4 CIRA 1972 Atmospheric Model

The CIRA-72 model is from COSPAR and had an operational range from 25 km to 2,500 km. The model from 25 km to 75 km is derived from Groves [Ref. 15] whose operational

range is from 25 km to 110 km. The model uses the Jacchia 1971 atmospheric density model for altitudes from 110 to 2000 km. In order to bridge the gap between Grove's low altitude model and Jacchia's high altitude model, an intermediate altitude model is used between 75 to 120 km. In this region, the overlap between Grove's model and Jacchia's model is from 90 km to 110 km., and thus compromise is made between the two, the details of which are given in CIRA-72. Since Jacchia's model uses the boundary condition from 90 km, which would yield different values of density and temperature at 120 km than that obtained using the intermediate altitude model, the boundary conditions at 90 km for the Jacchia model and other parameters all the way up to 120 km, had to be changed to match the results from the intermediate altitude model at 120 km.

1.5.5 MSISE 1990 and NRLMSISE 2000 Atmospheric Models

Both of these atmospheric models come under the Mass Spectrometer and Incoherent Scatter (MSIS) family of models, which are based mainly on the mass spectrometer data from several satellites and incoherent radar scatter data from the ground. The Drag Temperature Model (DTM) based on the air-glow temperature is also used to derive these MSIS models. The 'E' in the MSIS models stands for "Extended", which was first used in the MSISE-90 model to mean that the model has been extended from the ground up. MSISE-90 is an upgraded version of MSIS-86 [Ref.33], while the latter ranges upward from 90 km, the former extends from the ground. For a satellite that is travelling very quickly at perigee, the MSISE models have proven to be successful, thus several bands of atmosphere can be crossed by a satellite in a single integration step. NRLMSISE 2000 [Ref.12], which is a major upgrade of MSISE-90 is popular and used in several applications. Satellite drag data is also included in the formulation of

NRLMSISE 2000. In terms of computational speed, the Jacchia family of models runs faster than the MSIS family of models.

1.6 Previous Research on Atmospheric Density Model Corrections

Previous research on atmospheric density models and satellite drag can be classified into two main fields–dynamic calibration of the atmosphere (DCA) and accelerometer derived density. Accelerometer derived density, where density is measured indirectly from the non-conservational forces measured by the accelerometers on board the satellites.

1.6.1 Dynamic Calibration of the Atmosphere

Dynamic Calibration of the Atmosphere is a technique that is used to make corrections to existing density models in order to improve it. Vallado [Ref. 4] provides a very good introduction to DCA and this introductory paragraph is mainly based that. A set of calibration satellites is used to determine corrections to the density (for some DCA methods, once every three hours). This correction provides fundamental scientific information on the variations and the statistics of these variations in the density. These specific purpose calibration satellites are a group of LEO satellites which have better observational data so that their orbit determination would be more accurate than the average orbit determination results of other satellites. DCA solves for global density corrections and state vector simultaneously for each calibration satellite, using weighted least squares differential correction. The North American Aerospace Defense Command (NORAD) Two Line Element (TLE) data sets information are used to estimate corrections to density once every day. The “true” ballistic coefficient is required as one of the inputs to perform these corrections to existing atmospheric density models such as the Jacchia 71 or MSIS models.

DCA requires observations of trajectories of a large number of satellites, which are then used to make large scale corrections to any given atmospheric model. Using DCA to make such corrections is presented in References 16 to 26. Ref. 16 is about Air Force Space Command (AFSC) High Accuracy Satellite Drag Model (HASDM), which estimates and predicts dynamic variations in the global density field. HASDM uses a DCA algorithm and solves for thermospheric neutral density in near real-time based on observed drag effects on 75 LEO calibration satellites. The DCA algorithm solves for phases and amplitudes of diurnal and semi-diurnal variations in the thermosphere. This gives a dynamically varying global density field where the corrections in density are expressed as a function of latitude, local solar time and altitude. Thus, HASDM was able to reduce the error in the estimated density as compared to the empirical density models.

The development of a method to calculate accurate daily density values based on satellite drag data is presented in Reference 17. A standard six element state vector and ballistic coefficient was obtained by fitting radar and optical observational data by using a differential orbit correction program, which in turn uses special perturbations orbit integration. The modified Jacchia 1970 model that was used in HASDM was used in the orbit integration. Observed energy dissipation rates (EDR) values, "true" 30-year ballistic coefficient value of each satellite, EDR changes computed by the HASDM density model are all used to calculate daily temperature and density values. The authors compared the daily temperature values for the year 2001 with the results from HASDM for validation, and the results were excellent. But since HASDM was developed using the same technique, this may not be a good comparison. Validation of the daily density values with historical values over the past 30 year for over 25 satellites showed small density errors.

The semiannual thermospheric density variations on the Earth's upper atmosphere for a wide range of heights are characterized in Ref. 18. A differential orbit correction program was used to fit the historical radar observations for 13 different satellites in this altitude range, resulting in a six element state vector and a ballistic coefficient value. This process is very similar to the one used for HASDM, and so are the validation techniques and error results.

Ref. 19 uses TLE data sets to generate corrections to atmospheric density models. TLE data sets for a large number of objects whose perigee altitude is less than 600 km and whose element sets are regularly updated in the U. S Space Catalog, and observed solar flux and geomagnetic data are used as inputs to obtain corrections. This process generates corrections to density along with an element set.

An outline of the approach for using TLE data sets to provide density corrections is provided in Ref. 20. These corrections are given as a linear function of altitude to any given atmospheric density model. A large number of drag perturbed space objects, which are observed and cataloged a few times a day, are used for information to create corrections in density without extensive additional costs. Improvements in this method can be achieved if real time observations were used to compare with the TLE data sets.

Ref. 21 discusses corrections to atmospheric density to improve the accuracy of reentry time prediction of space objects. Corrections to the NRLMSIS-00 atmospheric models applied to both spherical and nonspherical shaped space objects to improve the reentry time predictions are assessed. Improvements in reentry prediction times are observed for both type of objects, however the nonspherical shaped objects have relatively lower accuracy because the ballistic coefficient varies with time.

Ref. 22 discusses improvements in the method of DCA. Unlike a typical DCA approach, where global optimal correction coefficients are generated that are directly related to the basis function chosen, this method uses successive refinements to density corrections. These successive refinements are brought about by introducing a series of vanishing coefficients into the procedure for determining atmospheric density model corrections. This improvement in the method is to reduce solution error, especially the errors in the residuals.

The results obtained by comparing the corrections to NRLMSISE-00 using DCA with the Russian DCA density correction method is presented in Reference 23. This comparison is performed during two four year periods with relative differences in solar and geomagnetic activity level. Like previous methods, a large number of satellites are used for comparison in this study as well.

The complexity associated with applying a DCA algorithm to estimate corrections to an existing atmospheric density model such as NRLMSISE-00 is discussed in Reference 24. DCA produces corrections that improve the accuracy; however, this accuracy depends on the agreement between the way the corrections were produced and the way they are applied. Apart from the density corrections, other information such as the time system used, input and output test cases, input parameters used, and any subroutines or model parameters utilized to generate the corrections. The atmospheric density models used for estimating density for a particular application and the model that is corrected must be one and the same. If any of the information related to generating density corrections is missing, then significant differences are observed in the orbit determination process.

Even though DCA improves the atmospheric density estimates after correcting the by atmospheric density models, there are some disadvantages. First of all, when DCA is applied to

a particular orbit determination scheme, the corrections obtained apply only to that specific time period. So if a different orbit determination scheme is used then only the updates to atmospheric density corrections for the orbit determination scheme under consideration can be used and, a complete archive of the density corrections for the given problem is required. The other limitation is that the corrections are restricted to a long time span of 3 hours or a day. This is because of the use of 3-hourly geomagnetic indices and daily solar indices. TLE data sets are not very accurate and since TLE data sets of a large number of LEO satellites are predominantly used as input for DCA, the resulting corrections are not very accurate either. Radar observations are still not as good as precision orbit ephemerides (POE) or satellite laser ranging (SLR) and radar observation data are not readily accessible.

One recent project using DCA is to apply it to a NASA GSFC Precision Orbit Determination and Geodetic Parameter Estimation Program called GEODYN [Ref. 25]. To improve the orbit precision of the GEOSAT Follow-On (GFO), DCA was applied to the NRLMSISE-00 model. The results of this were compared with the results obtained by using the MSIS-86 model for time periods that included a range of solar and geomagnetic activity. So far, this has been done up to an altitude of 600 km and the results showed very little difference. However, according to the authors, a significant improvement in the results is anticipated if the corrections are applied all way up to an altitude of 800 km.

Reference 26 is also recent research where TLE data sets are used to determine satellite drag data, which in turn is used to calculated corrections using DCA. There are two different calibration schemes, with the first one being height dependent scale factors and the second one uses corrections to CIRA-1972 model temperatures and thus the density.

1.6.2 Accelerometers

Accelerometers on board satellites are used to measure the non-conservative accelerations, and then to estimate the density based on these measurements. The accelerometers are sensitive only to non-conservative accelerations such as atmospheric drag, solar radiation pressure, Earth albedo, and Earth infrared pressure. They are insensitive to gravitational forces. Based on accurate radiation force modeling, the acceleration due to atmospheric drag alone can be isolated from the total non-conservative acceleration measured by the accelerometer. From this, density is estimated, which is very accurate as compared to the results from other methods such as DCA. However, only a few satellites have accelerometers onboard and thus accelerometer density data is limited. The recent satellites which have accelerometers on board are CHAMP (re-entered in 2010), GRACE-A, GRACE-B, and Gravity Field and Steady State Ocean Circulation Explorer (GOCE). There are other satellites which had accelerometers onboard and have been flown in the past. One such example is the Satellite Electrostatic Triaxial Accelerometer (SETA) experiment, discussed in Reference 27, which was used to measure atmospheric density at an altitude of 200 km for selected months in the years 1982- 84, by two satellites with accelerometers on board. References 28 to 30 and Reference 2 provide information on extracting densities from CHAMP's accelerometer, and Reference 3 gives information about extracting densities from GRACE's accelerometer. The accelerometer present onboard CHAMP is called the Spatial Triaxial Accelerometer for Research (STAR).

In Reference 28, using accelerometers on board to measure thermospheric events such as large solar mass eruptions reaching the Earth is presented. Models used to estimate non-conservative forces in POD can replace the measurements from the accelerometer, since the latter is more accurate than the results from the models. However, the authors suggest that the

calibration parameters have to be adjusted in order to get the absolute shape of the surface accelerations. They also suggest having an independent external reference for assessment, such as using SLR. But since the thermo burst (short-termed and well-localized thermospheric events) has a tendency to occur in the vicinity of the north and south poles, there are no laser stations to monitor them.

Reference 1 briefly describes how density is estimated from the accelerometer measurements by using a satellite macro model and accurate force models for all the radiative forces. The reference also specifies that the accuracy of the densities derived from accelerometer measurements, which are considered as the 'observed' density, depends mainly on the instrument performance and calibration, as well as on magnitude of unmodeled winds and uncertainty in the drag coefficient model, and thus varies between 1 to 20%. After comparing a few months of accelerometer derived density with the DTM2000 semi-empirical thermosphere model, the results showed that the modeled densities were larger than the former densities with a root mean square (RMS) of 20-30%. Based on these initial promising results, the author feels that future results will be more accurate.

The details of extracting the atmospheric density from the accelerometer measurements are discussed in Reference 29. Before the actual processing of the accelerometer measurements to obtain the density, the measurements undergo preprocessing where corrections due to maneuvers, specific events, and instrumental bias are performed. Estimating the density from the accelerometer measurements requires values of aerodynamic coefficients, which are obtained by using a model that uses diffuse reemission applied to a 15-plate macromodel. Uncertainties in the calibration parameters and of the aerodynamic lift govern the accuracy of the 'observed' densities. Even though the accelerometer derived densities were precise for low

and moderate geomagnetic activity, their uncertainty was relatively higher during high geomagnetic activity because of the lack of empirical wind models to sufficiently model upper-atmosphere neutral winds. The authors suggest that the uncertainty in drag coefficient can be brought down by simultaneous accelerometer and mass spectrometer observations, where both of them are accurately calibrated.

Reference 30 also presents the procedure to extract the density from accelerometer measurements. While STAR is used for accelerometer measurements, the Global Positioning System (GPS) present onboard and SLR are used to calculate accurate orbit positions. After calculating the accelerometer densities for a period of about 21 months, the global density values were compared with those obtained by several other atmospheric density models, such as DTM-2000 (Ref. 31), DTM-94 (Ref. 32), and MSIS-86 (Ref.33). These results were binned as a function of solar activity, position and season. The global mean of the models underestimated the density and the latitudinal gradient estimated was inaccurate. A new model called the DTM-STAR test model, which was created by using DTM-2000 as an *a priori* to estimate certain coefficients that were used to derive densities from the accelerometer, predicts a significantly higher density structure at the CHAMP altitude as compared to other models. However, when densities from the DTM-STAR model were compared with the accelerometer derived densities, the differences were relatively small and also the drag coefficient obtained from precision orbit determination using the DTM-STAR model showed the least bias for high solar activity.

Reference 2 is similar to the previous reference, the procedure to retrieve the density is discussed and provides additional information on atmospheric density obtained from CHAMP's accelerometer. The accelerometer derived density is compared with densities from semi-

empirical density models, for time periods that surround three geomagnetic storms that occurred in 2002. Variations in density due to seasonal, latitudinal, local time, and solar activity effects are also discussed.

Reference 3 gives the procedure to use the accelerometer measurements from the GRACE satellite to determine accurate density measurements. The paper recognizes the limitations of semi-empirical density models, which are not capable of predicting the short scale variations in the density caused when solar and geomagnetic activity vary on short temporal scales, such as during a geomagnetic storm. The satellite prediction accuracy can be improved by providing accurate and timely measurements of the density, which is possible by improving the neutral density models based on in situ measurements of density. The accelerometer present onboard does exactly that, provide in situ measurement of density that are used to correct the existing atmospheric density models.

1.6.3 Additional Approaches

Another way to estimate corrections to atmospheric density is to determine the non-conservative accelerations by GPS and SLR measurements instead of accelerometers. In Reference 34, satellite orbit data and tracking measurements are used to make adjustments (calibration) to the CIRA-72 model, to obtain accurate density values. There are two sources which provide the satellite orbit data and tracking measurements, the first one having high accuracy but limited to a few satellites, and the second is by using TLE data sets that are not very accurate. These two methods are complimentary in the sense that the latter provide higher spatial but lower temporal resolution and also lower accuracy as compared to the former method. The authors propose that a calibration system that works with actual TLE data sets in a

near real-time situation should be researched further. They also recommend a different investigation into alternate calibration schemes since the one that was examined in the paper is best suited using precise tracking or accelerometer measurements as input. The reference suggests that density prediction capabilities can be taken up once near real-time calibration has been set up.

References 35 and 36 give the procedure to extract the non-gravitational accelerations using GPS measurements from the CHAMP satellite. This is done to show that non-gravitational accelerations can be obtained even without onboard accelerometers, but indirectly from GPS satellite-to-satellite (SST) observations. Highly accurate results can be obtained this way because of the availability of very precise gravity field models due to the CHAMP and GRACE gravity missions. Since CHAMP has an onboard accelerometer, the results from GPS accelerometry can be compared with the actual values measured by STAR, which allows calibration and validation of the non-gravitational accelerations estimated from GPS measurements. The accelerations from GPS measurements were obtained in the along-track and cross-track directions only. Accelerations were not estimated in the radial directions to avoid problems because of the coupling between radial and along-track motion, and also because the acceleration is most dominant in the along-track direction. Even though the GPS accelerometry results indicate that this procedure is feasible, the high frequency accelerations are not captured very well.

Reference 37 also estimates accelerations from GPS measurements, but for both the CHAMP and GRACE-A satellites. The paper provides a brief description of the data processing strategy and mainly focuses on the effect of the temporal resolution of the estimated

accelerations. The data for both the CHAMP and GRACE-A satellite perform well in the along-track direction and poorly in the radial and cross-track directions.

Reference 38 analyzes the reduced dynamic orbit determination techniques based on dual-frequency GPS data received onboard the GRACE satellite. The acceleration is estimated as part of the orbit determination using least squares and an extended Kalman filter/smoother, which results in highly accurate orbit estimation. The acceleration estimated by these two methods had a high correlation between them. While the least-squares exhibits robust, smooth, and differentiable trajectories, the Kalman filter/smoother is efficient in utilizing computer memory and processing time.

1.7 Current Research on Atmospheric Density Model Corrections

The long term objective of this research is to estimate corrections to atmospheric density models by orbit determination. POE data that has an accuracy from a few centimeters to within a few meters are obtained by using data from satellite GPS receivers in an optimal orbit determination process. The POE data are then used as the input measurement in a sequential optimal orbit determination scheme to estimate corrections to existing atmospheric density models. Using POE instead of TLE data sets results in significant improvements in the estimated density. The corrected densities are then compared with accelerometer derived densities (for CHAMP and GRACE, since they have accelerometers onboard), which are considered as the true density values, for validation.

Reference 39 describes the procedure to estimate corrections to atmospheric density models using POE in an optimal orbit determination scheme. In Reference 40, the results of POE derived density for CHAMP are compared with CHAMP's accelerometer derived density.

Reference 41 is similar to the previous reference, and the authors try to find the right combination of input to get the best correlation with the accelerometer derived density. The inputs that are varied are the baseline density models, the density and ballistic coefficient correlation Gauss-Markov half-lives, and solution time spans. Results indicate that the POE derived densities showed better correlation with accelerometer derived densities than either Jacchia-71 or HASDM densities. In Reference 42, densities are estimated during periods of high solar and geomagnetic activity. Here too, the POE derived densities are compared quantitatively with respect to the accelerometer derived densities calculating the cross correlation (CC) between the two. These CC results are separated into different solar and geomagnetic bins. Further research is presented in Reference 43, where the effect of different solution fit span length, and also higher density and BC correlation half-life, on the accuracy of the POE derived density are investigated.

The research continues in Reference 44 where along with CHAMP, two more satellites–GRACE and TerraSAR-X [Ref. 45]–are used to get POE derived density along their trajectories. This reference also shows that travelling atmospheric disturbances cannot be detected from POE derived densities.

In Reference 46, densities are estimated for the CHAMP and GRACE satellites for the same time period and compared with their respective accelerometer derived densities. In Reference 47, density estimates are made for multiple satellites–CHAMP, GRACE, and TerraSAR-X, over the same time periods. Only the POE derived densities for CHAMP and GRACE are compared with their respective accelerometer derived densities, since TerraSAR-X does not have an accelerometer onboard. Conclusions drawn from results obtained for CHAMP and GRACE are used for TerraSAR-X.

In Reference 48, the POE derived densities of CHAMP and GRACE satellites are compared with their respective accelerometers by calculating the CC and RMS. Since GRACE is twin satellites (GRACE-A and GRACE-B) the POE derived densities calculated for both the satellites are compared with respect to each other. The plots overlapped and the CC between the twin satellites was very high. A subset of days in the year 2008 and 2009 were examined to see their behavior during low solar activity. According to this reference, the POE derived densities were nearly always superior than both empirical density models as well as HASDM densities. From late October 2005 to January 2006, POE derived density, HASDM density, and empirical density models, all showed poor correlation with respect to GRACE-A's accelerometer density. The plots indicated that the short period density variations shown by the accelerometer derived density were not captured by the other three types of densities. This is further investigated in Reference 49 where the authors characterize these time periods and explain the anomalous behavior.

Reference 50 follows a procedure similar to previous references, to calculate POE derived densities for CHAMP and GRACE and compare it with accelerometer derived densities. However, unlike the previous references which used only the accelerometer derived density by Sean Bruinsma, the accelerometer derived density by Eric Sutton from the University of Colorado (currently working at the Air Force Research Laboratory) is also used in this reference. The author compares the two different sources of accelerometer derived densities for both CHAMP and GRACE, and concludes that since they correlate very well, one can be used as a substitute for the other. The author also compares the POE derived density for both CHAMP and GRACE with respect to accelerometer derived density from both Bruinsma and Sutton, and shows that the results are nearly identical. Finally, this reference calculates

POE derived densities for ICESat and TerraSAR-X. Since neither ICESat nor TerraSAR-X have accelerometers onboard, the densities were compared with respect to those of CHAMP and GRACE qualitatively, by plotting the densities. These plots show similar trends and are useful in understanding the density variations at different altitudes and orbits.

1.8 Linear Weighted Blending Technique

Reference 51 examines the density estimated using POE for CHAMP and GRACE, and the effect on accuracy of using the linear weighted blending technique for the density during the overlap periods. References 52, 53, and 54 have used the linear weighted blending technique to bridge data (density and temperature) for a region of altitude (140 km to 200 km) obtained by two different density models. The linear weighted blending technique is a mathematical tool to stitch two datasets in a common or overlap region (like measurements of the same quantity at the same time but by different instruments) so that there is one continuous dataset having a value that is in between the two. However, it is not a simple average since that would result in the data points being discontinuous at the first and the last point in the overlap region. More details of this technique are described in the methodology section. Even though the technique used in this reference is the same, the blending of data is between two datasets for a common time period, and not a region of altitudes. Also, the primary objective of this reference is to create continuous data sets of density, and improving the accuracy is secondary. The technique used here is purely mathematical and not physics based. Since the dataset during the overlap period is not a one-to-one function, a cubic spline cannot be used.

1.9 Gauss-Markov Process

In orbit determination, not all the forces are modeled, and whatever is modeled will not be completely accurate. Thus, in order to account for unmodeled or inaccurately modeled forces or accelerations acting on a spacecraft, using a first-order Gauss-Markov process for dynamic model compensation in orbit determination is common. As the name implies, a Gauss-Markov process has the properties of a Gaussian probability and Markov process. A Gaussian process has a Gaussian or normal distribution and a Markov process is one, where the future state depends on the current state only, and not on other states before the current state. Since the current research does not model all the forces and uses inaccurate models to determine orbits, a Gauss-Markov process is used to estimate corrections to atmospheric density models used. More information on the Gauss-Markov process can be found in Reference 55.

1.10 Estimating Density and Ballistic Coefficient Separately

Acceleration due to atmospheric drag is proportional to the product of density and ballistic coefficient, and thus estimating both of them simultaneously in orbit determination is difficult. Reference 56 and 57 describes the procedure to estimate both the density and ballistic coefficient simultaneously and separately in real time.

Earlier, when density was estimated in an orbit determination process, the ballistic coefficient estimate had to absorb errors in density models as well as in ballistic coefficient models. However, in the current research, both density and ballistic coefficient are estimated simultaneously, and this is possible when the exponential half-life of ballistic coefficient errors and that of atmospheric density errors are significantly different from each other. Since a Gauss-Markov process is used to estimate corrections to density models, a half-life determines

how much of the previous state affects the current state. A half-life of a quantity is the time it takes the quantity to decay to half its initial value. In simultaneous density and ballistic coefficient estimation, there is atmospheric density correlated half-life and ballistic coefficient correlated half-life, both of which have to be specified by the user. More details about this method are discussed in the next chapter on Methodology.

In Reference 43, Hiatt examines the effect of varying the initial value of BC used as an input in orbit determination to estimate the density in CHAMP. Hiatt examines two days, one of them with moderate solar and quiet geomagnetic activity level and the other day having a high solar and active geomagnetic level. The initial BC is varied as a different percentage of nominal BC from 1% to 1100%. A subset of this, 90%, 110%, and 150% of nominal BC, was selected for further study based on the results of residuals, position, and velocity consistency tests. Cross correlation was calculated between the POE derived densities obtained from these three initial BC and the accelerometer derived densities. Hiatt concluded that based on the initial results, as long as the initial BC is within ±10% of the nominal BC, the orbit determination process produces relatively good POE derived density estimates. An examination of BC plots for different values of initial BC indicated that as the difference between the initial BC and nominal BC increased, so did the difference between the average of the POE derived BC and initial BC. According to Hiatt, this is because the orbit determination process is trying to estimate a more accurate BC than the incorrect initial BC used. This indicates that there is scope for using orbit determination to be used in an iterative manner to perform a convergent study to estimate a more accurate initial BC, but is suggested as future work. Hiatt also examined the influence of estimating and not estimating the BC as part of the orbit determination on the POE derived density estimates. Even though the CC between the POE

derived density and accelerometer derived density for the case of estimating and not estimating the BC was found to be similar, the differences was more pronounced as the solar and geomagnetic activity level increased.

Reference 58 continues Hiatt's work from Reference 43, and examines four main things: the effect of different BC and density correlated half-lives on both BC and density, sensitivity of the estimated density to the initial value of BC used, the effect of using a converged value of BC as initial BC to estimate density, and whether estimated BC absorbs error in the estimated atmospheric density. The study was performed for a few days on the CHAMP satellite. The authors found that increasing the BC correlated half-life increases the estimated density and decreases the BC, and vice-versa. Also, increasing the density correlated half-life decreases the density and increases the BC, and vice-versa. The authors vary the value of the initial BC used as different percentages of the nominal BC and examine the estimated BC and also the density, similar to the procedure adopted by Hiatt in Reference 43. The results and conclusions that the authors came up based on this study were same as that of Hiatt [Ref. 43]. The authors used orbit determination in an iterative fashion to find the converged value of BC, and then compare the accelerometer derived density with the POE derived density using the converged value of BC as the initial BC and also that obtained by using the nominal value of BC as the initial BC. The results indicate that the RMS between the accelerometer derived density and the density estimated using the converged BC as initial BC is worse than the one obtained using nominal value of BC. The authors feel that this may not be significant given the possibility of bias in the accelerometer derived density and thus conclude that performing a convergence study is not worth the effort if there is a good estimate of the nominal BC. The authors also examine the effect of estimating and not estimating the nominal BC during the

orbit determination process on the estimated density, as in Reference 43. Even though significant differences were not found, they found that estimating the BC is better since this yields better results. Finally, the authors calculate the CC between the density error and the BC to see if the BC estimation is absorbing density error, in which case one would expect a high negative CC between the two. The density error is defined as the difference between the accelerometer derived density and POE derived density. The authors found that only the day with high solar and geomagnetic activity showed a significant negative correlation between the density error and the estimated BC.

Reference 59 continues the work started in Reference 58 to see if BC estimates absorb the density errors by increasing the number of days examined for CHAMP and also looking into GRACE. This was done by calculating the CC between the density error and estimated BC for two different density correlated half-lives of 18 minutes and 180 minutes. The results showed a significant negative CC between the density error and estimated BC for a density half-life of 18 minutes as compared to 180 minutes, indicating that the estimated BC is absorbing the errors in POE derived density when the half-life is 18 minutes. The authors also examined the effect of estimating and not estimating the BC in orbit determination, on the POE derived density. The results showed marginally superior results for the CC between POE derived density and accelerometer derived density, when the BC was estimated as compared to not estimating BC.

1.11 Satellites Examined

This section is a brief discussion of the satellites whose data was used for this research. Four satellites were used and they are CHAMP, GRACE (GRACE-A only), TerraSAR-X, and ICESat.

1.11.1 CHAMP Satellite

The information on CHAMP that is presented here is from Reference 60. The primary mission of CHAMP was for geophysical research and application. CHAMP was launched on July 15, 2000 and originally designed for a five year mission to resolve long-term temporal variations primarily in the magnetic field, in the gravity field, and within the atmosphere. However, CHAMP exceeded its original intended mission lifetime by about 5 years and reentered on the September 20, 2010. Some of the instruments present onboard CHAMP that are relevant to this research either directly or indirectly are the dual-frequency GPS receiver, retroreflector array, and the three-axes accelerometer (STAR). The initial perigee altitude of CHAMP was 474 km, the orbit is nearly circular with an eccentricity of 0.00396, and has an inclination of 87.27 degrees. The initial mass of CHAMP was 400 kg. During the mission, the mass was reduced due to consumption of the onboard propellants that were used to fire the thrusters for orbit maintenance.

Figure 1.3: CHAMP satellite as depicted by an artist [Ref. 60].

1.11.2 GRACE Satellite

The information on the twin satellites GRACE-A and GRACE-B that is presented here is from Reference 61. The primary mission of the GRACE satellites is to provide high resolution estimates of the Earth's gravity field and its variability in time. GRACE is actually a pair of satellites that are flying at a distance of 220 km from each other and are in a polar orbit of altitude 500 km. GRACE was launched on the 17th of March 2002 and originally designed for a five year mission. However, GRACE has exceeded its original intended mission lifetime and continues to orbit at the time of this writing. The instruments present onboard GRACE are similar to that of CHAMP and includes an accelerometer as well. The initial perigee altitude of CHAMP is 485 km, the orbit is nearly circular with an eccentricity of less than 0.005, and has an inclination of 89 degrees. The initial mass of each of the GRACE satellites was 432 kg.

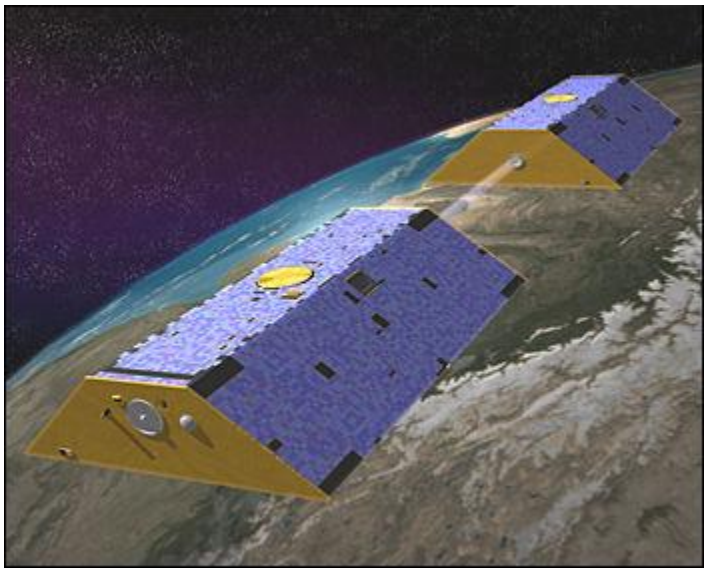

Figure 1.4: The twin GRACE satellites flying in formation as depicted by an artist [Ref. 61].

1.11.3 TerraSAR-X satellite

The information on TerraSAR-X that is presented here is from Reference 62. The primary mission of TerraSAR-X is for the provision of X-band Synthetic Aperture Radar (SAR) data for scientific research and applications. TerraSAR-X was launched on the June 15, 2007 and originally designed for a five year life. However, TerraSAR-X has exceeded its original intended mission lifetime and continues to orbit at the time of this writing. This satellite has a GPS receiver and retroreflector array, which are used to generate POE but does not have an accelerometer. TerraSAR-X orbits in a circular dawn-dusk Sun synchronous orbit, with an initial perigee altitude of 514 km, and with an inclination of 97.44 degrees. The initial mass of TerraSAR-X was 1,230 kg. During the mission, the mass was reduced due to consumption of the onboard propellants that were used to fire the thrusters for orbit maintenance.

Figure 1.5: TerraSAR-X satellite as depicted by an artist [Ref. 62].

1.11.4 ICESat satellite

The information on ICESat that is presented here is from Reference 63. Some of the objectives of ICESat are to measure the polar ice sheet thickness; measure cloud heights; map the topography of land surfaces; and measure roughness, snow-cover, and sea-ice surface characteristics. ICESat was launched on January 13, 2003 and originally designed for three to five years. However, ICESat exceeded its original intended mission lifetime and reentered after seven years of operation. The primary instrument onboard was the Geoscience Laser Altimeter System (GLAS), which was used for a laser altimetry science mission. The initial perigee altitude of ICESat was 600 km, the orbit was a near circular retrograde orbit with an eccentricity of 0.001 and an inclination of 94 degrees. The initial mass of ICESat was 970 kg.

Figure 1.6: ICESat satellite as depicted by an artist [Ref. 63].

2 METHODOLOGY

This section describes the process used to estimate corrections to atmospheric density models using orbit determination. Position and velocity vectors of the satellites were used as input in an optimal orbit determination technique to estimate corrections to baseline atmospheric density models. By varying the input to an optimal orbit determination technique, the estimated density also varies. These estimated densities are then compared with the accelerometer derived densities, which are considered as the true densities in this study. The inputs varied were, the BC and density correlated half-lives, baseline atmospheric density, and different functions of a_p. The procedure to create continuous density data sets by combining 14 hour data sets into one week data sets is described here. Estimating the approximate areas of the TerraSAR-X and ICESat satellites facing the Earth, the Sun, and the normal to the velocity vector are discussed here as well.

2.1 Precision Orbit Ephemerides

Ephemerides are the tabulated values of position and velocity vectors of several satellites over time. When the ephemerides are generated using high fidelity numerical techniques, they are called Precision Orbit Ephemerides (POE). The POEs are available for CHAMP, GRACE (both GRACE-A and GRACE-B) and TerraSAR-X from the GFZ German Research Center for Geosciences website and can be downloaded at http://isdc.gfz-potsdam.de/. For CHAMP, the POEs are available as either rapid science orbits (RSO) or precision science orbit (PSO). The processing and accuracy of RSO has been examined from Reference 64 to 67. The accuracy of the RSO is about 5-10 cm as compared to satellite laser ranging (SLR) for most of CHAMP's mission life. No published data are available for accuracy

of the PSO but they are believed to be at least as accurate as the RSO or even better because PSOs incorporate additional gravity field solutions obtained from CHAMP, and using PSO is thus desirable. But PSO are not available after the year 2003 and therefore this study uses RSO, which are available in 14 hour fit spans. PSO are not available for GRACE at all, so RSO must be used.

2.2 Optimal Orbit Determination

The discussion of optimal orbit determination in this subsection is obtained mainly from References 55, 4, and 68. Orbit determination is the process of determining the motion of a satellite with respect to the center of the celestial body in a given coordinate system. The satellites that are of interest in this research are artificial Earth satellites, and since they are significantly smaller in size and lower in mass, non-gravitational forces acting on them are significant. Since these satellites orbit relatively close to the Earth's surface (especially LEO satellites), the gravitational forces due to the aspherical shape of the Earth must be considered.

A set of parameters that are required to predict the future state of a system is called the state of a dynamical system. For orbit determination of a satellite, at least six parameters are required. These six parameters can be the three components of position and velocity vector each in a Cartesian coordinate system or six classical orbital elements. However, to improve the accuracy of prediction of the future state of a satellite, the parameters required would be more than six, and would include dynamic and measurement model parameters.

To give a general description of the orbit determination problem, consider a satellite orbiting Earth, whose state vector at initial time, t_0, is X_0. This satellite will be described by a set of governing differential equations, which account for the forces acting on the satellite. By

integrating these equations over time with the initial conditions known, the future state of the satellite can be predicted. However, the initial state of a satellite is not known accurately and the governing differential equations are incomplete and/or inaccurate. Thus the predicted value of the satellite state at a future time would be different from the actual state at the same time. This difference grows with time. However, by making actual measurements of the satellite state, these future estimates would be more accurate. Even these estimates would not be completely accurate since the observations are subjected to both systematic and random errors. Even the measurements do not measure the state of the satellite directly but rather observe quantities like range, range rate, elevation, and azimuth, which are nonlinear functions of the state vector.

The above paragraph about orbit determination can summarized, according to Tapley et al. [Ref. 55], by saying that "*The problem of determining the best estimate of the state of a spacecraft, whose initial state is unknown, from observations influenced by random and systematic errors, using a mathematical model that is not exact, is referred to as the problem of state estimation. In this presentation, such a procedure will be referred to as the process of orbit determination.*" The "best" estimate means optimal in some statistical sense, which will be described later in this section. Apart from the errors present in the orbit determination described above, additional errors also exist due to the computational procedure, numerical integration procedure, and truncation errors.

POE are used in this research as input measurements in a sequential Kalman filter/smoother which uses Gauss-Markov processes. The details of the sequential filter/smoother are given in upcoming sections of this chapter. The type of filter used is the

extended Kalman filter, thus the state estimate is updated at each time where the observations are available, which will improve the accuracy of the estimates.

As mentioned before, the "best" estimate is optimal in statistical sense and does not have a single unique definition but depends on the application. There are several definitions and methods with varying results. Several things have to be considered before adopting any of the methods. Some offer higher accuracy at the cost of lower speed. Questions such as whether to use sequential methods or batch methods, to minimize the size of measurement residuals or the size of orbit errors, and how to model measurement residuals and orbit errors are to be considered. Since all orbit determination problems are nonlinear and multidimensional, there are two choices available, either to solve the multidimensional nonlinear problem directly or linearize the problem first. Wright [Ref. 69] describes the meaning of optimal orbit determination used in this research, and this definition is given in terms of eight statements, which are quoted below.

1. "*Sequential processing (SP) is used to account for force modeling errors and measurements information in the time order in which they are realized.*
2. *The optimal state error estimate* $\Delta\hat{X}$ *is the expectation of the state error* ΔX *given the measurement residual* Δy. *That is:* $\Delta\hat{X}=E\{\Delta X|\Delta y\}$. *This is Sherman's Theorem.*
3. *Linearization of state estimate time transition and state to measurement representation is local in time, and not global.*
4. *The state estimate structure is complete.*
5. *All state estimate models and state estimate error model approximations are derived from appropriate force modeling physics, and measurement sensor performance.*

6. *All measurement models and measurement error model approximations are derived from appropriate sensor hardware definition and associated physics, and measurement sensor performance.*
7. *Necessary conditions for real data:*
    - *Measurement residuals approximate Gaussian white noise.*
    - *McReynolds filter-smoother consistency test is satisfied with probability 0.99.*
8. *Sufficient conditions for simulated data: The state estimate errors agree with the state estimate error covariance function.*

The first six requirements define standards for optimal algorithm design, and the creation of a realistic state estimate error covariance function. The last two requirements enable validation: They define realizable test criteria for optimality. The last requirement implies the development and use of a physically realistic measurement simulator."

2.3 Gauss-Markov Process Half-Lives

In this research, Gauss-Markov processes are used to estimate corrections to atmospheric density models. Orbit Determination Tool Kit (ODTK) software estimates the atmospheric density corrections as well as BC corrections. If ρ is the density estimated by ODTK from an atmospheric density model, then $\Delta\rho/\rho$ is the estimated correction to the density. Similarly, if B is the BC estimated by ODTK, then $\Delta B/B$ is the estimated correction to the BC. The estimated density and BC, along with the corrections are a function of the baseline atmospheric density models used. The user of ODTK has to specify this baseline atmospheric density model. The user also has to specify the density correlated half-life and BC correlated half-life, which represents the time required for the estimated correction of density and BC,

respectively, to decay to half its value in the absence of any measurement data. These half-lives are associated with the exponential half-lives in the Gauss-Markov process. More information on Gauss-Markov process half-lives along with the mathematical expressions can be obtained from References 70 and 71. Some of the mathematical relations are given in this section from these references.

If $x = x(t_k)$ is the dynamic scalar random variable, then the exponential Gauss-Markov sequence is given by,

$$x(t_{k+1}) = \Phi(t_{k+1}, t_k)\, x(t_k) + \sqrt{\left\{1 - \Phi^2(t_{k+1}, t_k)\right\}} \cdot w(t_k), \text{ where } k \in \{0,1,2,...\}$$

Where $w(t_k)$ is the Gaussian white random variable with mean equal to zero and a constant variance equal to σ_w^2. The transition function, Φ, is given by, $\Phi(t_{k+1}, t_k) = e^{\alpha|t_{k+1} - t_k|}$.

The constant in the exponential term, α, is related to the user defined half-life, τ, by the following expression.

$$\alpha = \ln(0.5)/\tau$$

Since τ is always positive with units of time, and the natural log of 0.5 is negative, α is always negative. Thus Φ decays with time.

2.4 Filter-Smoother Description

The information on the filter and smoother given in this section is obtained from References 55 and 72. A filter uses POE as input measurements and then estimates the state vector. This state vector has several parameters like the components of position and velocity, atmospheric density correction, spacecraft BC correction, and other parameters and other forces, measurements, and model parameters. The output from the filter at each time step,

which consists of the state estimate, is used along with the measurements at that time as the inputs to estimate the state at the next time step. Thus the filter processes the data sequentially forward in time.

Unlike the filter, the smoother inputs and processes the input data in reverse chronological order, and the input data for the smoother is the stored filtered state and covariance information. Thus the input data for a smoother at any time step is defined by the stored filter output data at that time as well as all the previous smoother output data. Since the smoother makes use of the entire filter output data, the state estimate by the smoother is more accurate and behaves smoothly, and the covariance is smaller than the filter state estimates.

2.5 McReynolds filter-smoother consistency test

The McReynolds filter-smoother consistency test is used to validate the filter and smoother estimates. The test is described in Reference 69. A dimensionless ratio, $\bar{R}$ is created for each of the parameters of the state estimate. The numerator of this is the difference between the filter estimate and the smoother estimate of the same time. If at any time t_k, for k={1, 2, 3, .., L}, the filter state estimate is given by $\hat{X}_k$ and smoother state estimate is given by $\tilde{X}_k$, then the difference between the two is $\bar{X}_k = \hat{X}_k - \tilde{X}_k$. The denominator is the square root of the main diagonal elements of the matrix that is formed by taking the difference between filtered covariance matrix and the smoother covariance matrix. So if the filtered covariance matrix is $\hat{P}_k$ and the smoother covariance matrix is $\tilde{P}_k$, then the difference between the two is $\bar{P}_k = \hat{P}_k - \tilde{P}_k$. Now if the covariance matrix is an $N \times N$ matrix and the state vector is an $N \times 1$ matrix, then denote the i^{th} element of $\bar{X}_k$ as $\bar{X}_k^i$ and the i^{th} element of the main diagonal element of $\bar{P}_k$ as $\bar{P}_k^i$,

then the i^{th} element of the dimensionless ratio, $\bar{R}$, at time, t_k, is given by, dimensionless ratio, $\bar{R}_k^i = \bar{X}_k^i \Big/ \sqrt{\bar{P}_k^i}$. This is calculated for all N elements at t_k and then for all time where the filter and smoother estimates exist. Now, for a parameter of the state vector of interest, if 99% of the ratios have a value of $\bar{R}_k$ less than or equal to 3, for all time where the filter and smoother estimates exist, then the McReynolds filter-smoother test is considered to be passed.

2.6 Using Orbit Determination to Estimate Density

The density is estimated in an optimal orbit determination technique. The POE are used as measurements in a sequential measurement and filtering scheme using ODTK software, which provides the orbit determination. The filter estimates a state vector and the smoother runs all the solution data generated by the filter, sequentially backward in time, and uses the last filter estimate to initialize it. Since the smoother uses all the available data from the filter output, the smoother's output is superior and thereby generates more accurate estimates. The force models used in this research include a 90×90 GRACE Gravity Model 2 (GGMO2C), solar radiation pressure, Earth infrared and albedo radiation pressure, solid Earth and ocean tides, luni-solar point masses, and general relativity.

The technique to estimate density as a part of an orbit determination process has been shown by Wright in Reference 56. Both atmospheric density and ballistic coefficient can be simultaneously observed as shown by Wright and Woodburn in Reference 57. They also show that while 3-hourly step functions of geomagnetic indices fail the McReynold's filter/smoother consistency test, the polynomial spline used to fit the 3-hourly step functions passes the same

test. The algorithm used to obtain the osculating splines of 3-hourly step functions is presented by Tanygin and Wright in Reference 73.

The atmospheric density is estimated as a correction to a baseline atmospheric model in ODTK. There are five models of atmospheric density currently available in ODTK (Version 6). They are Jacchia 1971, Jacchia-Roberts, CIRA 1972, MSISE-1990, and NRLMSISE-2000. The model that is used as the baseline density model is different for different studies and will be discussed in the relevant section. Two different types of corrections are applied to the selected atmospheric density model. The first one is a baseline correction based on the historical solar flux measurement of $F_{10.7}$ and geomagnetic activity measurement in the form of planetary geomagnetic amplitude a_p, that is obtained over several solar cycles. The corrections are propagated from the perigee height using an exponential Gauss-Markov sequence, where the half-life of the Gauss-Markov process can be specified by the user. A transformation is used to relate the error in the atmospheric density at the perigee to the error at any point in the orbit. The second correction is dynamic in nature where a correction is applied at each point based on measurements and current conditions. Estimating corrections at each time step in a sequential filter is easier than for a batch least squares process where one single correction is applied to the entire data set or many corrections lead to a large state vector. Similar to the first type of correction, exponential Gauss-Markov processes for the modeling errors are used in the dynamic corrections too, with associated density and ballistic coefficient correlated half-lives. These half-lives are user specified and their value determines how much past data effects the correction.

Yearly averages for the inverse ballistic coefficient for CHAMP are used as the nominal values to initiate the filter and came from Reference 74. The yearly values are 0.00444 m^2/kg

for 2002-2003 and 0.00436 m^2/kg for 2004-2005. The yearly average inverse ballistic coefficient for the remaining years of the CHAMP mission life were extrapolated by Hiatt in Reference 43 based on mass data and is 0.00426 m^2/kg for the year 2007 and later years. Only one value of inverse ballistic coefficient was used for GRACE to initialize the orbit determination process, 0.00687 m^2/kg, as determined in Reference 74.

The POE derived densities can be varied by varying the different types of inputs. In this study the parameters that are varied are density and BC correlated half-lives and baseline atmospheric density. Variation of other parameters such as nominal BC initialization value, solution fit span length, solution overlaps have been examined earlier by Hiatt in Reference 43.

2.7 Validation of Estimated Density

To validate the POE derived densities, they are compared with the accelerometer derived densities for satellites that have accelerometers onboard. This is because accelerometer derived densities are considered as the control or true densities since the densities derived from accelerometers are the most accurate. Accelerometer derived densities are available for both CHAMP and GRACE satellites but not for TerraSAR-X and ICESat, since the latter two do not have accelerometers onboard. The accelerometer derived densities for CHAMP and GRACE are obtained from Sean Bruinsma at the Centre National d'Etudes Spatiales (CNES), who has derived the density along the path of CHAMP and GRACE using the accelerometer measurements. Similarly, Eric Sutton from the University of Colorado (currently working at the Air Force Research Laboratory) has also obtained the density from the measurements from accelerometers onboard CHAMP and GRACE.

2.8 Cross Correlation and Root Mean Square

The zero delay cross correlation coefficient is a non-dimensional number which can be between -1 to +1 and is to quantify how two signals correlate. A value of 1 indicates that there is perfect correlation between the two; a value of -1 indicates that the signals correlate in an inverse manner, and a value of zero indicates that there is no correlation between the two.

Consider two signals or datasets, $x(i)$ and $y(i)$, where i=0, 1, 2, …., N is the number of elements in each dataset. Then, the zero delay cross correlation is given by the following expression [Ref. 75].

$$CC = \frac{\sum_{i=1}^{N}\left[\left(x(i)-\bar{x}\right)\left(y(i)-\bar{y}\right)\right]}{\sqrt{\sum_{i=1}^{N}\left(x(i)-\bar{x}\right)^2}\sqrt{\sum_{i=1}^{N}\left(y(i)-\bar{y}\right)^2}} \tag{2.1}$$

Where, $\bar{x}$ and $\bar{y}$ are the mean values of the datasets $x(i)$ and $y(i)$, respectively.

Even though the CC quantifies the correlation between two datasets, it says nothing about their relative magnitude and how well they match. If two datasets or signals vary in a similar manner or pattern but have very different magnitudes, they will still have a high value of CC between them. Thus the RMS between the two signals should also be calculated if information about their relative magnitude is to be known. The RMS for the two datasets is given by the following expression.

$$RMS = \sum_{i=1}^{N}\sqrt{\frac{\left(x(i)-y(i)\right)}{N}} \tag{2.2}$$

Unlike CC, RMS has the same units as $x(i)$ and $y(i)$. In this research, the RMS is calculated between two densities, thus the dimension is mass per cubic length (kg/m^3 in S.I. units).

To calculate either CC or RMS, both datasets should have the same number of elements. In this research CC and RMS are calculated for POE derived density and HASDM density with accelerometer derived density. Since they do not have the same number of elements in a given time span, both POE derived density and HASDM densities are interpolated using Hermite interpolation to match the time tags of accelerometer derived density. The reason for choosing Hermite interpolation is because previous research in the same field [Ref. 43] has examined linear interpolation as well and decided to use Hermite interpolation. Also, the POE derived density and HASDM densities are interpolated to match the accelerometer derived density time tags and not the other way round because accelerometer derived density is considered as the true density in this research.

2.9 Linear Weighted Blending Technique to Create Continuous Data Sets

In order to create a continuous data set, two techniques were used. The first one was to bridge two successive solutions of estimated density for the overlap period using the linear weighted blending technique. This overlap period is the first two hours and last two hours of a 14 hour fit span. The second method was to blend the same overlap periods using the linear weighted blending technique for the position vectors of the POE, and then use it as measurements in the optimal orbit determination technique to estimate the densities. Both of them were compared with accelerometer derived density by calculating their cross correlation.

A total of 100 days were examined for this research, selected in such a way that they span almost the whole of CHAMP's mission life, include a wide range of solar and geomagnetic activity, differing periods of solar cycle, and at different positions of Earth in its orbit around the Sun. The classification of solar and geomagnetic activity bins is based on Picone et al. [Ref. 12], and uses the daily solar flux, $F_{10.7}$, and daily planetary geomagnetic amplitude, A_p. The 100 days were picked so that their percentage distribution of solar and geomagnetic bins would match that of CHAMP's mission lifetime, as given in Reference 44, and reproduced in Table 2.1.

Table 2.1: Solar and Geomagnetic activity bin distribution for CHAMP mission life [Ref. 44**].**

Activity Bin	Definition of Bin	CHAMP Mission Life
Low Solar	$F_{10.7} < 75$	20.8 %
Moderate Solar	$75 \leq F_{10.7} < 150$	57.8 %
Elevated Solar	$150 \leq F_{10.7} < 190$	12.0 %
High Solar	$190 \leq F_{10.7}$	9.5 %
Quiet Geomagnetic	$A_P \leq 10$	63.7 %
Moderate Geomagnetic	$10 < A_P < 50$	33.5 %
Active Geomagnetic	$50 \leq A_P$	2.8 %

Only one set of ballistic coefficient and density correlated half-lives equal to 1.8 and 180 minutes, respectively, was used. Lechtenberg [Ref. 44] showed that using the Jacchia family of density models as the baseline has the highest correlation with accelerometer derived density, and for most of the bins it was CIRA 1972. For all the bins, a ballistic coefficient correlated half-life of 1.8 minutes had the best results, while the density correlated half-life was either 18 or 180 minutes, depending on the bin. While 18 minutes was more common for CHAMP, especially for higher activities, 180 minutes was always better for GRACE.

The 100 days examined for this study are displayed in Table 2.2 and Table 2.3, with each day under its respective solar and geomagnetic bin, respectively. The solution span examined for all these days was 14 hours duration and ranged from 10 hours to 24 hours.

Table 2.2. Days examined for CHAMP by Solar activity Bins.

Activity Level Bin	CHAMP Mission Life		
Low Solar F10.7 < 75	October 27, 2005	February 13, 2007	September 12, 2007
	May 14, 2006	March 9, 13, 16, 17, 2007	November 18, 2007
	July 14, 11, 2006	April 11, 23, 2007	March 3, 9, 2008
	September 25, 2006	June 20, 2007	May 8, 2008
	December 20, 2006	August 7, 2007	June 4, 2008
Moderate Solar $75 \leq$ F10.7 < 150	October 1, 2002	December 15, 19, 2003	November 15, 20, 2004
	January 7, 17, 23, 2003	January 7, 8, 2004	December 14, 2004
	February 13, 24, 2003	February 8, 12, 20, 2004	January 6, 2005
	April 5, 7, 2003	March 7, 10, 2004	February 8, 2005
	May 17, 2003	April 2, 9, 14, 2004	March 7, 30, 2005
	June 24, 2003	May 8, 27, 2004	May 10, 2005
	July 8, 17, 2003	June 12, 2004	July 9, 15, 2005
	August 5, 2003	July 5, 15, 24, 25, 2004	September 20, 2005
	September 6, 24, 2003	August 5, 8, 2004	December 7, 2005
	October 5, 19, 2003	September 10, 17, 2004	April 3, 2006
	November 7, 9, 2003	October 8, 13, 2004	November 15, 2005
Elevated Solar $150 \leq$ F10.7 < 190	June 6, 2001	June 9, 2002	April 2, 2003
	August 8, 2001	October 4, 27, 2002	October 23, 2003
	March 18, 28, 2002	January 13, 2003	July 20, 23, 2004
High Solar F10.7 $\geq$ 190	June 17, 22, 2001	February 5, 21, 2002	July 30, 2003
	September 26, 29, 2001	April 17, 2002	October29, 2003

Table 2.3. Days examined for CHAMP by Geomagnetic activity Bins.

Activity Level Bin	CHAMP Mission Life		
Quiet Geomagnetic $Ap \leq 10$	June 6, 17, 22, 2001 August 8, 2001 February 21, 2002 March 28, 2002 June 9, 2002 July 30, 2002 January 13, 17, 2003 February 13, 24, 2003 April 7, 2003 May 17, 2003 July 8, 2003 August 5, 2003 September 6, 2003 October 5, 23, 2003 November 7, 2003 December 19, 2003 January 8, 2004	February 8, 20, 2004 March 7, 2004 April 2, 14, 2004 May 8, 27, 2004 June 12, 2004 July 5, 15, 20, 2004 August 5, 8, 2004 September 10, 2004 October 8, 2004 November 15, 2004 December 14, 2004 January 6, 2005 March 30, 2005 May 10, 2005 July 15, 2005 September 20, 2005 October 27, 2005	December 7, 2005 April 3, 2006 May 14, 2006 May 14, 2006 July 11, 2006 September 25, 2006 November 15, 2006 March 9, 17, 2007 April 11, 2007 June 20, 2007 September 12, 2007 November 18, 2007 March 3, 2008 May 8, 2008 June 4, 2008
Moderate Geomagnetic $10<Ap<50$	September 26, 29, 2001 February 5, 2002 March 18, 2002 October 27, 2002 January 23, 2003 April 2, 5 2003 June 24, 2003 July 17, 2003 September 24, 2003 October 19, 2003	November 9, 2003 December 15, 2003 January 7, 2004 February 12, 2004 March 10, 2004 April 9, 2004 July 24, 2004 September 17, 2004 October 13, 2004 November 20, 2004	February 8, 2005 March 7, 2005 July 9, 2005 July 14, 2006 December 20, 2006 February 13, 2007 March 13, 16, 2007 April 23, 2007 August 7, 2007 March 9, 2008
Active Geomagnetic $Ap \geq 50$	April 17, 2002 October 1, 4, 2002	October 29, 2003	July 23, 25, 2004

Similarly for GRACE, a total of 20 days were examined. However, unlike CHAMP, data corresponding to elevated and high solar activity levels were not available and hence only

two solar activity bins - low and moderate were examined. The days examined were within the lifetime of both CHAMP and GRACE, but not necessarily the same days. This was done to have a fair distribution of days with whatever data was available for GRACE. These days are shown in Table 2.4 under their respective solar and geomagnetic bins.

Table 2.4. Days examined for GRACE by Solar and Geomagnetic activity Bins.

Activity Level Bin	GRACE Mission Life	
Low Solar F10.7 < 75	October 27, 2005 August 4, 7, 2006 March 13, 2007 February 4, 2008	
Moderate Solar $75 \leq$ F10.7 < 150	November 9, 2004 March 9, 18, 2005 April 7, 2005 May 10, 13, 2005 August 2, 2005 September 11, 20, 2005	November 17, 2005 December 7, 2005 January 21, 26, 2006 February 3, 2006 April 28, 2007
Quiet Geomagnetic Ap $\leq$ 10	April 7, 2005 May 10, 2005 August 2, 2005 September 20, 2005 October 27, 2005	December 7, 2005 January 21, 2006 February 3, 2006 August 4, 2006 February 4, 2008
Moderate Geomagnetic 10<Ap<50	March 9, 18, 2005 May 13, 2005 January 26, 2006 August 7, 2006 March 13, 16, 2007 April 28, 2007	
Active Geomagnetic Ap $\geq$ 50	November 9, 2004 September 11, 2005	

2.9.1 Linear Weighted Blending Technique

For a 14 hour solution fit span, there are two overlap regions. The first overlap period is for the first two hours of the fit span under study, with the last two hours (13^{th} and 14^{th} hours) of the preceding 14 hour fit span. The second one is for the last two hours (13^{th} and 14^{th} hours) of the fit span under study, with the first two hours of the succeeding 14 hour fit span. Supposing the 14 hour fit span under study is from 10:00 hours to 24:00 hours then the first overlap region is from 10:00 hours to 12:00 hours, while the second overlap region is from 22:00 hours to 24:00 hours. To calculate the average value for all these data points under the overlap region, and also to maintain continuity and smooth transition from one dataset to another, an arithmetic average can't be used. Thus, the linear weighted blending technique, with linear variation of the normalized weight was used. The weight for one data set decreased from a starting value of 1 to a final value of 0 in a linear fashion. Similar weights were assigned to the other data set, but in reverse, the first data point was assigned a weight of 0, while the last one was assigned 1. Thus, at given time within the overlap period, the sum of the weights of the two data points corresponding to that time will be equal to one. For the first two hours of the solution fit span under study, the weight assigned varies linearly from 0 for the first data point to 1 for the last data point. For the last two hours it varies from 1 to 0. For the example fit span above, this translates to having a weight of 0 for the data point at 10:00 hours, and a weight of 1 for the data point at 12:00 hours, with linear variation in between. Similarly for the last two hours, the weight assigned to the data point at 22:00 hours is 1, while it is 0 for data point at 24:00 hours.

The density estimate is expected to be worse near the end of the data sets since there is less data around the time of the estimate. This is another reason for using the linear weighted blending technique so as to improve the accuracy near the ends of the data sets.

An illustration of this method is displayed in Figure 2.1 and Figure 2.2 by blending the first two and last two hours of a 14 hour density estimate fit span under study using the linear weighted blending technique from 22 hours, 29 October 2003 to 12 hours, 30 October 2003.

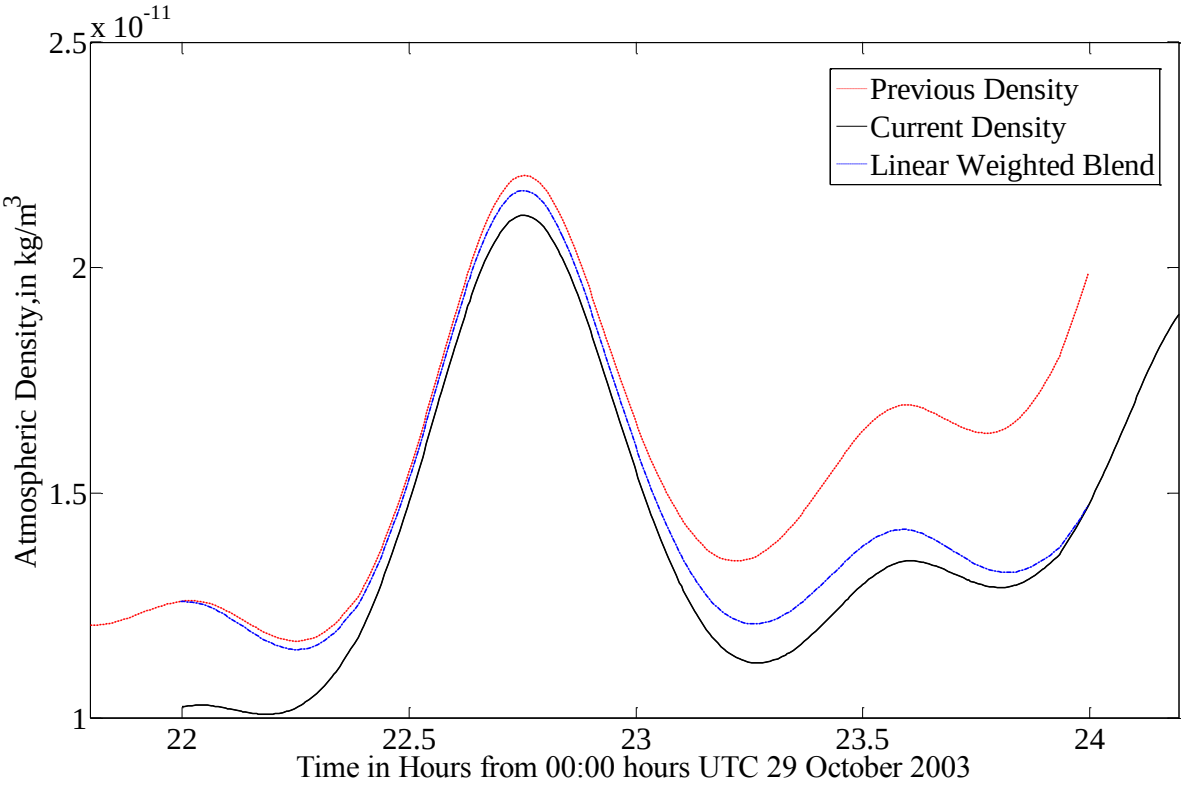

Figure 2.1: The density estimate for the fit span under study (22 hr 29th to 12 hr 30th Oct. 2003), the preceding fit span, and their blended density for the two hour overlap period (22 hr to 24 hr 29th Oct. 2003)

.

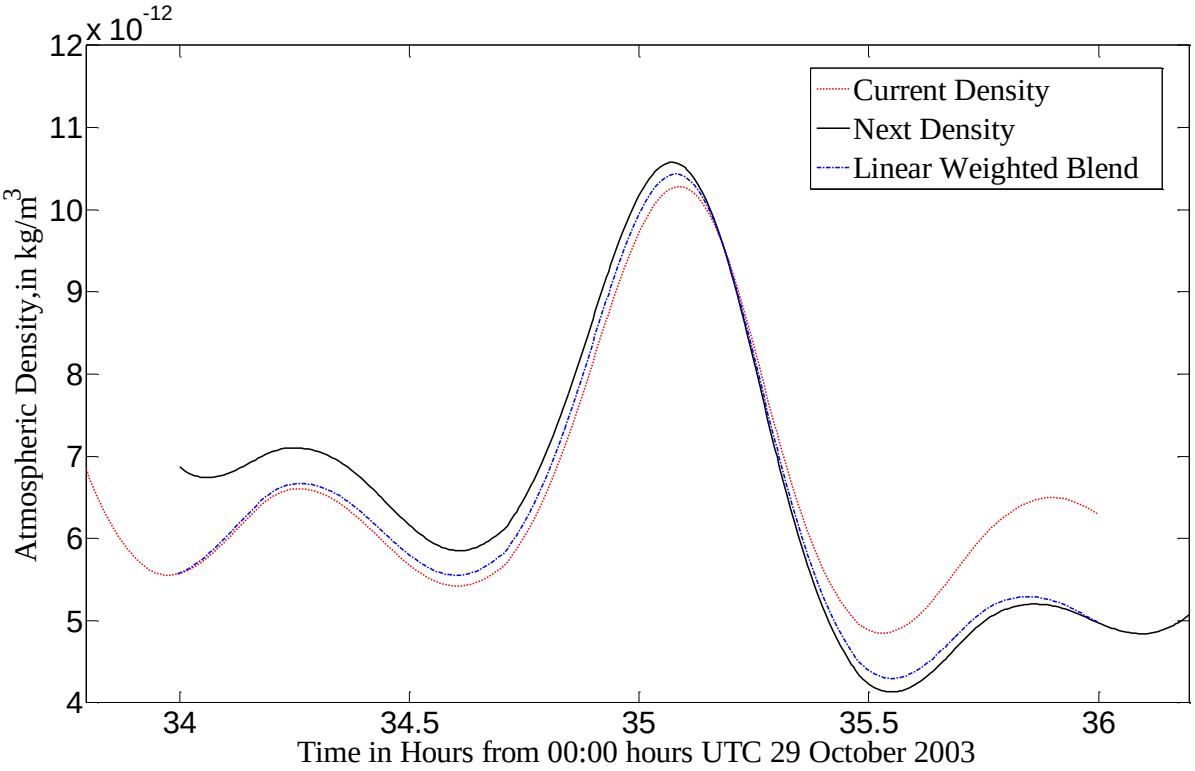

Figure 2.2. The density estimate for the fit span under study (22 hr 29th to 12 hr 30th Oct. 2003), the succeeding fit span, and their blended density for the two hour overlap period (10 hr to 12 hr 30th Oct. 2003).

Figure 2.1 and Figure 2.2 show the smooth and continuous transition from the end of one fit span to the beginning of the next one. This would not be possible if a simple average was used between the two fit spans.

A similar procedure was adopted to bridge the position vector. Figure 2.3 shows the X-component of position vector obtained by applying the linear weighted blending technique for the first two hours of a 14 hour density estimate fit span under study from 22 hours, 29 October 2003 to 12 hours 30, October 2003.

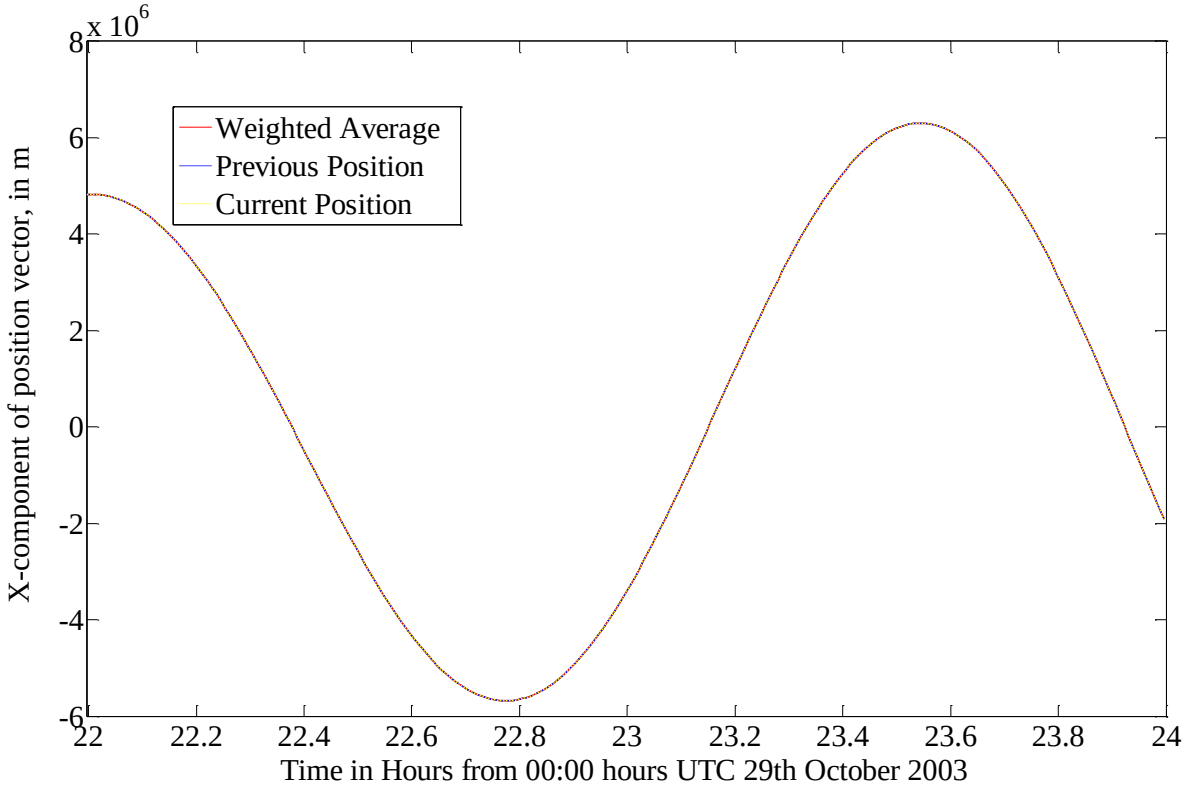

Figure 2.3. The X-component of position vector for the fit span under study (22 hr 29th to 12 hr 30th Oct. 2003), the preceding fit span, and their blended position for the two hour overlap period (22 hr to 24 hr 29th Oct. 2003).

Figure 2.3 shows all the three different sources of position, which are position from the dataset corresponding to the current and preceding scenario and the linear weighted blending of those two scenarios. The three different sources of position appear to coincide because the difference between the two positions at any given time during the overlap period from the scenarios was very small, on the order of 1 cm.

2.10 Area Normal to Velocity, Earth, and Sun Vector for TerraSAR-X

One of the objectives of this research is to find an average cross sectional area that is normal to the velocity vector, the area facing the Sun, and the area facing the Earth, so that

these areas can be used to estimate the atmospheric drag, solar radiation pressure, and Earth radiation pressure (infrared and Earth albedo), respectively.

The specifications of the TerraSAR-X satellite and its orbit that are relevant to obtain these areas are tabulated in Table 2.5.

Table 2.5: Some of the characteristics of TerraSAR-X satellite mission [Ref. 76]

Parameter	Value
Length	4.88 meters
Diameter	2.4 meters
Inclination (with respect to the equator)	97.44 degrees
Type of orbit	Sun-synchronous, dawn-dusk orbit

The cross sectional area normal to the velocity vector is nothing but the area of the TerraSAR-X projected on to a plane normal to the longitudinal axis of the satellite, which happens to align closely with the velocity vector. This area was specified as 3.1 m^2 (A_{drag}) based on a personal correspondence with Dr. Wolters of ASTRIUM and is shown in Figure 2.4 [Ref. 77].

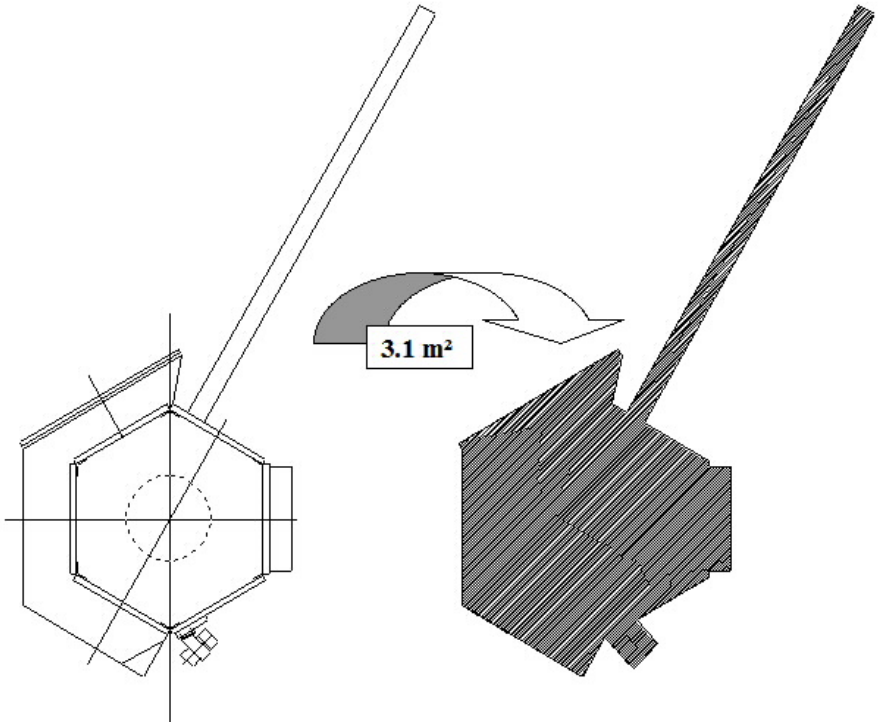

Figure 2.4: The frontal cross section area of TerraSAR-X [Ref. 77].

In order to determine the length of the sides in Figure 2.4–so as to estimate the area facing the Earth and the Sun–an assumption that the entire frontal face is composed of two half regular hexagon was made. The left part is the larger hexagon while the right part is the smaller one. The contribution of the projected area of the boom to the total frontal cross sectional area can't be ignored since it may have a significant contribution since it has a fair size cross section as seen in Figure 2.4. Thus the size of the boom is also estimated.

The diameter of the larger hexagon (one towards the left) is given as 2.4 meters [Ref. 76]. The area of a regular hexagon with a diameter of 2.4 meters is 3.74 m^2 and half of which is about 1.87 m^2, which is the area of the larger hexagon. The remaining area, which is the difference between the total frontal area (3.1 m^2) and the half the area of larger hexagon (1.87 m^2) is thus 1.23 m^2. This is illustrated in Figure 2.5.

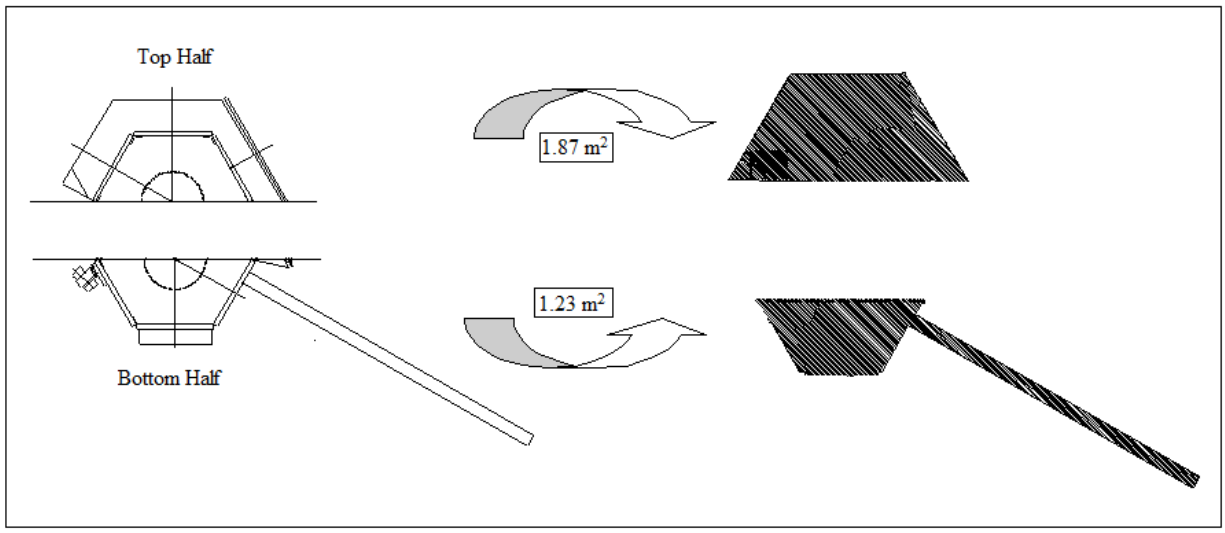

Figure 2.5: Approximate areas of the top and bottom half.

Since Figure 2.4 is to scale, the diameter of the boom was found to be about one fifth the length of the side of the smaller hexagon and the length of the boom equal to 4.13 times the length of the side of the smaller hexagon. This gives the following relation for the sum of the areas of half the hexagon and boom.

$$1.23 = \frac{1}{2} A_{Hexagon} + A_{Boom} = \frac{1}{2}\frac{3\sqrt{3}}{2} a^2 + \frac{1}{15} a \times 4.13a = 2.1257a^2 \qquad (2.3)$$

This gives a value of ***a*** (side of the smaller hexagon) equal to 0.76 meters. Thus the size of the boom is 0.15 meters (diameter) and 3.14 meters (length). Thus the cross sectional area of the boom is 0.48 m^2. The approximate dimensions of the simplified frontal surface, formed by two different half regular hexagons and a boom are shown in Figure 2.6.

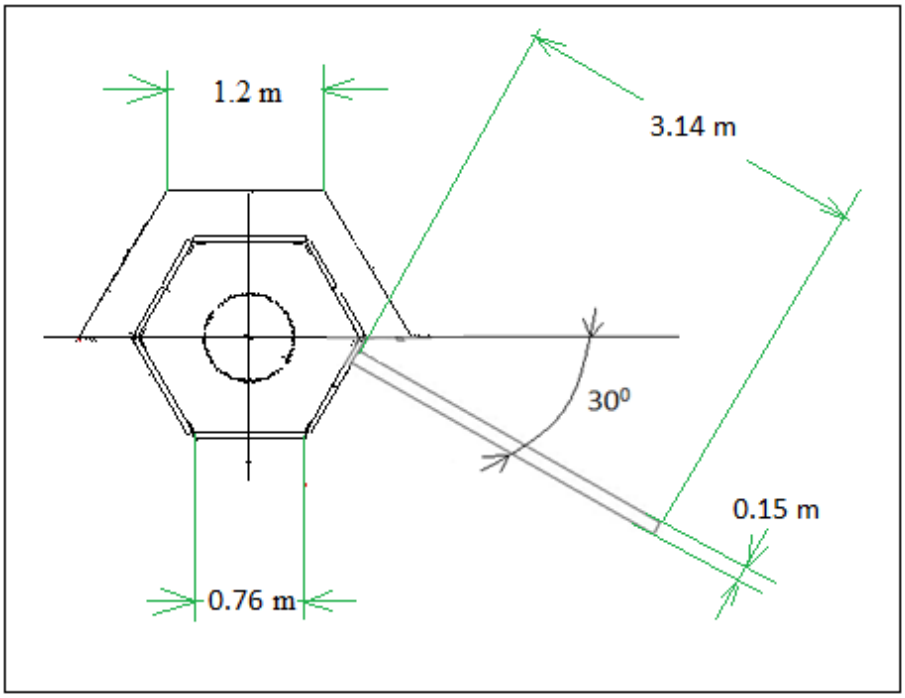

Figure 2.6: Approximate dimensions of the frontal cross section of TerraSAR-X.

The design attitude of TerraSAR-X relative to the surface of the Earth is shown in the schematic diagram in Figure 2.7.

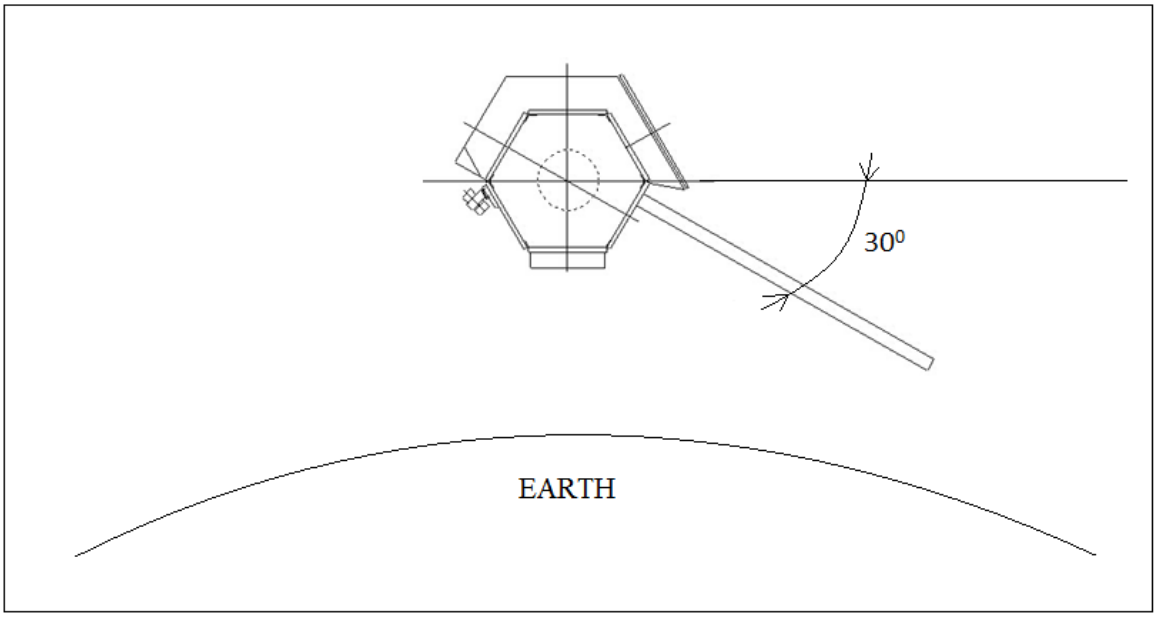

Figure 2.7: Attitude of TerraSAR-X relative to Earth's surface. Figure not to scale.

Thus the projected area of TerraSAR-X for the side facing the Earth will be the sum of the product of the diameter (2.4 m) and the length of the satellite (4.88 m), and the projection for the boom area on to the plane parallel to the Earth. This results in an area equal to 12.13 m^2 ($A_{\oplus}$).

The area facing the Sun is the projection of the satellite area on to a plane normal to the line joining the center of Sun to the center of Earth, which is the simply the plane normal to the ecliptic of the Earth. Thus, the projected area is clearly a function of the beta angle (the angle from the ecliptic to the satellite orbit plane). The projected area for four different beta angles corresponding to summer solstice, fall equinox, winter solstice, and spring equinox were examined so as to come up with a yearly average of the projected area. Since the inclination of TerraSAR-X is constant with a value of 97.44^o and it's also in a sun-synchronous dawn-dusk orbit, the plane of the orbit is always facing the Sun. This means the angle between the line joining the center of the Sun and the Earth, and the satellite plane angular momentum vector (normal to the satellite orbit plane) measured along the ecliptic is always zero (which is equivalent to stating that the line formed by the intersection of the ecliptic plane and the satellite orbit plane is normal to the Sun-Earth vector).

Before determining the beta angle and thus the projected area, the area of the TerraSAR-X facing toward the Sun (but not normal to it), the contribution of the satellite to the projected surface normal to the ecliptic is to be determined. The schematic diagram showing this orientation is shown in Figure 2.8.

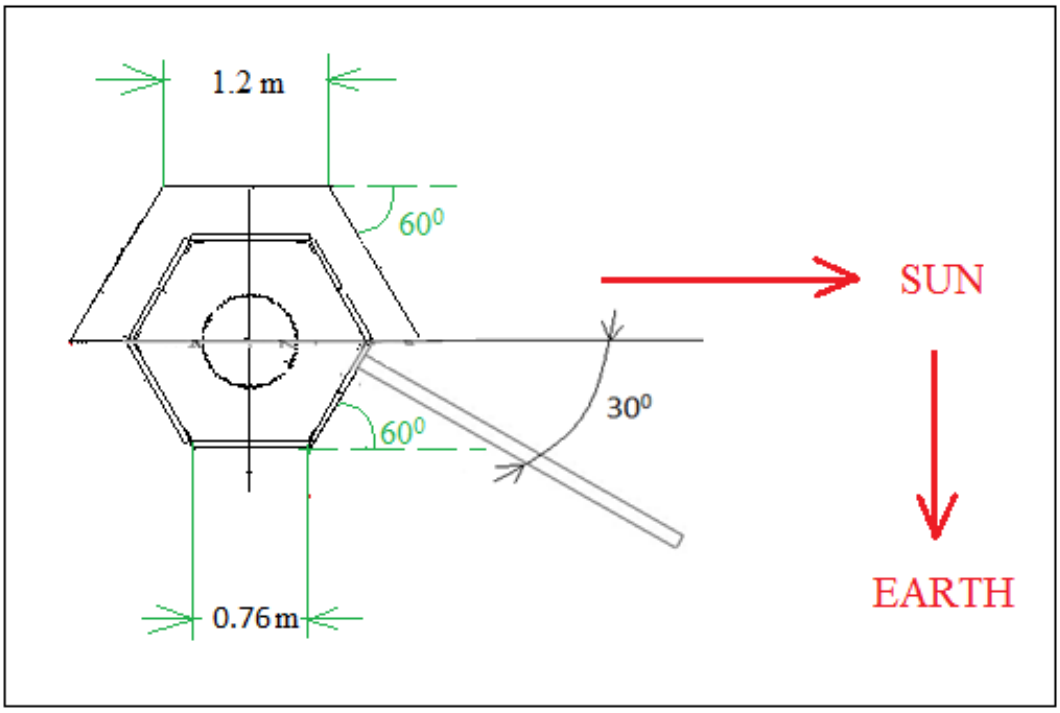

Figure 2.8: Direction of Earth and Sun relative to the TerraSAR-X frontal cross section.

The area facing the Sun is the projection of the top 'plate/rectangle' with a breath of 1.2 m and a length of 4.88 m, the projection of the bottom 'plate/rectangle' with a breadth of 0.76 m and a length of 4.88 m, and the projection of the boom. Thus the total projected area towards the Sun was calculated from the expression below.

$$A'_{\odot} = 4.88 \times (1.2 + 0.76)\sin\left(60^0\right) + 0.48 \times \sin\left(30^0\right) = 8.52 \text{ m}^2$$

Depending on the beta angle, the projection of this area and the frontal area on to the plane normal to the ecliptic can be determined.

During summer solstice, the beta angle is 73.94^0 and the orientation of the satellite relative to the ecliptic and the normal to the ecliptic is shown in Figure 2.9.

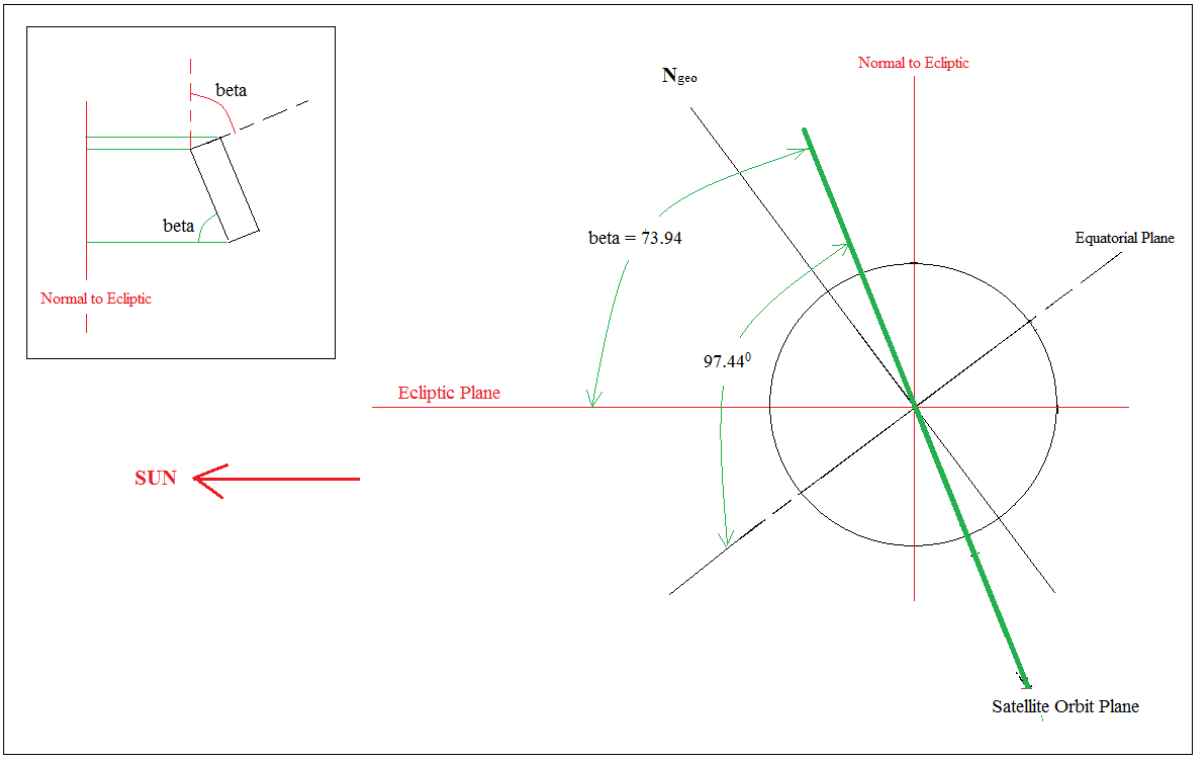

Figure 2.9: Geometry of the TerraSAR-X orbit plane relative to the ecliptic and inset figure showing orientation of the TerraSAR-X relative to the normal to the ecliptic as seen from the edge of the satellite orbit plane during summer solstice.

From Figure 2.9, the area projected normal to the plane of the ecliptic was calculated as,

$$A_{\odot}^{\text{summer}} = A_{\text{drag}}\cos(\beta) + A'_{\odot}\sin(\beta) = 3.1\cos(73.94) + 8.52\sin(73.94) = 9.05\ \text{m}^2$$

During winter solstice, the beta angle is 120.94^0 (measured from the line joining the centers of the Earth and Sun, and the satellite orbit plane), or equivalently 59.06^0 when measured between the ecliptic plane and satellite plane but measured from the 'dark side' of the Earth. The orbit plane geometry and the orientation of the satellite relative to the normal to the ecliptic are shown in Figure 2.10.

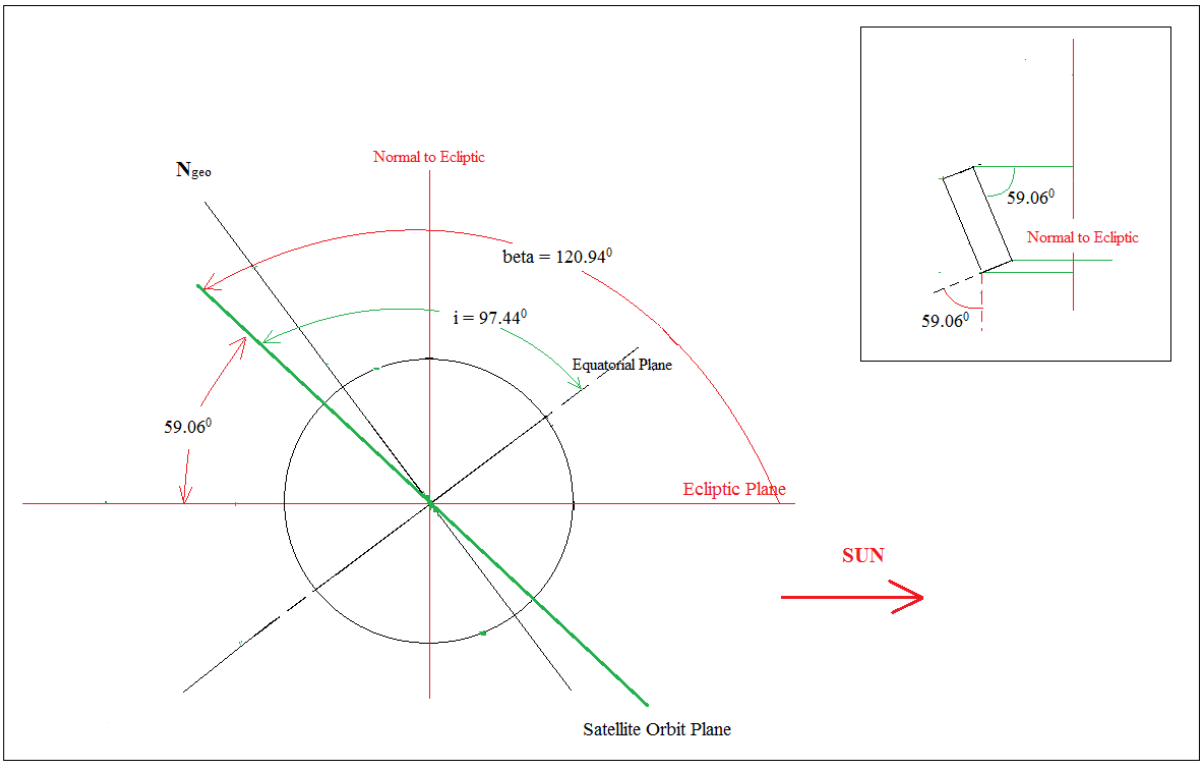

Figure 2.10: Geometry of the TerraSAR-X orbit plane relative to the ecliptic and inset figure showing orientation of the TerraSAR-X relative to the normal to the ecliptic as seen from the edge of the satellite orbit plane during winter solstice.

From Figure 2.10, the area projected normal to the plane of the ecliptic was calculated as,

$$A_{\odot}^{\text{winter}} = A_{\text{drag}} \cos(180-\beta) + A'_{\odot} \sin(180-\beta) = 3.1\cos(59.06) + 8.52\sin(59.06) = 8.91 \text{ m}^2$$

During both the fall and spring equinox, the plane normal to the ecliptic will pass through the axis of Earth's rotation and therefore the beta angle will be equal to the inclination, which is 97.44^0. Thus, for both the equinoxes, the projected area was calculated using,

$$A_{\odot}^{\text{equinox}} = A_{\text{drag}} \cos(180-\beta) + A'_{\odot} \sin(180-\beta) = 3.1\cos(82.56) + 8.52\sin(82.56) = 9.51 \text{ m}^2$$

Thus, the yearly average area normal to the Sun vector is the average of $A_{\odot}^{\text{summer}}$, $A_{\odot}^{\text{winter}}$, and $2 \times A_{\odot}^{\text{equinox}}$, and is equal to $A_{\odot} = 8.92 \text{ m}^2$.

Based on the above analysis one can see that the general equation to obtain the area normal to the Sun at any given beta angle is given by the following equation.

$$\boxed{\begin{aligned} A_{\odot} &= A_{drag}\cos(\beta) + A'_{\odot}\sin(\beta) \text{ , when } \beta<90^0 \\ A_{\odot} &= A_{drag}\cos(180-\beta) + A'_{\odot}\sin(180-\beta) \text{ , when } \beta>90^0 \end{aligned}} \tag{2.4}$$

2.11 Attitude Determination for ICESat

This section deals with estimation of the attitude of the ICESat satellite at times when Precision Orbit Ephemerides (POE) are available. By estimating its attitude, the area facing the Sun, Earth, and direction of flight (normal to the velocity vector) can be determined, which will be useful in modeling the forces acting on the satellite. The estimated areas are used as inputs to ODTK, along with the POE data, which are input as measurements, and then ODTK estimates corrections to baseline atmospheric density models and ballistic coefficients along the path of the satellite using optimal orbit determination. The current feature in ODTK does not allow the user to input the values of critical areas at each observation where POE are available. Thus, an average value of the critical areas for a scenario has to be used as the input. Since each scenario for ICESat spans 30-hours, the average critical areas are the average of the area facing the Sun, Earth, and normal to the velocity vector for this duration of 30-hours.

The attitude of ICESat is a function of the angle between the line joining the center of Earth to the center of the Sun (position vector of the Sun in International Celestial Reference Frame), and the plane of the satellite orbit. The details of which are given in a PhD dissertation by C. E. Webb [Reference 78]. Using this information, a computer program was developed in MATLAB capable of calculating the design attitude based on the time and the state vector, which was available from the University of Texas Center for Space Research.

2.11.1 ICESat Geometry

Finding the projection of the satellite on a 2-D plane that is normal to any specified direction vector is challenging since it involves a complete understanding of the geometry of the satellite and its relation to the coordinate axis. The complexity can be reduced by adopting a simpler model of the satellite. The type of model depends on the actual geometry of the satellite as well as the accuracy required. The following figure illustrates the complexity in using the actual geometry of ICESat to obtain its projection on a 2-D plane. The 2-D planes of interest in this research are: the plane normal to the Sun direction vector, normal to the Earth direction vector (or nadir), and normal to the satellite's velocity vector.

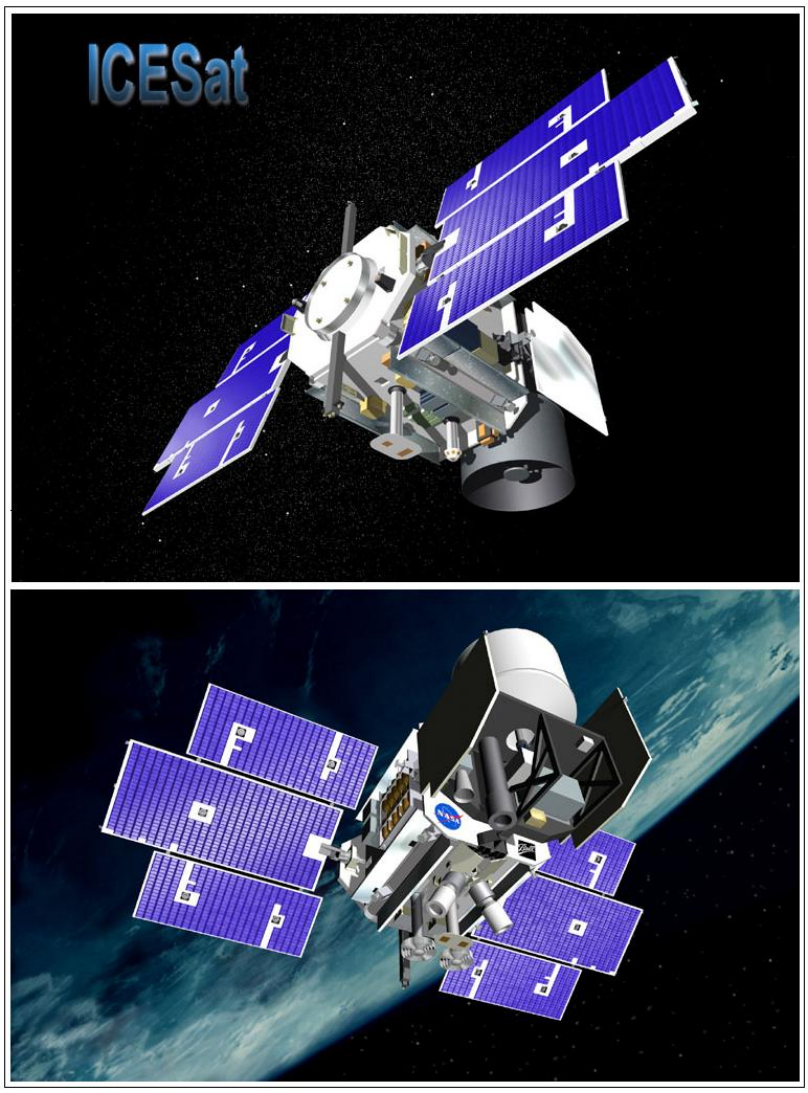

Figure 2.11: Illustration of ICESat as seen from two different views [Ref. 79].

One such way is to develop a micro-model of ICESat which includes as many details as possible, and was actually developed by the Ball Aerospace and Technologies Corporation (BATC) as a prelaunch version and details of which are given in Reference 78. It consists of 950 surfaces, which includes flat plates, cones and cylinders, and each of these was oriented with respect to the Satellite Coordinate System (SCS). The larger surfaces were further

subdivided resulting in a total of 2,058 nodes [Ref. 78]. This model proved to be too complex for the current study. This micro-model is illustrated in Figure 2.12.

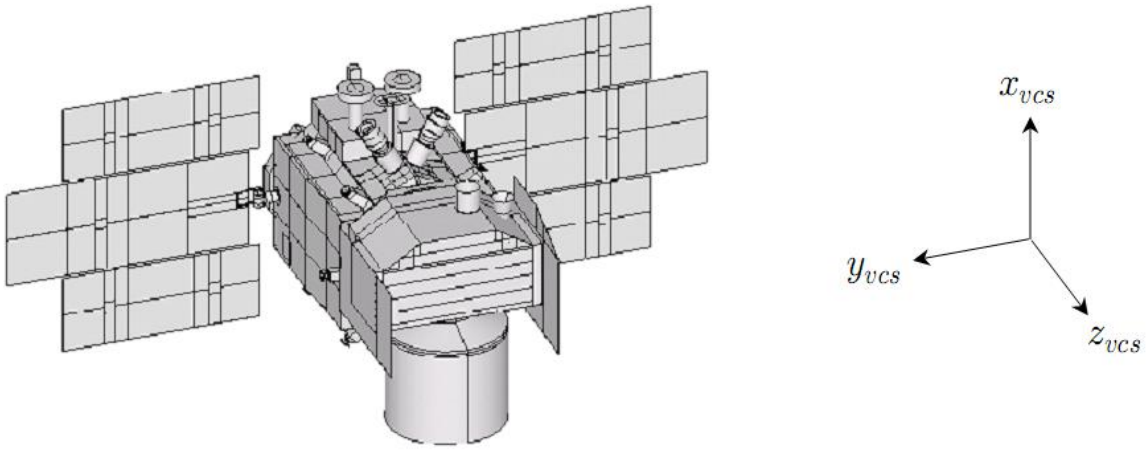

Figure 2.12: Micro-model of ICESat with 950 surfaces and 2,058 nodes [Ref. 78].

Since the current study requires approximate projections and because the details of this micro-model are not available, a decision to develop a satellite macro-model was made. This model consists of a six sided 'box' or a cuboid that models ICESat's bus, and two double sided 'wing' or flat plates that model ICESat's two sets of solar arrays (one set is considered to be the combination of three solar arrays on one side of the spacecraft). This forms a total of 10 surfaces (6 surfaces forming the cuboid body and 4 surfaces forming the two sides of both the solar arrays) which are all flat. This model appears in Figure 2.13.

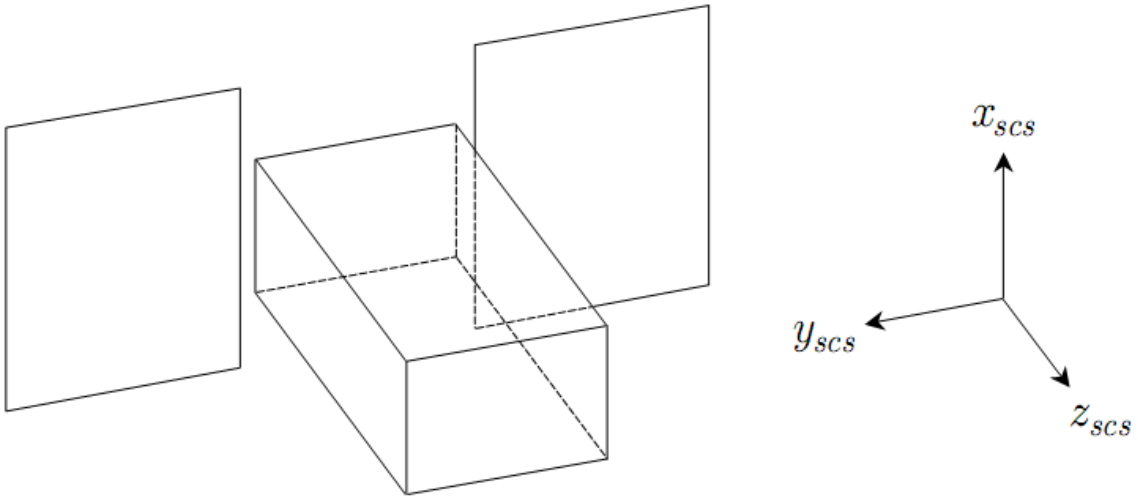

Figure 2.13: Macro-model of ICESat with 6 flat surfaces forming a cuboid body and 4 flat surfaces forming 2 solar arrays, along with the satellite coordinate system [Ref. 78].

Figure 2.13 also shows the orientation of this macro-model in the SCS. The area of each of these surfaces is ideally the projected areas of various components on the surface under consideration (the projections from the corresponding parts of the micro-model shown in Figure 2.12). However, in Reference 78, the author calculates these areas in a different way, which is briefly described below. The author used the Thermal Synthesizer System (TSS) for simulating a circular orbit of altitude equal to 600 km, with β' equal to 0^0 (aligning the orbit plane with the ecliptic) and then placing the ICESat micro-model at the ascending node, with each of its SCS axes pointing towards the Sun in turn. The heat rate for each orientation was calculated by summing over the nodes that are facing the Sun, and this is divided by the constant solar irradiance to yield the effective area of the desired macro-model surface. The areas obtained in this fashion are illustrated in Figure 2.15 to Figure 2.19.

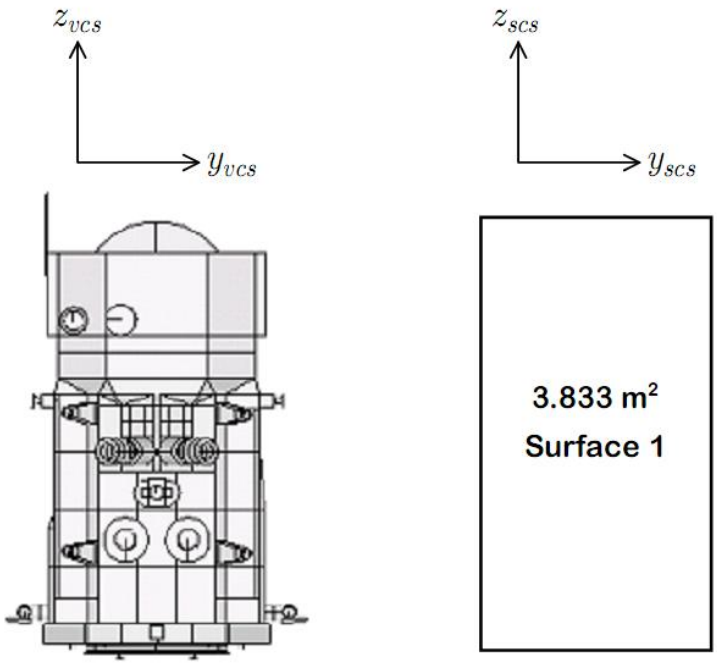

Figure 2.14: Projected area normal to $+x_{scs}$ axis: Micro-Model (left) and Macro-Model (right) [Ref. 78].

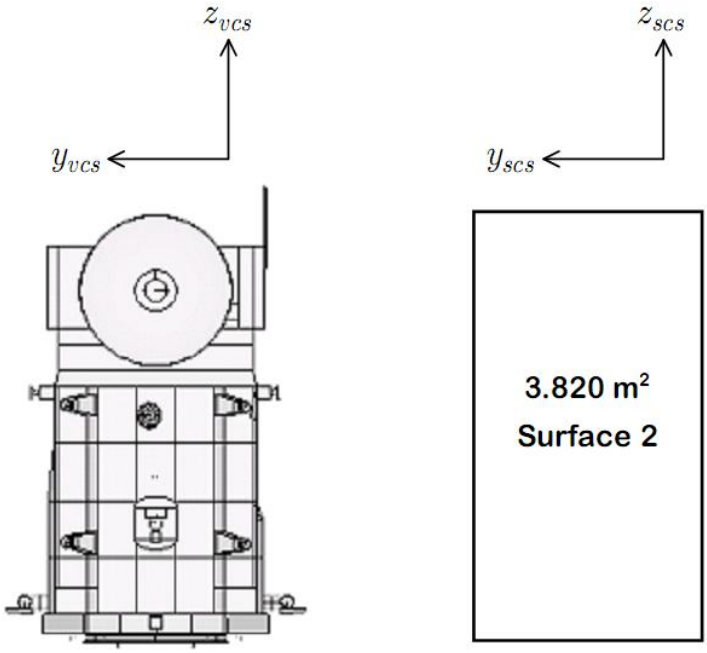

Figure 2.15: Projected area normal to $-x_{scs}$ axis: Micro-Model (left) and Macro-Model (right) [Ref. 78].

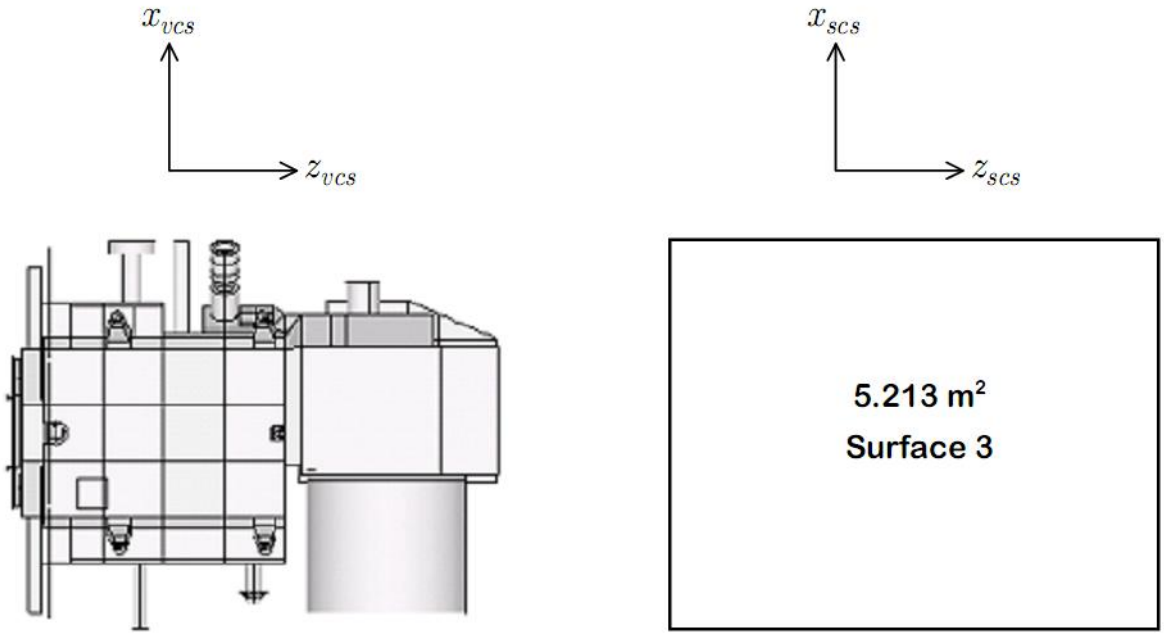

Figure 2.16: Projected area normal to +y_{scs} axis: Micro-Model (left) and Macro-Model (right) [Ref. 78].

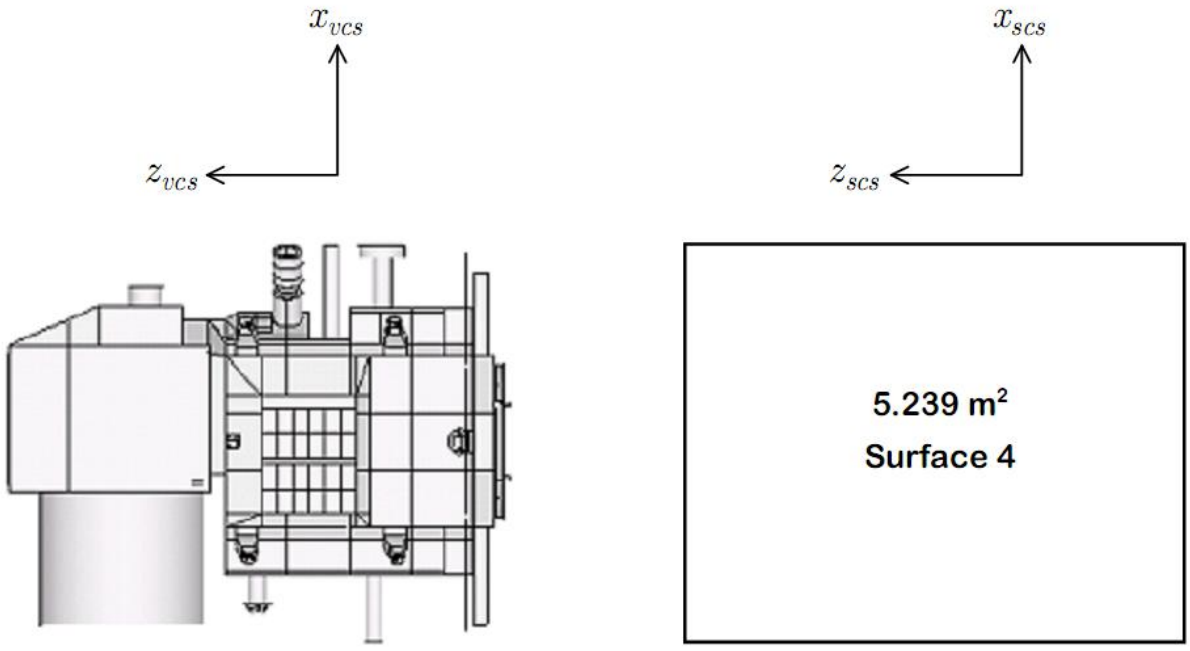

Figure 2.17: Projected area normal to -y_{scs} axis: Micro-Model (left) and Macro-Model (right) [Ref. 78].

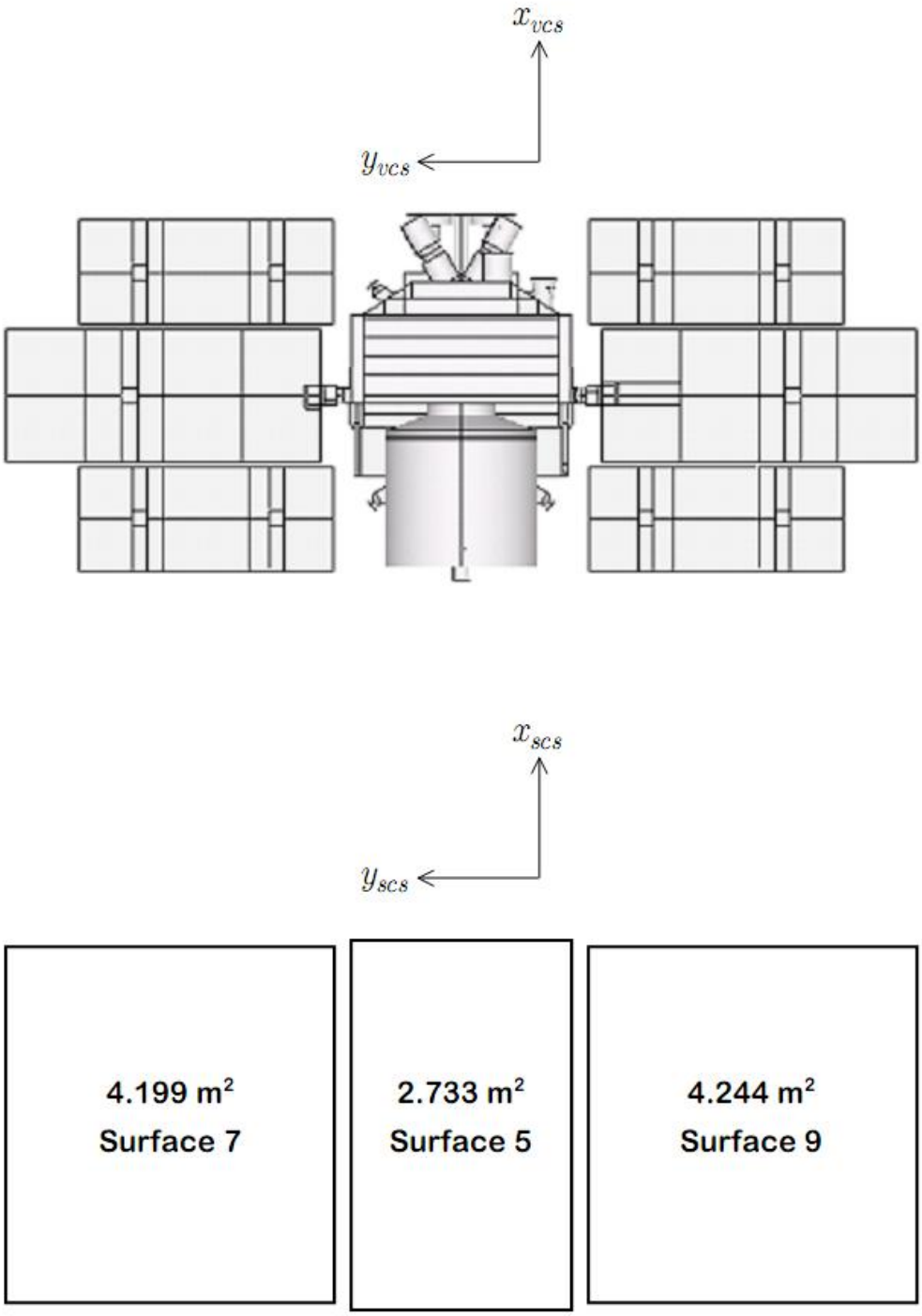

Figure 2.18: Projected area normal to $+z_{scs}$ axis: Micro-Model (left) and Macro-Model (right) [Ref. 78].

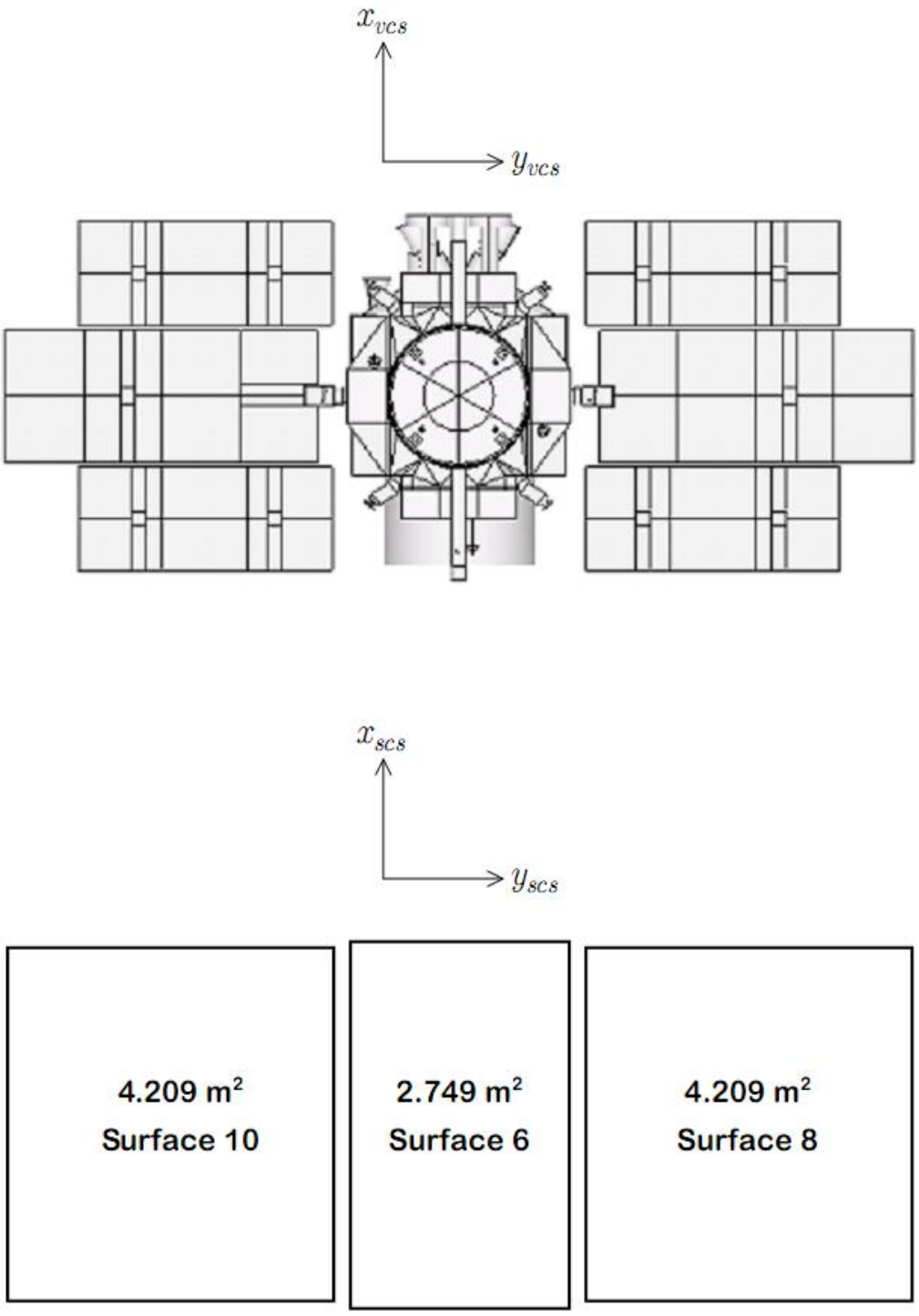

Figure 2.19: Projected area normal to -z_{scs} axis: Micro-Model (left) and Macro-Model (right) [Ref. 78].

These areas are well suited for calculating the projected areas normal to the Sun direction vector and Earth direction vector, since both of them interact with the surfaces in a similar fashion (by radiation pressure). However, the atmosphere acts on the surface by impinging particles on the surface and hence the projected areas of various components on the surface under consideration would be more accurate for this application. But the difference would be too small to affect the accuracy demanded in this study, and hence the same areas were used for calculating the areas normal to the velocity vector.

2.11.2 Satellite Design Attitude

Depending on the angle between the Sun's position vector (in ICRF) and the orbit plane, the satellite assumes one of the four yaw orientations, or control frames. This angle β' is shown in Figure 2.20.

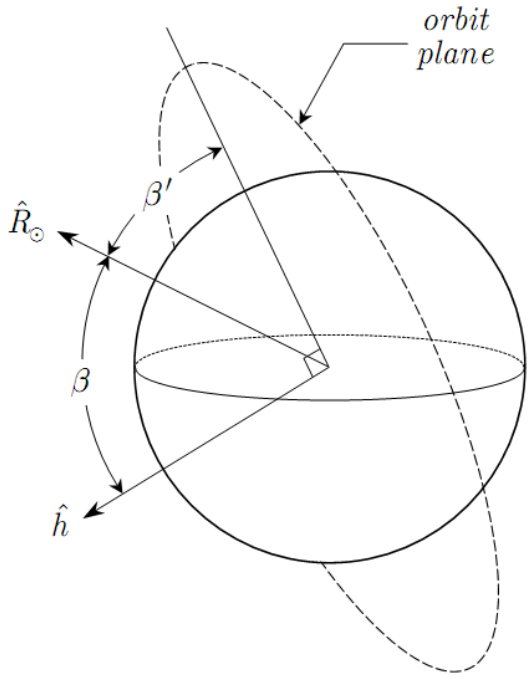

Figure 2.20: Beta angle, β, for a satellite orbit plane [Ref. 78].

This angle is the complementary angle between the Sun direction vector and the specific angular momentum vector of the orbit plane, β. For an orbit plane having $\hat{h}$ as its specific angular momentum unit vector, and $\hat{R}_{sun}$ as the Sun direction unit vector, from the geometry, the expression for β' is given by the following equation.

$$\beta' = \frac{\pi}{2} - \cos^{-1}\left(\hat{h} \cdot \hat{R}_{sun}\right) \tag{2.5}$$

The four possible yaw orientations or control frames are shown in Figure 2.21.

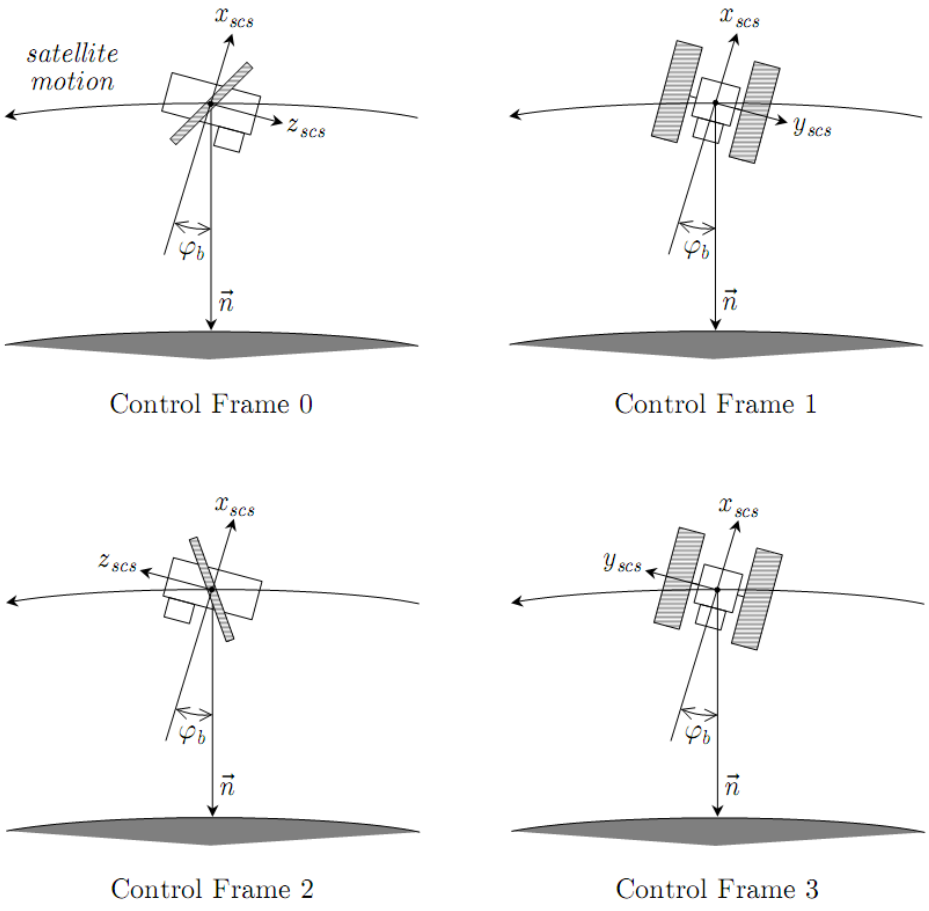

Figure 2.21: The four possible yaw orientations or control frames for ICESat [Ref. 78].

These four control frames are a function of β' and depending on the range of β', the satellite assumes one of the above control frames. The range of β' for which the satellite assumes a certain control frame is given in Table 2.6, along with the yaw orientation.

Table 2.6: Range of β' for which for which each type of control frame exists, and also the yaw angle for each control frame. The operational mode (airplane or sailboat) is also specified for each control frame [Ref. 78].

Control Frame	Operational Mode	Yaw Angle	β' Limits	
			Lower	Upper
0	Airplane	180^0	0^0	33^0
1	Sailboat	90^0	33^0	90^0
2	Airplane	0^0	-33^0	0^0
3	Sailboat	270^0	-90^0	-33^0

In Figure 2.21, $\vec{n}$ represents the geodetic-nadir pointing vector, and x, y, and z, with the subscript *scs* represent the orthogonal axis in the satellite coordinate system. The angle φ_b, is the pitch bias, designed to avoid the specular reflections of the laser pulses off the subject (surface of the Earth or atmosphere) and into the GLAS instrument. This angle is maintained at 5 miliradians. Table 2.6 shows the yaw angle for each of the control frames, which is also visible in Figure 2.21. For control frames 0 and 2, the operational mode is named the Airplane mode, because the axis of rotation of the solar array ($+y_{scs}$, from Figure 2.21) is perpendicular to the direction of motion, and since the arrays appear like the wings of an airplane. Similarly, for control frames 1 and 3, the axis of rotation of the solar array is along the direction of motion, giving the solar array the appearance of a sail, and therefore, these two modes are named the Sailboat mode.

With the knowledge of the position vector of the Sun and the satellite, β' can be calculated, and from that, the control frame and therefore the attitude of ICESat can be partially determined. Partially, because the attitude depends on the orientation of the solar array as well and this is a function of the direction of the Sun relative to the satellite coordinate system. Thus, a transformation matrix has to be used to convert the direction vector of the Sun from ICRF to SCS. The details of the transformation matrix are given in Reference 78, and only the matrix is given below.

$$T_{icrf}^{scs}\left(\psi,\varphi_b,t\right)=T_{lvlh'}^{scs}\left(\psi\right)\cdot T_{lvlh}^{lvlh'}\left(\varphi_b\right)\cdot T_{icrf}^{lvlh}\left(t\right) \tag{2.6}$$

Where, $T_{icrf}^{scs}\left(\psi,\varphi_b,t\right)$ is the transformation matrix, from ICRF to SCS, $T_{icrf}^{lvlh}\left(t\right)$ is the transformation from ICRF to the local-vertical local-horizontal (LVLH) frame given by,

$T_{icrf}^{lvlh}\left(t\right)=\left[\hat{r}' \quad -\hat{h} \quad -\hat{r}'\times\hat{h}\right]$ with $\hat{r}'=-\dfrac{\vec{n}}{|\vec{n}|}$ and $\hat{h}$ being the specific angular momentum unit vector. $T_{lvlh}^{lvlh'}\left(\varphi_b\right)$ represents the rotation about the pitch axis by an angle equal to the pitch bias, φ_b, given by,

$$T_{lvlh}^{lvlh'}\left(\varphi_b\right)=\begin{bmatrix}\cos\varphi_b & 0 & -\sin\varphi_b\\ 0 & 1 & 0\\ \sin\varphi_b & 0 & \cos\varphi_b\end{bmatrix}$$

And $T_{lvlh'}^{scs}\left(\psi\right)$ represents the rotation about the yaw axis equal to the yaw angle, ψ, given by,

$$T_{lvlh'}^{scs}\left(\psi\right)==\begin{bmatrix}1 & 0 & 0\\ 0 & \cos\psi & -\sin\psi\\ 0 & \sin\psi & \cos\psi\end{bmatrix}$$

2.11.3 Solar Array Articulation

The solar array articulation mechanism is programmed to track the Sun when the Sun is visible and track a fictitious Sun when the satellite is in the Earth's shadow, with certain exceptions, which will be discussed in the next section. The two solar arrays of ICESat are capable of rotating independently (though they rotate in unison) about the y_{scs} axis, and are shown in Figure 2.22.

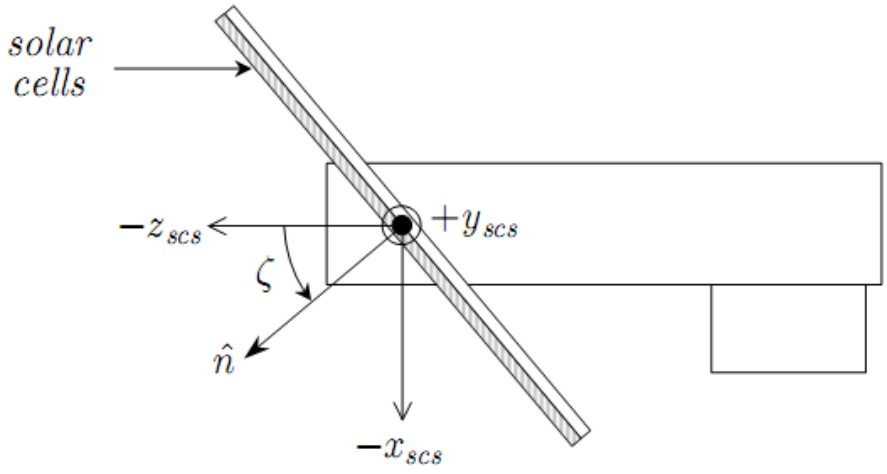

Figure 2.22: Orientation of the solar array with respect to $-z_{scs}$ axis [Ref. 78].

In Figure 2.22, ς is the angle of rotation measured from $-z_{scs}$ to $\hat{n}$, the unit vector normal to the solar array, and the range is from $+180^0$ to -180^0. The difference between the Sun position vector in ICRF and position vector of ICESat's center of mass (CM) in ICRF gives the position vector of the Sun relative to ICESat, but it would still be in ICRF. To get it in SCS, this position vector is multiplied by the transformation matrix $T_{icrf}^{scs}(\psi, \varphi_b, t)$, to obtain the position vector of the Sun in SCS. This procedure is given in the equations below, from Reference 78.

$$\vec{r}_{sun}^{\,icrf}(t) = \vec{R}_{sun}^{\,icrf}(t) - \vec{r}_{com}^{\,icrf}(t)$$
$$\vec{r}_{sun}^{\,scs}(t) = T_{icrf}^{scs}(\psi, \varphi_b, t).\vec{r}_{sun}^{\,icrf}(t) \tag{2.7}$$

If the components of this position vector in SCS are x_{sun}^{scs}, y_{sun}^{scs}, and z_{sun}^{scs}, then the rotation angle ς, for both the arrays is given by,

$$\varsigma(t) = \tan^{-1}\left[\frac{-x_{sun}^{scs}(t)}{-z_{sun}^{scs}(t)}\right] \tag{2.8}$$

The position vector of the Sun in ICRF, given in Equation (2.7) as $\vec{R}_{sun}^{\,icrf}(t)$, can be obtained at any time by using the Jet Propulsion Laboratory (JPL) DE-405 planetary ephemerides[§]. However, a much simpler and faster way was to compute these position vectors in ICRF using equations given in Reference 4. Also, the accuracy achieved from the latter method was sufficient for this study.

2.11.4 Solar Array Inhibition

As mentioned in the previous section, there are certain situations when the solar arrays do not track the Sun. One such situation is when ICESat is in the polar region, since moving the arrays in this zone may cause a slight disturbance to GLAS and thereby reduce the accuracy of the measurements. Thus, when ICESat crosses 60^0 on an ascending pass and -60^0 on its descending pass, the solar arrays are rotated to an angle ς_{stop}, and held at that position until it comes out of the 60^0 latitude or -60^0 latitude, for northern hemisphere or southern hemisphere, respectively. This stop angle, ς_{stop}, is such that it is the angle the arrays would have had at the midpoint of the pass, had they continued to articulate even after the 60^0 or -60^0 pass. This is done to reduce the time required for the solar arrays to continue tracking the Sun when they

[§] http://www.cv.nrao.edu/~rfisher/Ephemerides/ephem_descr.html

come out of the polar region. The situation is illustrated in Figure 2.23, which is from Reference 78.

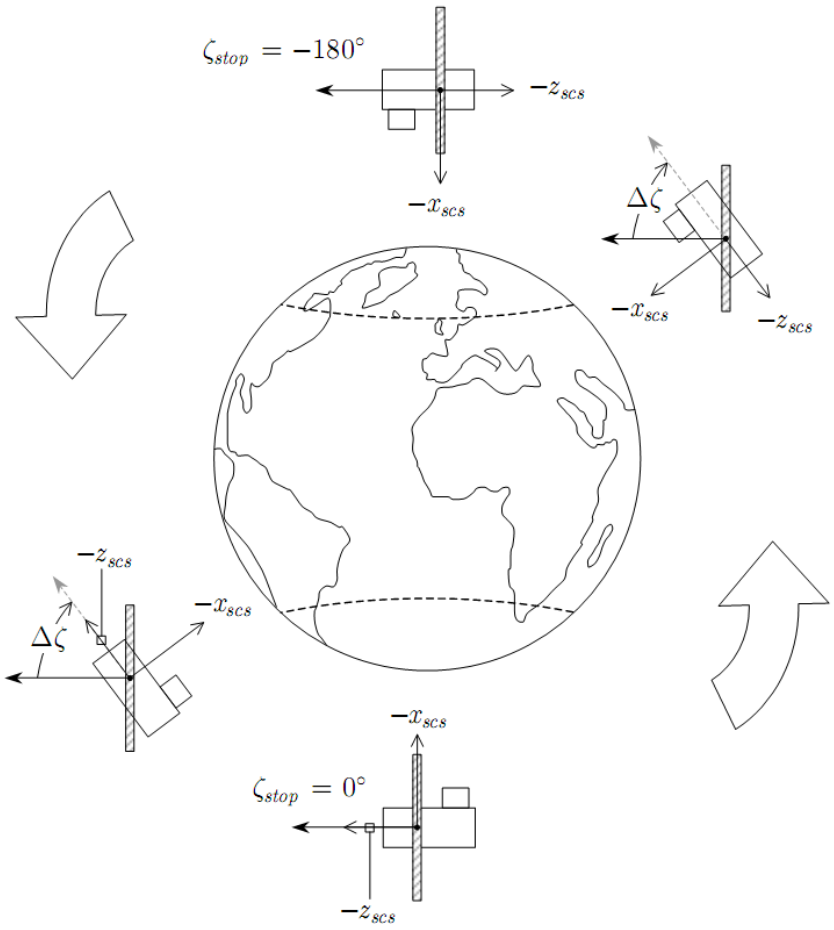

Figure 2.23: Inhibition of articulation of solar array in the polar regions [Ref. 78].

The stop angle can be found my integrating the state vector to find this future time and using Equations (2.7) and (2.8). However, the author of Reference 78 chooses another method, though approximate, the method is sufficiently accurate for this study. This method is briefly described below.

If t_0 is the time at which ICESat makes the +/-60^0 pass, then the time at which the satellite reaches the midpoint of the pass is the same as the time at which the satellite is at the apex (since the midpoint and the apex coincide) and can be predicted to be equal to

$$t_{apex} = t_0 + \frac{u_{apex} - u_0}{n_0} \tag{2.9}$$

Where n_0 is the mean motion at time, t_0, u_0 is the argument of latitude at time, t_0, and u_{apex} is the argument of latitude at the apex, which is equal to 90^0 for a northern pass and 270^0 for a southern pass. The author assumes that the right ascension of ascending node (Ω) and the inclination (***i***) do not change appreciably from time t_0 to t_{apex}, and hence uses the values at the former time to calculate the unit direction vector of the satellite CM. The equation to calculate the unit direction vector of ICESat's CM in ICRF is given in Reference 78 and reproduced below.

$$\hat{r}_{com}^{icrf}\left(t_{apex}\right) = \begin{bmatrix} \cos\Omega_0 \cos u_{apex} - \sin\Omega_0 \sin u_{apex} \cos i_0 \\ \sin\Omega_0 \cos u_{apex} + \cos\Omega_0 \sin u_{apex} \cos i_0 \\ \sin u_{apex} \sin i_0 \end{bmatrix} \tag{2.10}$$

The position vector is then simply the product of the unit direction vector and the semi-major axis given by $\vec{r}_{com}^{icrf}\left(t_{apex}\right) = a_0 \cdot \hat{r}_{com}^{icrf}\left(t_{apex}\right)$, and the position vector of the Sun in ICRF relative to the satellite is obtained by subtracting the above result from the position vector of the Sun in ICRF; and finally, the Sun vector is converted to SCS by using the transformation matrix. These steps are given in the equations below, which are reproduced from Reference 78.

$$\vec{r}_{sun}^{icrf}\left(t_{apex}\right) = \vec{R}_{sun}^{icrf}\left(t_{apex}\right) - \vec{r}_{com}^{icrf}\left(t_{apex}\right)$$
$$\vec{r}_{sun}^{scs}\left(t_{apex}\right) = T_{icrf}^{scs}\left(\psi, \varphi_b, t_{apex}\right) \cdot \vec{r}_{sun}^{icrf}\left(t_{apex}\right)$$

And similar to Equation (2.8), the stop angle is given by

$$\varsigma_{stop} = \varsigma\left(t_{apex}\right) = \tan^{-1}\left[\frac{-x_{sun}^{scs}\left(t_{apex}\right)}{-z_{sun}^{scs}\left(t_{apex}\right)}\right] \tag{2.11}$$

The second situation is when the β' is greater than 55^0 (Northern Hemisphere), or is less than -55^0 (Southern Hemisphere), wherein ICESat is in sailboat mode, and the Sun is nearly perpendicular to the arrays, and thus they are not articulated and held at $\varsigma=0^0$.

There are other situations in which articulation of the arrays is inhibited during passes involving a Target Of Opportunity (TOO), during which the array motion was to be simply arrested during the pass and resumed after this [Ref. 78]. Since the start and stop times of passes involving TOO were unknown for this study, and also since this pass was much shorter than the polar passes, it was not taken into consideration while calculating the array angle.

2.11.5 Calculation of Areas Normal to the Sun, the Earth, and the Velocity Vector

With POE data for ICESat as the input, the attitude of ICESat at any time for which POE data are available can be calculated and from that the area of the satellite normal to the Sun's direction (for solar pressure calculation), normal to nadir (facing Earth, to calculate Earth albedo and Earth radiation pressure), and normal to the velocity vector (for atmospheric drag calculation) can be calculated. All this is done by developing a program in MATLAB, based on the method described in the previous subsections. The details are briefly described below.

The POE data available for ICESat are in the Geocentric Coordinate Reference Frame (GCRF) but to calculate β', the state vector has to be in ICRF. Thus, the POE data are transformed from GCRF to ICRF for each observation using the IAU-2000 Resolutions, the details of which are given in Reference 4. This data is available for a span of 30 hours, with measurements every 30 seconds. The Earth Orientation Parameters (EOP)[**] were obtained corresponding to the time of the first measurement of the data file under study. The Sun vector

[**] http://www.celestrak.com/SpaceData/

in ICRF was calculated for all the times at which the state vector of ICESat was available for that scenario. These two were used to calculate the β' and thus determine the control frame, which in turn defined the attitude of the body of ICESat. After appropriate transformation of the Sun vector from ICRF to SCS, the solar array angle ς was calculated. Since ς is a function of latitude, the latitude for each observation was calculated and for polar passes, ς_{sotp} was calculated.

To calculate ς_{stop}, the time t_0–the time at which the satellite crosses $+60^0$ for ascending passes and -60^0 for descending passes–has to be known. This was done by saving the latest time at which such a pass occurred. However, if the very first observation in the data file indicates that the satellite is already in the polar region, then there were two choices–either to let the user input t_0, if known; or integrate the state vector backwards in time, until the latitude was equal to $+60^0$ or -60^0 (depending on whether it was in the northern or southern hemisphere), using a 2-body model of Earth with J2 and atmospheric drag (using an exponential density model and an approximate and fixed ballistic coefficient). In most of the cases, the user will not know the value of t_0. Since equation (2.10) itself is an approximation, formulated so that integration can be avoided, using integration to find the time, t_0, would fail the purpose of using equation (2.10). An examination of equation (2.10) reveals that $\hat{r}_{com}^{icrf}\left(t_{apex}\right)$ is really an approximation using right ascension of the ascending node and inclination at time, t_0, instead of time, t_{apex}. Also, for ICESat, having a time averaged inclination of 94 degrees [Ref. 63] the regression of nodes is about 0.5 degrees per year (using only the J2 effect on the orbit plane) and since ICESat has an orbital period of about 101 minutes [Ref. 63], the time difference between t_0 and t_{apex} would not be more than 20 minutes and thus the right ascension

of the ascending node would not have changed more than 0.01 degrees. The change in inclination would also be low. Thus, if the first observation indicates that the satellite is already in the polar region, then instead of trying to estimate t_0 and then determine the right ascension of ascending node and inclination at that time, the program simply determines the right ascension of ascending node and inclination at the time of first observation of the data file, t. This time, t, happens to be in the polar region (and thus between time t_0 and either t_{apex} or the time of exit of the satellite from the polar orbit), and would yield a similar estimate of $\hat{r}_{com}^{icrf}\left(t_{apex}\right)$.

Finally, when both the control frame as well as ς are identified and calculated, respectively, the projection of all the 10 areas forming the surface of the ICESat macro model, on planes normal to the Sun direction vector, Earth direction vector, and velocity vector was calculated. While summing the projected areas, only the areas visible when viewed along the corresponding direction are considered since the others will be shadowed.

The program calculates the area for all of the time for which POE data are available. However, only one area can be input in ODTK, thus the average of each area is taken for an entire scenario (spanning 30 hours) and this value is used as the input in ODTK.

2.12 Drag Coefficients for TerraSAR-X and ICESat

To estimate POE derived densities, an initial nominal value of BC is required. This requires an estimate of the drag coefficient, the area normal to the velocity vector, and the mass of the satellite. For both TerraSAR-X and ICESat, the procedure to calculate the area normal to the velocity vector has been described in subsections 2.10 and 2.11. The masses of TerraSAR-X and ICESat are also assumed to be constant and equal to 1,230 kg [Ref. 62] and 970 kg [Ref.

63], respectively. The only step remaining is to estimate the drag coefficient. Estimating the drag coefficient for a satellite is a complex process that requires information such as the geometry of the satellite, surface properties of the satellite, temperature of the surface, temperature of the surrounding gas, molecular composition of the surrounding gas, and relative velocity of the satellite surface and surrounding gas. Since the objective of this research is to estimate the areas and not the drag coefficient of TerraSAR-X and ICESat, a rough estimate of drag coefficient is made and used.

Reference 74 has plots of drag coefficient of a cylinder as a function of altitude for three different L/D values for two different solar activity levels. The analytical expression for the drag coefficient in reference 74 was deduced from Sentman's analysis [Ref. 80]. Instead of using the analytical expression from reference 74, the plots in the same reference were used to estimate the drag coefficient of TerraSAR-X for simplicity. For this, TerraSAR-X was assumed to be a cylinder with a diameter (D) of 2.4 meter and length (L) of 4.88 meter, thus having a length to diameter ratio (L/D) of about 2.0. The plots of drag coefficient from reference 74 for solar minimum and solar maximum are reproduced in Figure 2.24 and Figure 2.25.

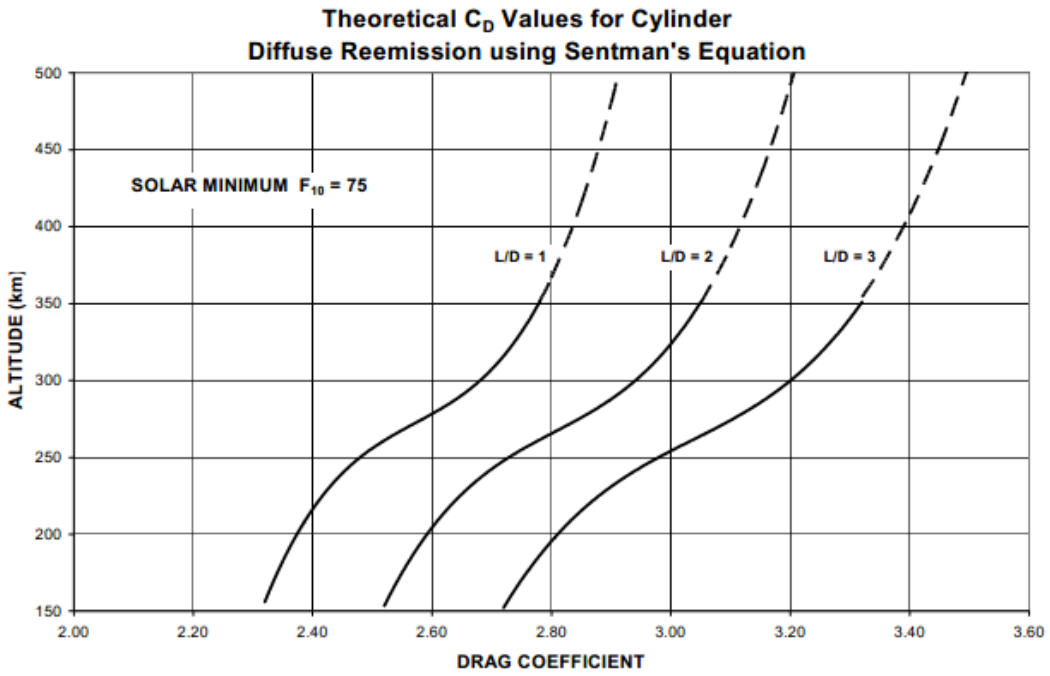

Figure 2.24: Theoretical value of drag coefficient for stabilized cylinders as a function of altitude for different L/D for solar minimum conditions [Ref. 74].

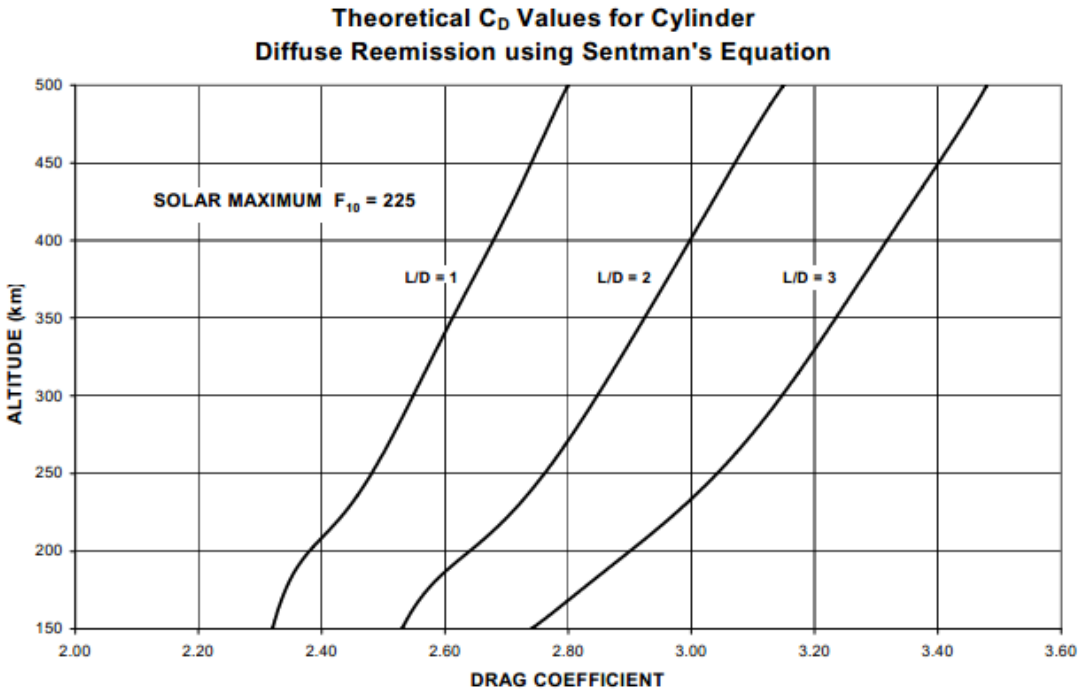

Figure 2.25: Theoretical value of drag coefficient for stabilized cylinders as a function of altitude for different L/D for solar maximum conditions [Ref. 74].

From Figure 2.24 and Figure 2.25, the drag coefficient for a cylinder with L/D equal to 2.0 is about 3.2, corresponding to an altitude of 514 km. Thus, the initial value of the drag coefficient of TerraSAR-X is chosen to be equal to 3.2.

Estimation of the drag coefficient of ICESat is relatively complex because ICESat contains two solar panels and the main body of the ICESat can be approximated as a cylinder, the attitude of which changes as a function of beta angle. Even a preliminary estimation of the drag coefficient of ICESat is beyond the scope of this research and is postponed for further research. A value of 2.6 is used for the drag coefficient of ICESat since this value was used by Arudra in reference 50, even though Arudra does not provide an explanation for using this value.

3 INVESTIGATING THE EFFECT OF DIFFERENT FUNCTIONS OF GEOMAGNETIC ACTIVITY PLANETARY AMPLITUDE (a_P) ON ESTIMATED ATMOSPHERIC DENSITIES

This section investigates the effect of different functions of geomagnetic planetary amplitude (a_p) as an input in orbit determination to estimate atmospheric density. The three different functions of input are 3-hourly a_p step functions, linear interpolated a_p functions, and a_p osculating spline functions.

Wright and Woodburn [Ref. 57] have shown that using 3-hourly step functions of geomagnetic indices fail the McReynold's filter/smoother consistency test, while the polynomial spline used to fit the 3-hourly step functions passes the same test. The algorithm used to obtain the osculating splines of 3-hourly step functions is presented by Tanygin and Wright [Ref. 73].

The effect of these functions on estimated atmospheric density is observed quantitatively by computing and comparing the zero delay CC and RMS with respect to the accelerometer derived densities, obtained by Sean Bruinsma of CNES. This accelerometer derived density estimate is considered as the true density or actual observed density. The CC were calculated between these two atmospheric densities for a certain number of days, that were selected based on the availability of GRACE POE data and also based on previous analysis that had been performed for CHAMP from Reference 47. However, the POE derived densities for those days in Reference 47 were calculated using 3 hourly a_p step functions as input and not the other two types.

The RMS values are calculated for the same days and using the same function of a_p as input, as in Reference 47. In addition to that, the CC and RMS values are calculated for the same days using the other two functions of a_p input–a_p osculating spline functions and 3-hourly linear interpolated a_p functions.

3.1 3-Hourly Step Functions of a_p

The CC and RMS values between POE derived densities for the CHAMP and GRACE satellites with respect to the accelerometer derived densities were calculated. The POE derived densities were generated by using ODTK, where a_p was one of the inputs and it was considered to have a constant value for three hour intervals (3-hourly step functions). These CC values are the time averages of the zero delay CC values that were calculated for various dates that covered most of the solar and geomagnetic bins that were available for both CHAMP and GRACE. The dates for which they were calculated are given in Reference 47, and reproduced below under their respective solar and geomagnetic bins.

Table 3.1: Solar Activity Bins and Days [Ref. 47].

Activity Level Bins	Bin Definitions	Days in Bins	
Low	$F_{10.7}<75$	August 1-4, 2006	
		December 22-24, 2006	
Moderate	$75\leq F_{10.7}<150$	November 6-9, 2004	June 11-12, 2005
		January 16-21, 2005	June 22-23, 2005
		March 11-14, 2005	July 9-10, 2005
		March 17-18, 2005	August 23-24, 2005
		April 4, 2005	September 10-12, 2005
		May 7-13, 2005	September 14-15, 2005
		May 29-30, 2005	
Elevated	$150\leq F_{10.7}<190$	None	
High	$F_{10.7}\geq 190$	None	

Table 3.2: Geomagnetic Activity Bins and Days2 [Ref. 47].

Activity Level Bins	Bin Definitions	Days in Bins	
Quiet	$A_p \leq 10$	March 11-12, 2005 May 9, 2005 August 2-4, 2006	
Moderate	$10 < A_p < 50$	March 13-14, 2005 March 17-18, 2005 May 10-13, 2005 August 1, 2006 December 22-24, 2006	
Active	$A_p \leq 50$	November 6-9, 2004 January 16-21, 2005 April 4, 2005 May 7-8, 2005 May 29-30, 2005 June 11-12, 2005	June 22-23, 2005 July 9-10, 2005 August 23-24, 2005 September 10-12, 2005 September 14-15, 2005

The CC values from Reference 47 for these dates are shown in Table 3.3 and Table 3.4.

Table 3.3: Time averaged cross correlation coefficients for CHAMP POE density with accelerometer density [Ref. 47]. The highest value of cross correlation for each bin has been shaded.

Half Lives (min) BC/Density	CIRA 1972	Jacchia 1971	Jacchia-Roberts	MSISE 1990	NRLMSISE 2000
1.8/1.8	0.869	0.868	0.868	0.840	0.841
18/1.8	0.857	0.857	0.857	0.834	0.835
180/1.8	0.847	0.846	0.846	0.829	0.830
1.8/18	0.881	0.880	0.880	0.847	0.849
18/18	0.875	0.875	0.875	0.843	0.845
180/18	0.863	0.863	0.862	0.834	0.838
1.8/180	0.875	0.875	0.875	0.845	0.844
18/180	0.867	0.867	0.867	0.838	0.838
180/180	0.850	0.849	0.849	0.827	0.827

Table 3.4: Time averaged cross correlation coefficients for GRACE POE density with accelerometer density [Ref. 47].The highest value of cross correlation for each bin has been shaded.

Half Lives (min) BC/Density	CIRA 1972	Jacchia 1971	Jacchia-Roberts	MSISE 1990	NRLMSISE 2000
1.8/1.8	0.844	0.844	0.843	0.830	0.826
18/1.8	0.848	0.849	0.848	0.831	0.828
180/1.8	0.842	0.842	0.842	0.829	0.827
1.8/18	0.867	0.867	0.866	0.845	0.842
18-18	0.866	0.866	0.865	0.843	0.840
180/18	0.859	0.859	0.858	0.838	0.835
1.8/180	0.878	0.878	0.878	0.853	0.850
18/180	0.873	0.874	0.874	0.849	0.846
180/180	0.855	0.855	0.855	0.835	0.833

Table 3.3 and Table 3.4 show only the CC values of CHAMP and GRACE. Since the RMS values are also essential for comparison, they were calculated in this paper for the dates shown in Table 3.1 and Table 3.2, the results of which are displayed below.

Table 3.5: Time averaged RMS Values for CHAMP POE density with accelerometer density. The lowest value of RMS for each bin has been shaded.

Half Life (min) BC/Density	CIRA 1972	Jacchia 1971	Jacchia-Roberts	MSISE 1990	NRLMSISE 2000
1.8-1.8	0.730	0.726	0.727	1.031	1.030
18-1.8	0.843	0.830	0.834	1.041	1.043
180-1.8	0.973	0.967	0.970	1.087	1.086
1.8-18	0.672	0.677	0.675	1.046	1.038
18-18	0.707	0.700	0.702	1.043	1.038
180-18	0.845	0.826	0.832	1.128	1.123
1.8-180	0.675	0.683	0.680	1.034	1.039
18-180	0.711	0.707	0.708	1.053	1.059
180-180	0.867	0.834	0.843	1.249	1.247

Table 3.6: Time averaged RMS Values for GRACE POE density with accelerometer density. The lowest value of RMS for each bin has been shaded.

Half Life (min) BC/Density	CIRA 1972	Jacchia 1971	Jacchia-Roberts	MSISE 1990	NRLMSISE 2000
1.8-1.8	0.161	0.162	0.159	0.255	0.251
18-1.8	0.178	0.178	0.177	0.254	0.251
180-1.8	0.217	0.217	0.216	0.261	0.261
1.8-18	0.143	0.143	0.140	0.253	0.247
18-18	0.149	0.149	0.146	0.254	0.249
180-18	0.186	0.186	0.184	0.278	0.275
1.8-180	0.141	0.141	0.138	0.250	0.245
18-180	0.147	0.148	0.145	0.251	0.249
180-180	0.194	0.195	0.192	0.303	0.302

For all the tables displaying the CC and RMS for CHAMP and GRACE, the best value of CC (the maximum numerical value) and the best value of RMS (the minimum numerical value) under each baseline density model has been highlighted in yellow (or light gray) and the overall best value of CC and RMS (the best out of 45 cells of the table generated by all the various possible combinations of baseline density models and density and ballistic coefficient correlated half-lives) has been highlighted in light brown (or dark gray).

Please note that whenever a density model is mentioned, it's not the empirical model but rather the baseline density model used as an input to the ODTK to estimate the densities along the path of the satellite.

3.1.1 Observations for CHAMP

The CC values in Table 3.3 show that the best overall value of CC is for the baseline density model CIRA 1972 and the ballistic coefficient (BC) and density correlated half-life of 1.8-18, respectively. *Note: Henceforth, while specifying the ballistic coefficient and density*

correlated half-life combination, the first number indicates the BC correlated half-life in minutes while the second number, with a separating hyphen will be the density correlated half-life in minutes. The RMS values in Table 3.5 agree with this observation since the corresponding combination of half-lives is 1.8-18, for a baseline density model of CIRA 1972.

The CC table shows that all the baseline density models have a maximum CC at BC and density correlated half-life combination of 1.8-18. However, this is true in the RMS table only for the Jacchia family of density models, while the MSIS family of density models have an optimum BC and density half-life combination of 1.8-1.8.

3.1.2 Observations for GRACE

The CC values in Table 3.4 show that the best overall value of CC is for the baseline density model Jacchia 1971 with the BC and density correlated half-life combination of 1.8-180. However, the RMS values in Table 3.6 present a different view, in which the optimum baseline density model is Jacchia-Roberts while the BC/density correlated half-life combinations still remain the same with a value of 1.8-180.

Both the CC and RMS table reveal that the all the baseline density models have a maximum CC and minimum RMS value at BC and density correlated half-life combination of 1.8-180.

3.2 Linear Interpolated a_p Functions

Using linear interpolated a_p functions as one of the inputs, the densities and BC were estimated for various combinations of baseline atmospheric density models, and BC and density correlated half-lives, for both CHAMP and GRACE, for all the dates shown in Table 3.1 and Table 3.2. This option of using linear interpolated a_p function as the input is available in

ODTK. The zero delay cross correlation coefficient and RMS values for all these days were calculated between the POE derived densities and accelerometer derived densities. Then the time averages of these were tabulated and are displayed in Table 3.7, Table 3.8, Table 3.9, and Table 3.10.

3.2.1 Observations for CHAMP

Table 3.7: Time averaged zero delay cross correlation coefficients for CHAMP POE density with accelerometer density for linear interpolated ap functions as the input. The highest value of cross correlation for each bin has been shaded.

Half Life (min) BC/Density	CIRA 1972	Jacchia 1971	Jacchia-Roberts	MSISE 1990	NRLMSISE 2000
1.8-1.8	0.865	0.864	0.865	0.783	0.786
18-1.8	0.842	0.841	0.841	0.783	0.785
180-1.8	0.825	0.824	0.824	0.783	0.785
1.8-18	0.883	0.882	0.882	0.784	0.789
18-18	0.874	0.874	0.874	0.784	0.788
180-18	0.860	0.860	0.860	0.779	0.785
1.8-180	0.879	0.879	0.879	0.777	0.781
18-180	0.868	0.869	0.868	0.774	0.778
180-180	0.848	0.849	0.849	0.766	0.773

Table 3.8: Time averaged RMS Values for CHAMP POE density with accelerometer density for linear interpolated ap functions as the input. The lowest value of RMS for each bin has been shaded.

BC/Density	CIRA 1972	Jacchia 1971	Jacchia-Roberts	MSISE 1990	NRLMSISE 2000
1.8-1.8	0.749	0.751	0.754	1.361	1.359
18-1.8	0.898	0.890	0.895	1.318	1.318
180-1.8	1.060	1.057	1.060	1.323	1.320
1.8-18	0.670	0.689	0.688	1.418	1.410
18-18	0.711	0.716	0.718	1.386	1.378
180-18	0.857	0.844	0.851	1.442	1.432
1.8-180	0.668	0.690	0.688	1.422	1.425
18-180	0.709	0.716	0.718	1.413	1.414
180-180	0.868	0.844	0.854	1.589	1.574

The CC table shows that the best overall value of CC is for the baseline density model CIRA 1972 with a BC and density correlated half-life of 1.8-18. Even though the RMS table agrees partially with this observation in terms of the optimum baseline density model, the optimum combination of BC and density correlated half-life is 1.8-180. But, it can be seen that the RMS value under CIRA 1972 baseline model with a BC and density correlated half-life combination of 1.8-18 is very close to that of 1.8-180, and is in fact the second best RMS value among all combinations.

The CC table shows that all the baseline density models have a maximum CC at BC and density correlated half-life combination of 1.8-18. However, this is true in the RMS table only for the Jacchia family of density models (an exception being CIRA 1972), while the MSIS family of density models have an optimum BC and density correlated half-life combination of 18-1.8.

3.2.2 Observations for GRACE

Table 3.9: Time averaged zero delay cross correlation coefficients for GRACE POE density with accelerometer density for linear interpolated a_p functions as the input. The highest value of cross correlation for each bin has been shaded.

Half Life (min) BC/Density	CIRA 1972	Jacchia 1971	Jacchia-Roberts	MSISE 1990	NRLMSISE 2000
1.8-1.8	0.832	0.832	0.831	0.773	0.770
18-1.8	0.833	0.833	0.832	0.778	0.776
180-1.8	0.822	0.822	0.822	0.780	0.780
1.8-18	0.867	0.867	0.866	0.779	0.779
18-18	0.865	0.865	0.864	0.779	0.779
180-18	0.857	0.857	0.856	0.778	0.778
1.8-180	0.880	0.880	0.880	0.783	0.784
18-180	0.876	0.876	0.875	0.781	0.782
180-180	0.855	0.856	0.856	0.771	0.772

Table 3.10: Time averaged zero delay RMS Values for GRACE POE density with accelerometer density for linear interpolated ap functions as the input. The lowest value of RMS for each bin has been shaded.

Half Life (min) BC/Density	CIRA 1972	Jacchia 1971	Jacchia-Roberts	MSISE 1990	NRLMSISE 2000
1.8-1.8	0.164	0.167	0.164	0.331	0.329
18-1.8	0.186	0.187	0.186	0.325	0.323
180-1.8	0.234	0.234	0.233	0.326	0.326
1.8-18	0.139	0.143	0.140	0.339	0.336
18-18	0.146	0.148	0.146	0.337	0.334
180-18	0.183	0.185	0.183	0.359	0.356
1.8-180	0.137	0.140	0.137	0.339	0.337
18-180	0.143	0.146	0.143	0.341	0.338
180-180	0.188	0.191	0.188	0.395	0.391

The CC table shows that the best overall value of CC is for the baseline density model Jacchia 1971 and with BC and density correlated half-life combination of 1.8-180. However, the RMS table presents a different view, in which the optimum baseline density model is CIRA 1972 while the BC and density correlated of half-life combinations still remain the same.

While the CC table shows that all the baseline density models have the best value of CC (maximum numerical value) at a BC and density correlated half-life combination of 1.8-180, the RMS table partially agrees with this observation, with the exception being the MSIS family baseline density models. The latter have an optimum BC and density correlated half-life combination of 18-1.8.

In general, the Jacchia based density models used as baselines prove to be superior to the MSIS family baseline models both in terms of their cross correlation coefficient and root mean square sense. Also, the CC and RMS values among the Jacchia family baseline density models are very close to each other for any given BC and density correlated half-life combination, as expected. This holds true for the MSIS family baseline density models as well. However, the difference between these two families of baseline density models is significant.

3.3 a_p Osculating Spline Functions

Using a_p osculating spline functions as inputs the densities and BC were estimated for various combination of baseline atmospheric density models, and BC and density correlated half-lives, for both CHAMP and GRACE, for all the dates shown in Table 3.1 and Table 3.2. This option of using cubic spline a_p functions as an input is available in ODTK. The zero delay cross correlation coefficient and RMS values for all these days were calculated between the

POE derived densities and accelerometer derived densities. Then the time averages of these were tabulated and are displayed in Table 3.11, Table 3.12, Table 3.13, and Table 3.14.

3.3.1 Observations for CHAMP

Table 3.11: Time averaged zero delay cross correlation coefficients for CHAMP POE density with accelerometer density for ap osculating spline functions as the input. The highest value of cross correlation for each bin has been shaded.

Half Life (min) BC/Density	CIRA 1972	Jacchia 1971	Jacchia-Roberts	MSISE 1990	NRLMSISE 2000
1.8-1.8	0.877	0.875	0.876	0.828	0.831
18-1.8	0.867	0.866	0.866	0.830	0.833
180-1.8	0.856	0.855	0.855	0.830	0.833
1.8-18	0.886	0.885	0.885	0.827	0.833
18-18	0.881	0.880	0.880	0.827	0.833
180-18	0.868	0.868	0.868	0.822	0.828
1.8-180	0.882	0.882	0.882	0.821	0.826
18-180	0.874	0.875	0.874	0.819	0.823
180-180	0.856	0.856	0.856	0.811	0.815

Table 3.12: Time averaged zero delay RMS Values for CHAMP POE density with accelerometer density for ap osculating spline functions as the input. The lowest value of RMS for each bin has been shaded.

BC/Density	CIRA 1972	Jacchia 1971	Jacchia-Roberts	MSISE 1990	NRLMSISE 2000
1.8-1.8	0.714	0.722	0.723	1.133	1.123
18-1.8	0.825	0.818	0.822	1.099	1.092
180-1.8	0.958	0.953	0.956	1.113	1.105
1.8-18	0.661	0.681	0.680	1.182	1.165
18-18	0.696	0.700	0.703	1.157	1.140
180-18	0.838	0.823	0.830	1.220	1.202
1.8-180	0.661	0.684	0.682	1.185	1.178
18-180	0.695	0.704	0.705	1.182	1.175
180-180	0.856	0.830	0.840	1.354	1.340

The CC table shows that the best overall value of CC is for the baseline density model CIRA 1972 with a BC and density correlated half-life of 1.8-18. Even though the RMS table agrees partially with this observation in terms of the optimum baseline density model, the optimum combination of BC and density correlated half-life is 1.8-180. But the RMS value under CIRA 1972 baseline model with a BC and density correlated half-life combination of 1.8-18 is very close to that of 1.8-180, and is in fact the second best value among all 45 combinations.

The CC table shows that Jacchia based density models have a maximum CC at BC and density correlated half-life combination of 1.8-18, while the MSIS based family of density models have a half-life combination of 18-1.8 and 180-1.8 for MSISE 1990 and NRLMSISE 2000, respectively. Similar observations are made in the RMS table for the Jacchia family of density models (an exception being CIRA 1972), while both the MSIS family density models have an optimum BC and density correlated half-life combination of 18-1.8.

3.3.2 Observations for GRACE

Table 3.13: Time averaged zero delay cross correlation coefficients for GRACE POE density with accelerometer density for ap osculating spline functions as the input. The highest value of cross correlation for each bin has been shaded.

Half Life (min) BC/Density	CIRA 1972	Jacchia 1971	Jacchia-Roberts	MSISE 1990	NRLMSISE 2000
1.8-1.8	0.851	0.850	0.849	0.823	0.821
18-1.8	0.858	0.858	0.857	0.829	0.828
180-1.8	0.854	0.854	0.854	0.832	0.832
1.8-18	0.873	0.873	0.872	0.828	0.827
18-18	0.872	0.872	0.871	0.828	0.827
180-18	0.866	0.866	0.865	0.827	0.827
1.8-180	0.885	0.885	0.885	0.832	0.833
18-180	0.882	0.882	0.882	0.830	0.831
180-180	0.863	0.864	0.863	0.821	0.821

Table 3.14: Time averaged zero delay RMS Values for GRACE POE density with accelerometer density for ap osculating spline functions as the input. The lowest value of RMS for each bin has been shaded.

Half Life (min) BC/Density	CIRA 1972	Jacchia 1971	Jacchia-Roberts	MSISE 1990	NRLMSISE 2000
1.8-1.8	0.154	0.157	0.155	0.274	0.270
18-1.8	0.172	0.174	0.172	0.268	0.265
180-1.8	0.212	0.213	0.212	0.271	0.269
1.8-18	0.136	0.139	0.136	0.279	0.274
18-18	0.142	0.145	0.142	0.278	0.274
180-18	0.181	0.183	0.180	0.300	0.296
1.8-180	0.134	0.137	0.134	0.278	0.274
18-180	0.140	0.143	0.140	0.281	0.276
180-180	0.188	0.191	0.188	0.332	0.327

Both the CC table and RMS tables show that the best overall value of CC is for the baseline density model CIRA 1972 with the BC and density correlated half-life combination of 1.8-180.

The CC and RMS tables show that the Jacchia family baseline density models have the best value of CC (maximum value) at BC and density correlated half-life combination of 1.8-180. While MSIS family based baseline density models have an optimum combination of BC and density correlated half-life of 18-1.8 for the RMS table, and 180-1.8 and 1.8-180 for the MSISE and NRLMSISE-2000 density models, respectively, for the CC table.

In general, the Jacchia based density models used as baselines prove to be superior to the MSIS family baseline models both in terms of their cross correlation coefficient and root mean square sense. Also, the CC and RMS values among the Jacchia family baseline density models are very close to each other for any given BC and density correlated half-life combination, as expected. This holds true for the MSIS family of baseline density models as well. However, the difference between these two families of baseline density models is significant.

3.4 General Observations for All Three Different Cases

The following are the observations based on examining the three different functions of a_p as an input to ODTK to generate the POE densities.

3.4.1 CHAMP

A comparison of the best value of CC from each of the tables for different a_p functions reveal that using a_p spline function as input has the best value of CC and RMS. The best value of CC and RMS for each type of a_p function for CHAMP is tabulated below.

Table 3.15: The best time averaged zero delay cross correlation and RMS Values for CHAMP POE density with accelerometer density for each different function of a_p as the input. The highest cross correlation and the lowest value of RMS for each bin have been shaded.

Kind of a_p function	3-hourly step function of a_p	Linear interpolated a_p function	a_p osculating spline function
CC	0.881	0.883	0.886
RMS	0.672	0.668	0.661

This best value of CC corresponds to the baseline density model, CIRA 1972, with BC and density correlated half-life combination of 1.8-18. The next best case of a_p functions is the one with the second best value of CC among the other two functions of a_p as the input, and the data indicate that it is the one using the linear interpolated a_p functions. This is followed by 3-hourly a_p step functions. Both of them have the best value of CC for a baseline density model, CIRA 1972, with BC and density correlated half-life combination of 1.8-18.

A similar observation for RMS shows that using a_p spline functions as the input yields the best value of RMS and this corresponds to the baseline density model, CIRA 1972, with BC and density correlated half-life combination of 1.8-180; different from observations from the CC tables. However, it is also evident from the RMS table for a_p cubic spline input (Table 3.12), that the next best value of RMS is for a BC and density correlated half-life combination of 1.8-18. And the difference between these two values is on the order of 0.0001 (not observable in Table 3.12 since the table is rounded off to three decimal places). The next best case is linear interpolated a_p functions, followed by 3-hourly step functions of a_p. While all three cases have CIRA 1972 as their optimum baseline density model, the 3-hourly step functions of a_p has its BC and density correlated half-life combination of 1.8-18, while linear interpolated a_p functions and spline functions of ap differ in this respect and have a

corresponding value of 1.8-180. But a combination of 1.8-18, is not only very close to the RMS value of the former, but also the second best among all the remaining combination of baseline density models and half-lives. Thus, for linear interpolated a_p functions and cubic spline a_p functions, the optimum value of RMS under a baseline density model of CIRA 1972 (and overall) has a BC and density correlated half-life combination of 1.8-18.

While CC values for the Jacchia family baseline density models show improvement (increase in the numerical value of CC) from 3-hourly a_p step functions to interpolated a_p functions to a_p cubic spline functions, no such improvement is visible for the MSIS family baseline density models. In fact, the CC values deteriorate from a_p step functions to cubic spline to linear interpolated inputs. The worst values being that for linear interpolated a_p functions.

3.5 GRACE

A comparison of the best value of CC for each of the tables for different a_p functions reveals that using a_p spline functions as input has the best value of CC and it corresponds to the baseline density model, CIRA 1972, with a BC and density correlated half-life combination of 1.8-180. The best value of CC and RMS for each type of a_p function for GRACE is tabulated in Table 3.16.

Table 3.16: The best time averaged zero delay cross correlation and RMS Values for CHAMP POE density with accelerometer density for each different function of a_p as the input. The highest cross correlation and the lowest value of RMS for each bin have been shaded.

Kind of a_p function	3-hourly step function of a_p	Linear interpolated a_p function	a_p osculating spline function
CC	0.878	0.880	0.885
RMS	0.138	0.137	0.134

The next best case of a_p functions is the one with the second best value of CC among the other two a_p functions as the input, and the data indicate that it is the one using the linear interpolated a_p functions. This is followed by 3-hourly a_p step functions. Both of them have the best value of CC for a baseline density model of Jacchia 1971 and with BC and density correlated half-life combination of 1.8-180.

A similar observation for RMS shows that using a_p spline functions as the input has the best value of RMS and this corresponds to the baseline density model CIRA 1972, with a BC and density correlated half-life combination of 1.8-180; the same as the observations from the CC tables. The next best case is linear interpolated a_p functions, followed by 3-hourly step functions of a_p. While linear interpolated a_p and cubic spline a_p functions have CIRA 1972 as their optimum baseline density model, 3-hourly a_p step function has its optimum baseline density model as Jacchia-Roberts. But all three share the same combination of BC and density correlated half-life of 1.8-180.

While CC values for the Jacchia family baseline density models show improvement (increase in the numerical value of CC) from 3-hourly a_p step functions to interpolated a_p functions to a_p cubic spline functions, no such improvement is visible for the MSIS family of baseline density models. In fact, the CC values deteriorate from a_p step functions to cubic spline to linear interpolated inputs. The worst values being for linear interpolated a_p functions.

4 LINEAR WEIGHTED BLENDING TECHNIQUE TO CREATE CONTINUOUS DATA SETS

The results are displayed for each solar and geomagnetic activity bin by calculating the cross correlation coefficient between the type of density estimate and the accelerometer derived density. This is done for both CHAMP and GRACE.

4.1 Cross Correlation Results

The cross correlation was calculated between density estimates obtained from all three methods - the POE derived density, POE derived density with linear weighted blending for the overlap periods, and using linear weighted blending of the position vectors of POE as measurements in ODTK to estimate densities–and the accelerometer derived densities for all the days in Table 2.2 and Table 2.3. The cross correlation between the HASDM densities and accelerometer derived densities was also calculated. The average cross correlation for each solar and geomagnetic bin was calculated and is displayed in Table 4.1, along with the average CC for all the bins.

Table 4.1: Cross correlation coefficient for different types of CHAMP POE derived density and HASDM with accelerometer derived density. The highest value of cross correlation for each bin has been shaded.

Bin	Cross Correlation			
	HASDM	**POE derived density**	**POE derived density with linear weighted blending technique**	**POE derived density using linear weighted blending of POE as measurements**
Low Solar	0.884	0.892	0.896	0.894
Moderate Solar	0.920	0.922	0.927	0.926
Elevated Solar	0.932	0.945	0.946	0.945
High Solar	0.880	0.892	0.901	0.898
Quiet Geomagnetic	0.935	0.935	0.939	0.938
Moderate Geomagnetic	0.876	0.891	0.897	0.895
Active Geomagnetic	0.851	0.855	0.866	0.865
For all Bins	0.910	0.916	0.921	0.919

In Table 4.1, the highest correlation with accelerometer derived density for all the solar and geomagnetic level bins is for the POE derived density found using the linear weighted blending technique in the density overlap regions. The second highest is for the case of POE derived densities using linear weighted blending of POE as measurements in ODTK, for all the solar and geomagnetic bins, except for the elevated solar activity bin. However, the difference between the two is less than one thousandth and hence negligible. The next best estimate is the POE derived density without making any changes to either the density data or the POE data used as measurements in ODTK.

The exact same procedure was performed for GRACE for all the days in Table 2.4. The average cross correlation for each solar and geomagnetic bin was calculated and is displayed in Table 4.2, along with the average CC for all the bins.

Table 4.2. Cross correlation coefficient for different types of GRACE POE derived density and HASDM with accelerometer derived density. The highest value of cross correlation for each bin has been shaded.

Bin	Cross Correlation			
	HASDM	POE derived density	POE derived density with linear weighted blending technique	POE derived density using linear weighted blending of POE as measurements
Low Solar	0.636	0.707	0.726	0.702
Moderate Solar	0.894	0.900	0.901	0.900
Quiet Geomagnetic	0.805	0.834	0.842	0.831
Moderate Geomagnetic	0.884	0.888	0.891	0.889
Active Geomagnetic	0.774	0.823	0.825	0.822
For all Bins	0.829	0.852	0.857	0.851

The results displayed in Table 4.2 for GRACE are consistent with those of CHAMP, both the satellites show that the highest correlation with accelerometer derived density for all the bins is for the POE derived density using the linear weighted blending technique in the density overlap regions. The second highest is for the case of POE derived densities using linear weighted blending of POE as measurements in ODTK, for the moderate solar and geomagnetic bins, and the POE derived density without making any changes to either the density data or the POE data used as measurements in ODTK for the remaining bins.

4.2 Results for One Week

The method used above can be used for any length of time desired by using a series of consecutive solution fit spans that cover the time period of interest. One such study was performed for this research with a time period of one week. The week selected was from 26 October 2003 to 1 November 2003 because this week had the highest solar and geomagnetic activity during the CHAMP mission life. To obtain a continuous POE derived density for the

whole week fifteen successive 14 hour solution fit spans were used. The linear weighted blending was produced for all the periods of overlap throughout the week, one for density and the other for POE so that it can be used as measurements in ODTK to estimate the density. The cross correlation between the accelerometer density and the four other types of density described above were calculated for the same time period. The results of the cross correlation are displayed below.

Table 4.3. Cross correlation coefficient for different types of CHAMP POE derived density and HASDM with Accelerometer derived density for time period of one week, from October 26 to November 1, 2003. The highest value of cross correlation has been shaded.

Cross Correlation of accelerometer derived density with	Cross Correlation
HASDM	0.927
POE derived density	0.916
POE derived density with linear weighted blending technique	0.944
POE derived density using linear weighted blending of POE as measurements	0.943

Table 4.3 shows that the highest value of CC is for the case of POE derived density by using the linear weighted blending technique in all the overlap regions and the next highest being the POE derived densities using linear weighted blending of POE as measurements in ODTK. The difference between the two is only one thousandth. Figure 4.1 shows the plot for one full week for accelerometer derived density, HASDM, and POE derived density with weighted blending.

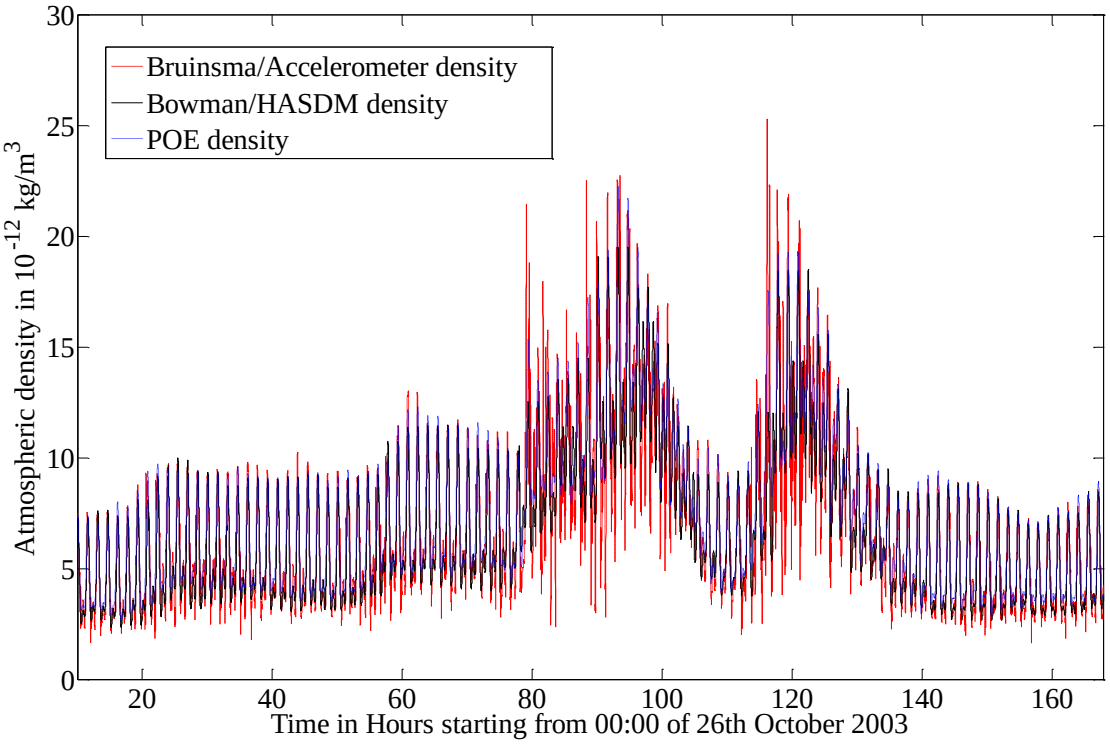

Figure 4.1. Accelerometer derived densities, precision orbit density estimates with linear weighted blending, and HASDM density, for a period of one week, from October 26 to November 1, 2003.

4.3 One Week Continuous Sets

To create continuous data sets for the entire mission life of CHAMP and GRACE, the linear weighted blending technique was applied to POE derived density estimates for a period of one week. This week spanned from midnight of any given Sunday till midnight of the next Sunday, thus utilizing fifteen scenarios each with 14 hour solution fit span. The cross correlation between the one week data sets and the accelerometer derived density, as well as between HASDM and accelerometer derived density was calculated for all the weeks for the entire mission life of CHAMP and GRACE, whenever data was available. Data for all three types of density was available for CHAMP from the end of May 2001 till December 2008. For GRACE, they were available from January 2005 to December 2008. There were a few days of

data missing in between these time spans. For most of the cases, the cross correlation was higher for the former case.

The average cross correlation of all the weeks calculated for CHAMP are shown in Table 4.4, displayed under its respective solar and geomagnetic bin, along with the average CC for all the bins.

Table 4.4. Cross correlation coefficient for POE derived density with linear weighted blending technique and HASDM with accelerometer derived density, for a period of one week, for CHAMP. The highest value of cross correlation for each bin has been shaded.

Bin	Cross Correlation	
	HASDM	POE derived density with linear weighted blending technique
Low Solar	0.909±0.052	0.926±0.041
Moderate Solar	0.924±0.053	0.935±0.046
Elevated Solar	0.913±0.143	0.919±0.145
High Solar	0.938±0.034	0.948±0.029
Quiet Geomagnetic	0.918±0.078	0.932±0.073
Moderate Geomagnetic	0.923±0.048	0.932±0.046
Active Geomagnetic	0.942±0.013	0.950±0.007
For all Bins	0.920±0.067	0.932±0.062

In Table 4.4, the highest correlation with accelerometer derived density for all the solar and geomagnetic level bins is for the POE derived density found using the linear weighted blending technique in the density overlap regions.

Similarly, the average cross correlation of all the weeks calculated for GRACE are shown in Table 4.5, displayed under its respective solar and geomagnetic bin, along with the average CC for all the bins.

Table 4.5. Cross correlation coefficient for POE derived density with linear weighted blending technique and HASDM with accelerometer derived density, for a period of one week, for GRACE. The highest value of cross correlation for each bin has been shaded.

Bin	Cross Correlation	
	HASDM	POE derived density with linear weighted blending technique
Low Solar	0.806±0.154	0.829±0.144
Moderate Solar	0.881±0.102	0.897±0.103
Quiet Geomagnetic	0.832±0.147	0.853±0.141
Moderate Geomagnetic	0.878±0.090	0.892±0.087
For all Bins	0.845±0.135	0.864±0.129

In Table 4.5, the highest correlation with accelerometer derived density for all the solar and geomagnetic level bins is for the POE derived density found using the linear weighted blending technique in the density overlap regions. This observation is consistent with that observed for the CHAMP satellite.

4.4 Removing 'Bad' Weeks

Further investigation of the accelerometer derived density for weeks having very low cross correlation (below 0.6, including negative CC) revealed anomalous values of accelerometer densities. While some of them were negative, others had spikes at certain time periods. These spikes were an order of magnitude higher than the density values for the rest of the time periods. For CHAMP, four such weeks were found. While three of them had negative accelerometer derived density value, one of them had spikes for a considerable period of time (about 8-10 hours). For GRACE, eight such weeks were identified. All eight weeks had spike(s) in accelerometer derived density. When the data around the spike was removed and the cross correlation recalculated, an improvement in the cross correlation was observed. These

anomalous weeks for both CHAMP and GRACE as well as the cross correlation for each of these weeks are given in the tables below.

Table 4.6. List of weeks where the accelerometer derived density had negative values and/or spikes, for CHAMP. The cross correlation for that week is also shown for reference.

Week	Cross Correlation	
	HASDM	POE derived density with linear weighted blending technique
10th to 16th June, 2001	0.528	0.528
7th to 13th October, 2001	0.614	-0.025
9th to 15th September, 2002	-0.014	0.139
8th to 14th December, 2002	0.187	0.165

Table 4.7. List of weeks where the accelerometer derived density had negative values and/or spikes, for GRACE. The cross correlation for that week is also shown for reference.

Week	Cross Correlation	
	HASDM	POE derived density with linear weighted blending technique
14th to 20th May, 2006	0.343	0.397
11th to 17th June, 2006	0.480	0.491
13th to 19th August, 2006	0.534	0.523
25th February to 3rd March, 2007	0.420	0.411
4th to 10th March, 2007	0.361	0.371
8th to 14th July, 2007	0.525	0.531
7th to 13th October, 2007	0.342	0.348

To illustrate the abnormality in the accelerometer derived density, the plots of densities for the four weeks for CHAMP are shown in the figures below.

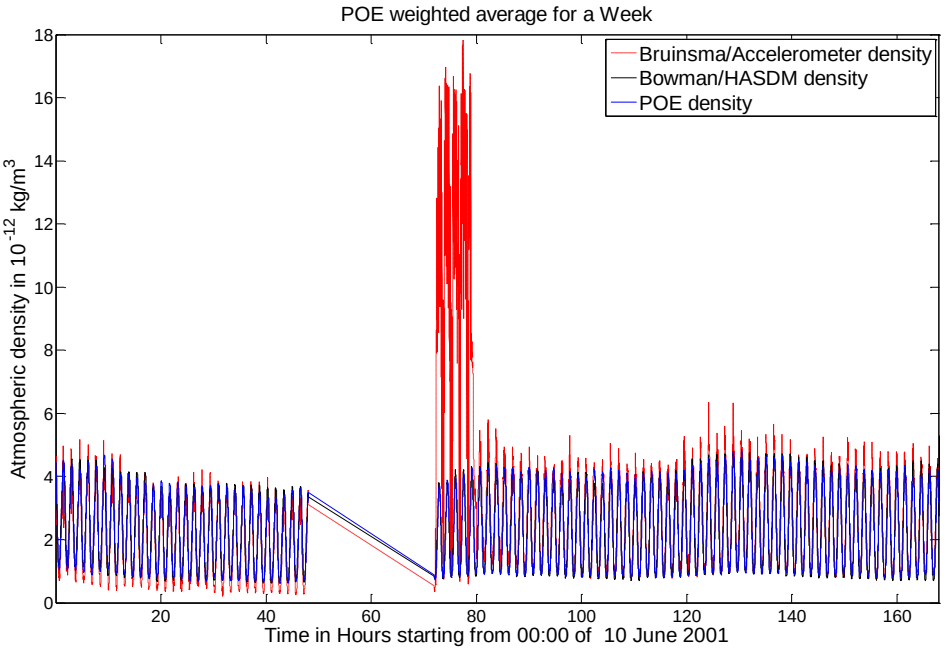

Figure 4.2. Accelerometer derived densities, precision orbit density estimates with linear weighted blending, and HASDM density, for a period of one week, from June 10 to 16, 2001.

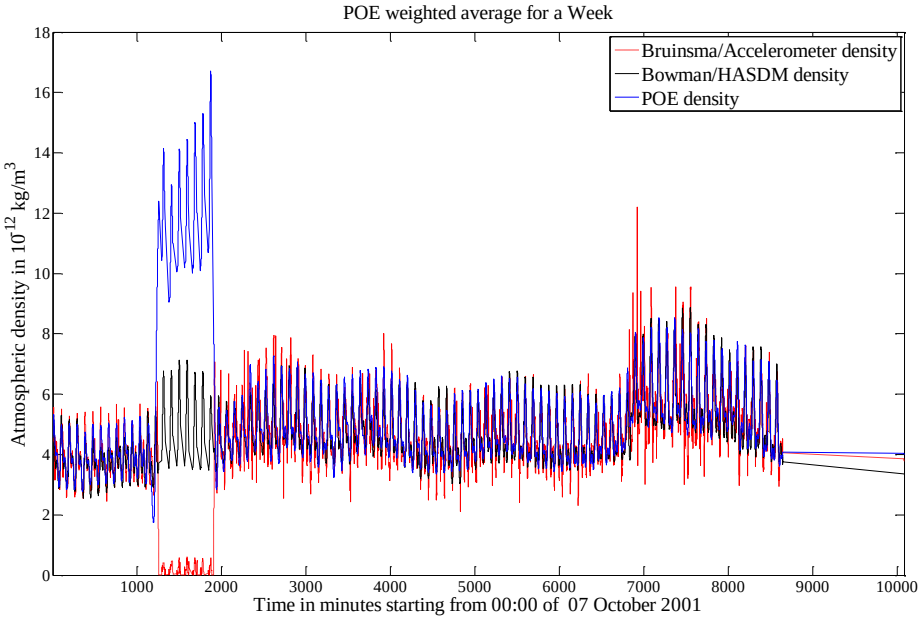

Figure 4.3. Accelerometer derived densities, precision orbit density estimates with linear weighted blending, and HASDM density, for a period of one week, from October 7 to 13, 2001.

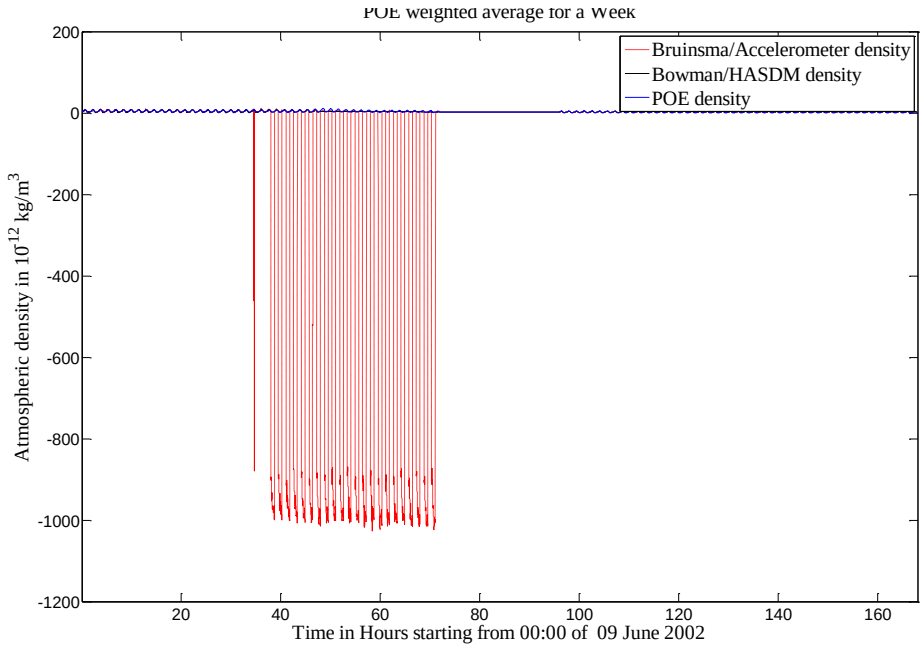

Figure 4.4. Accelerometer derived densities, precision orbit density estimates with linear weighted blending, and HASDM density, for a period of one week, from June 9 to 15, 2002.

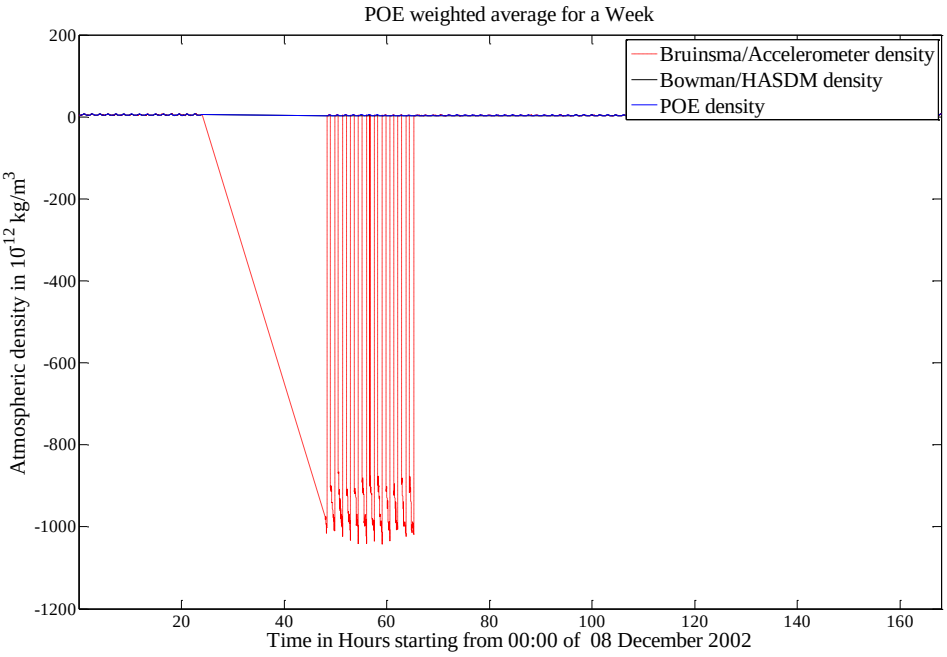

Figure 4.5. Accelerometer derived densities, precision orbit density estimates with linear weighted blending, and HASDM density, for a period of one week, from December 8 to 14, 2002.

All the figures above show anomalies in the accelerometer derived density (such as being negative, which is physically meaningless).

Similarly, plots for some of the selected weeks for GRACE are shown in the figures below. Only a few weeks are shown because the nature of the anomaly (one or more spikes in the accelerometer derived density) is common to all.

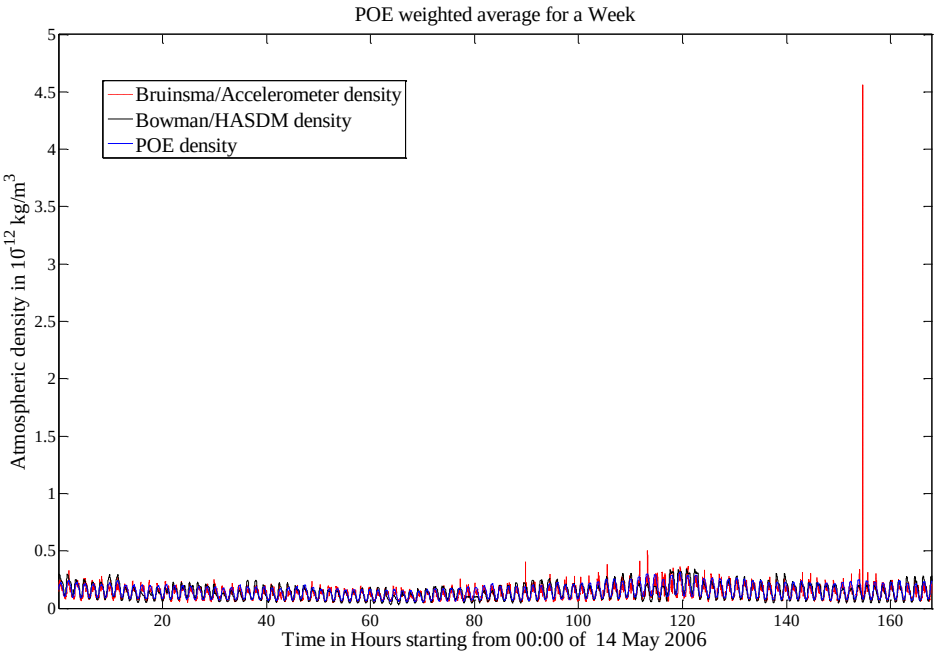

Figure 4.6. Accelerometer derived densities, precision orbit density estimates with linear weighted blending, and HASDM density, for a period of one week, from May 14 to 20, 2006.

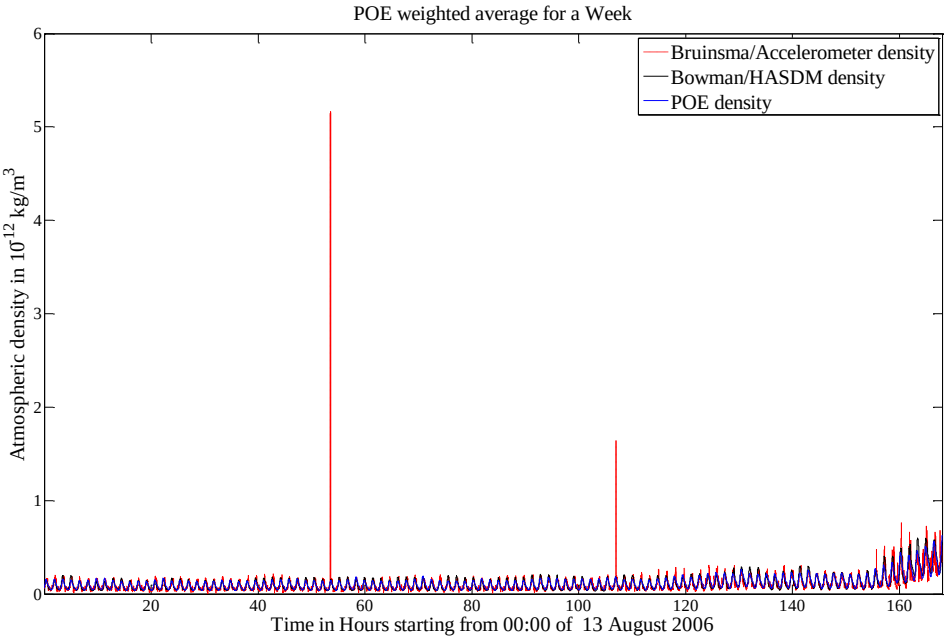

Figure 4.7. Accelerometer derived densities, precision orbit density estimates with linear weighted blending, and HASDM density, for a period of one week, from August 13 to 19, 2006.

After these spike were removed, the cross correlation was recalculated, and the improved results are compared with the previous results and are shown in Table 4.8.

Table 4.8. List of weeks where the accelerometer derived density had spikes for GRACE. The cross correlation for that week is also shown before and after eliminating the spikes.

Week	Cross Correlation			
	HASDM (Before)	HASDM (After)	POE derived density with linear weighted blending technique (Before)	POE derived density with linear weighted blending technique (After)
14th to 20th May, 2006	0.343	0.793	0.397	0.894
11th to 17th June, 2006	0.480	0.943	0.491	0.958
13th to 19th August, 2006	0.534	0.898	0.523	0.878
25th February to 3rd March, 2007	0.420	0.818	0.411	0.825
4th to 10th March, 2007	0.361	0.803	0.371	0.827
8th to 14th July, 2007	0.525	0.903	0.531	0.899
7th to 13th October, 2007	0.342	0.884	0.348	0.905

A large improvement in the cross correlation values for all the weeks is observed (except for the week starting on 29th July, where the improvement is relatively small). Cases with spikes whose order of magnitude was the same as the density values for the rest of the time periods, were not considered as possible candidates for poor accelerometer density values. To illustrate this, consider the week of 29th July 2007, whose CC between POE derived density and accelerometer density is 0.645 and for HASDM density is 0.596 (very close to 0.6). The density plot is shown in the figure below.

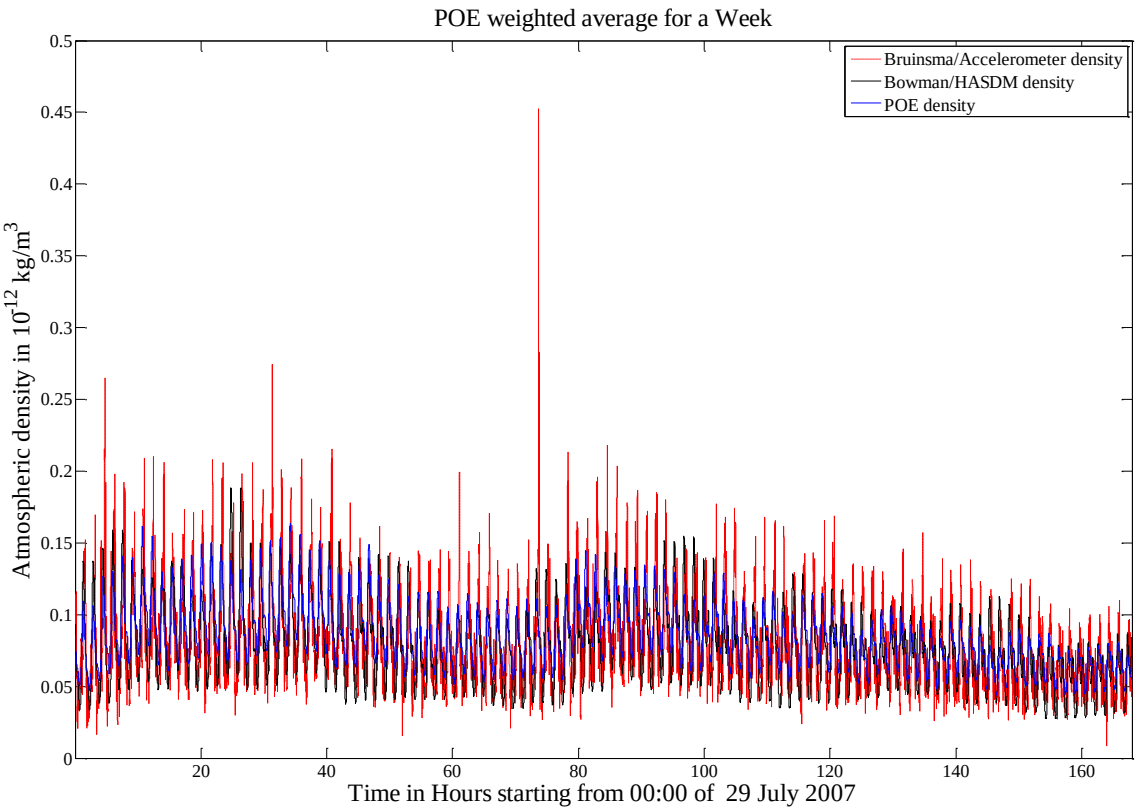

Figure 4.8: Accelerometer derived densities, precision orbit density estimates with linear weighted blending, and HASDM density, for a period of one week, from July 29 to August 4, 2007.

The spike in density at about 73 hours is on the same order of magnitude as normal density variations. After removing the spike, the CC was calculated, and the results before and after removal of the spike is shown in the table below.

Table 4.9: Cross correlation before and after removal of a certain spike in accelerometer derived density, for the week July 29 to August 4, 2007, for GRACE.

Week	Cross Correlation			
	HASDM (Before)	**HASDM (After)**	**POE derived density with linear weighted blending technique (Before)**	**POE derived density with linear weighted blending technique (After)**
29th July to 4th August, 2007	0.596	0.603	0.645	0.654

As seen in Table 4.9, the improvement in CC is less than two percent. As mentioned earlier, since the spike is on the same order as the normal density variations, removing this spike would not yield a significant improvement in CC. Also since they are on the same order of magnitude, the accelerometer density can't be labeled as incorrect or not reliable for this particular week. However, a satisfactory explanation for the reason behind a poor correlation (less than HASDM) for this week is hard to provide. The best explanation perhaps would be that low magnitude spikes are present throughout the week, which would contribute to low CC.

For GRACE, other weeks with cross correlation values less than 0.6 (but positive) were observed; however the reason for such a low CC can't be explained satisfactorily. Neither an appreciable spike was observed nor did negative accelerometer density exist during the week, thus the same explanation used to explain the low CC for the earlier weeks could not be used for the new ones. Like the week of July 29 to August 4, 2007, the best explanation would be that the presence of low magnitude spikes throughout the time span of one week results in low CC. The weeks for which the reason for low CC is unknown or does not have any satisfactory explanation are displayed in Table 4.10 along with their CC.

Table 4.10. List of weeks where the accelerometer derived density had negative values and/or spikes, for GRACE. The cross correlation for that week is also shown for reference.

Week	Cross Correlation	
	HASDM	POE derived density with linear weighted blending technique
23rd to 29th December, 2007	0.466	0.499
13th to 19th January, 2008	0.454	0.475
20th to 26th January, 2008	0.386	0.574
7th to 13th December, 2008	0.553	0.536

After all the 'bad' weeks were omitted from the list of weeks for which the data exists for the entire mission life of CHAMP and GRACE, the average CC for the entire mission life of CHAMP and GRACE was recalculated. Please note that the weeks for which the reason for low CC was unknown were not omitted, this is because unless there is a justifiable explanation that the accelerometer density is unreliable for these weeks, these are considered as poor correlation results and nothing more. These results are displayed in Table 4.11 and Table 4.12.

Table 4.11. Cross correlation coefficient for POE derived density with linear weighted blending technique and HASDM with accelerometer derived density, for a period of one week, for CHAMP. The results shown are before and after elimination of 'bad' weeks. The highest value of cross correlation compared between the results obtained before and after removing 'bad' weeks, under the same type of densities used has been shaded for each bin (except when they are equal).

Bin	Cross Correlation			
	HASDM (Before)	HASDM (After)	POE derived density with linear weighted blending technique (Before)	POE derived density with linear weighted blending technique (After)
Low Solar	0.909±0.052	0.909±0.052	0.926±0.041	0.926±0.041
Moderate Solar	0.924±0.053	0.924±0.053	0.935±0.046	0.935±0.046
Elevated Solar	0.913±0.143	0.944±0.048	0.919±0.145	0.949±0.041
High Solar	0.938±0.034	0.938±0.034	0.948±0.029	0.948±0.029
Quiet Geomagnetic	0.918±0.078	0.923±0.055	0.932±0.073	0.937±0.043
Moderate Geomagnetic	0.923±0.048	0.923±0.048	0.932±0.046	0.932±0.046
Active Geomagnetic	0.942±0.013	0.942±0.013	0.950±0.007	0.950±0.007
For all Bins	0.920±0.067	0.923±0.052	0.932±0.062	0.935±0.044

Table 4.12. Cross correlation coefficient for POE derived density with linear weighted blending technique and HASDM with accelerometer derived density, for a period of one week, for GRACE. The results shown are before and after elimination of 'bad' weeks. The highest value of cross correlation compared between the results obtained before and after removing 'bad' weeks, under the same type of densities used has been shaded for each bin (except when they are equal).

Bin	Cross Correlation			
	HASDM (Before)	HASDM (After)	POE derived density with linear weighted blending technique (Before)	POE derived density with linear weighted blending technique (After)
Low Solar	0.806±0.154	0.820±0.133	0.829±0.144	0.843±0.121
Moderate Solar	0.881±0.102	0.896±0.068	0.897±0.103	0.913±0.064
Quiet Geomagnetic	0.832±0.147	0.852±0.188	0.853±0.141	0.874±0.107
Moderate Geomagnetic	0.878±0.090	0.878±0.090	0.892±0.087	0.892±0.087
For all Bins	0.845±0.135	0.859±0.111	0.864±0.129	0.879±0.102

As expected, there is an improvement in the CC because the 'bad' weeks were omitted and thus the accelerometer density, against which the HASDM density and POE derived density were compared, improved.

4.5 Anomalous Behavior of CHAMP and GRACE

While developing precision orbit ephemeris (POE) derived density for CHAMP and GRACE, Fattig [Ref. 48] discovered time periods of low CC of the the accelerometer derived density with the POE derived density and HASDM density. These time periods were especially from October 2005 to January 2006 for the GRACE. The low CC was observed for the GRACE satellites only (both GRACE-A and GRACE-B) during this time period and not for CHAMP, except in early 2006 and the low CC for CHAMP was relatively better than GRACE. A plot showing the CC for both CHAMP and GRACE around this time period is given in Ref. 48 and reproduced in Figure 4.9.

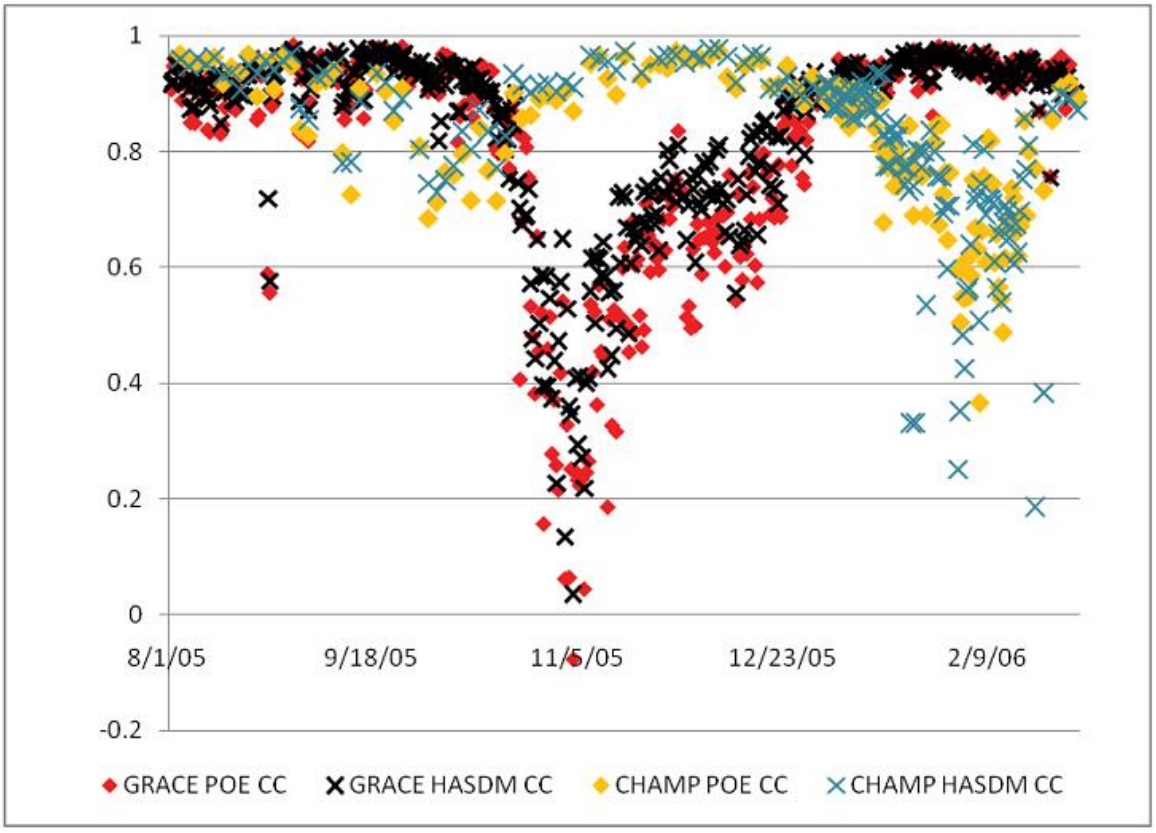

Figure 4.9: Cross correlation between accelerometer derived density and POE derived density for CHAMP and GRACE-A from August 1, 2005 to February 28, 2006 [Ref. 48**].**

Reference 49 attempts to explain this behavior by examining the relation between density and inclination of the orbit plane with respect to the direction of the Sun. Figure 4.10 shows both the accelerometer derived density and POE derived density for the period between October 2005 to January 2006 for GRACE-A. The POE derived density plotted in Figure 4.10 is the POE derived density generated for one week by using the linear weighted blending technique, described earlier in this section. The density variations have a relatively low magnitude from late October to December 2005. This time period corresponds to low CC for GRACE.

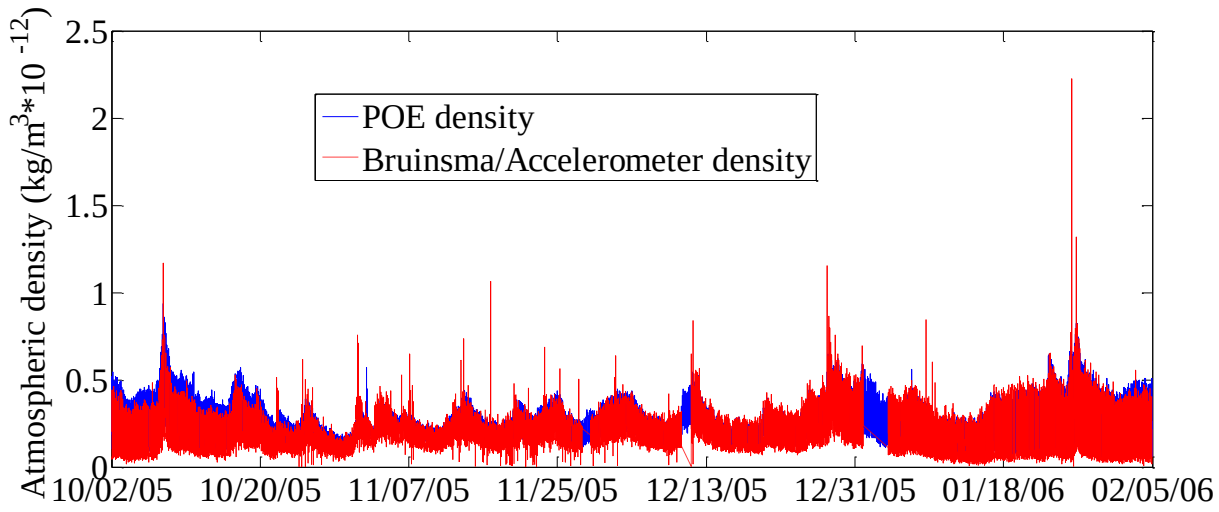

Figure 4.10: POE derived density and accelerometer derived density for GRACE-A from October 2005 to January 2006 [Ref. 49**].**

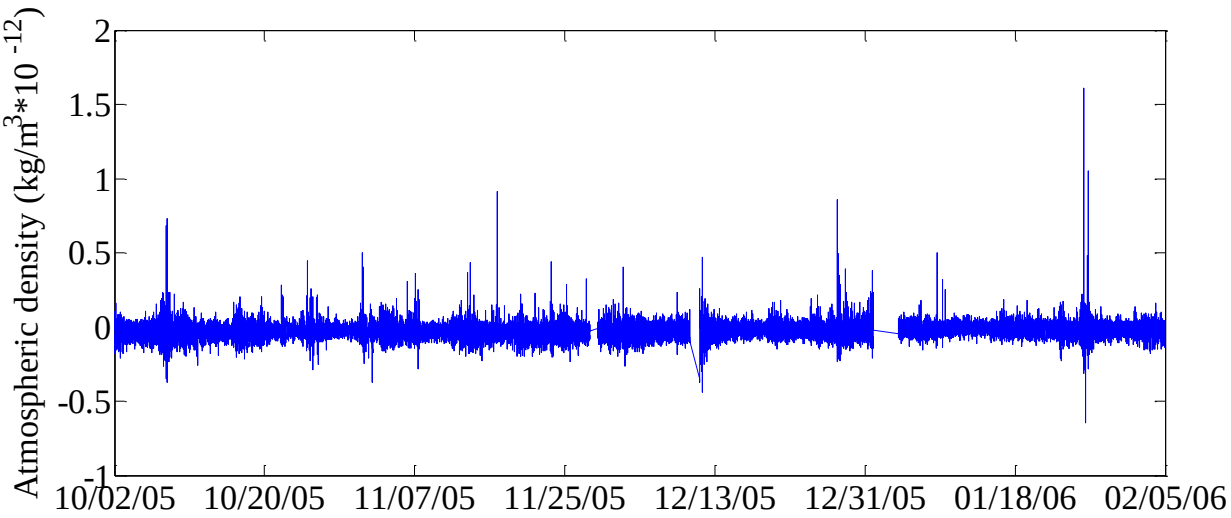

Figure 4.11: Difference between POE derived density and accelerometer derived density for GRACE-A from October 2005 to January 2006 [Ref. 49**].**

Figure 4.11 shows the difference between the accelerometer derived density and the POE derived density for the period between October 2005 to January 2006 for GRACE-A. The differences in the density have the same magnitude during the anomalous time period as the time period around it. This shows that the high frequency variations observed in the

accelerometer derived density have the same magnitude as the low magnitude daylight to eclipse density variations during the anomalous time period. Since these high frequency density variations are not observed in either the POE derived densities or the HASDM densities due to limitations of the density models, this results in low CC during the anomalous time period. According to Reference 49, the reason for low magnitude daylight to eclipse density variations for GRACE during the anomalous time period is because of the beta angle (β), where β is the angle between the satellite orbit plane and the Sun vector. At lower β angle, the satellite experiences a full daytime to eclipse cycle and if the β angle is high then it does not experience a full daytime to eclipse cycle.

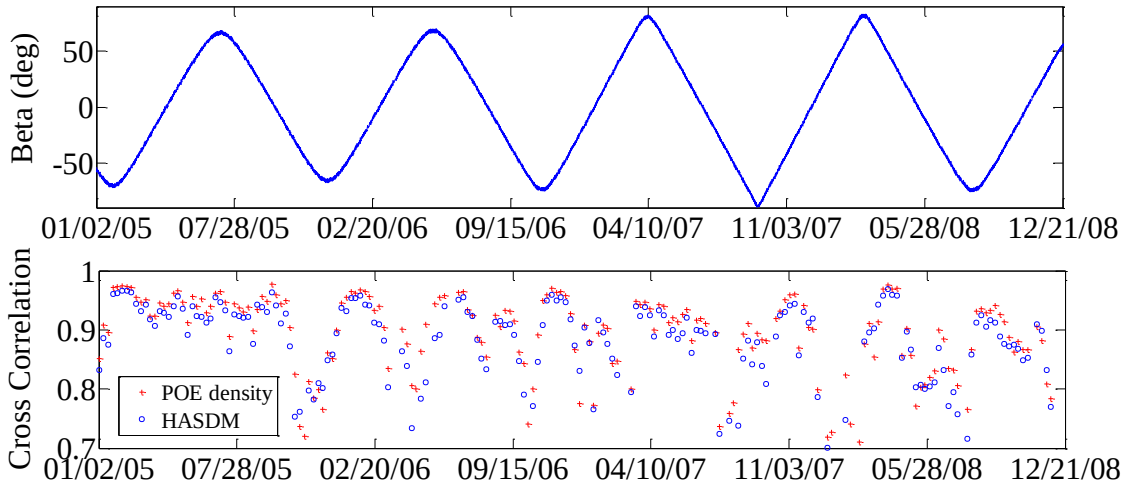

Figure 4.12: Beta angle and weekly cross correlation between POE derived density and HASDM density with accelerometer derived density for GRACE-A [Ref. 49].

Figure 4.12 shows a plot of variation of β and weekly CC between POE derived density and HASDM density with accelerometer derived density from the year 2005 to 2008. A periodic variation in the CC is observed. The first large drop in CC occurs between late 2005 and early 2006, the anomalous period mentioned above. During this time period, the β angle is

at one of its extrema and thus the orbit is nearly polar. Thus, the daytime to eclipse variation in density would be low.

Similar to Figure 4.12, the plot for CHAMP from year 2001 to 2008 is shown in Figure 4.13. Unlike GRACE, the CCs are high but still show periodic variations and are better correlated with the β angle.

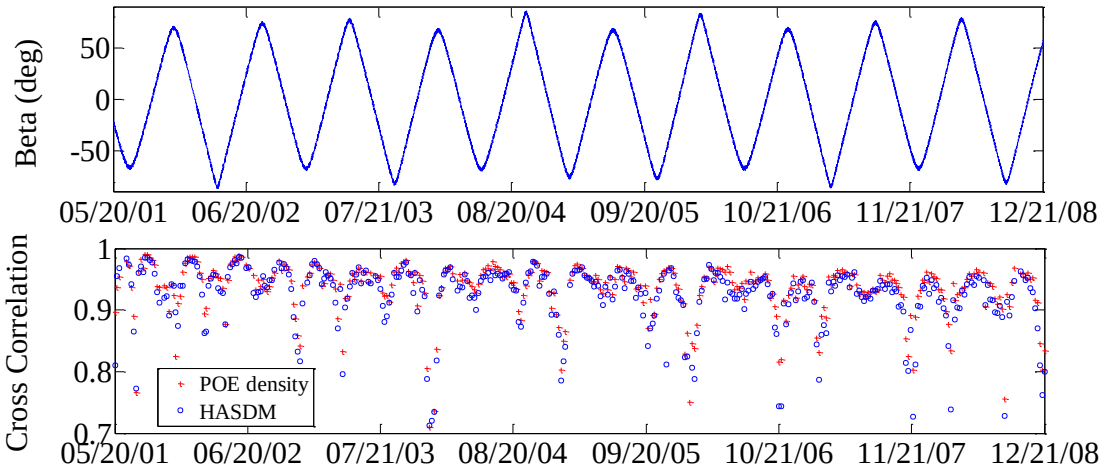

Figure 4.13: Beta angle and weekly cross correlation between POE derived density and HASDM density with accelerometer derived density for CHAMP [Ref. 49].

4.6 One Week Continuous Sets Using Sutton's Accelerometer Derived Density

One week data sets created using POE derived density using linear weighted blending technique for both CHAMP and GRACE were also compared with the accelerometer derived density obtained from Eric Sutton from the United States Air Force Research Lab by calculating the CC between the two. The accelerometer derived density for both CHAMP and GRACE are available in the University of Colorado website at http://sisko.colorado.edu/sutton/data.html. However, at the time of this writing, the data available was Version 2.2, which is not the latest version. Thus, Version 2.3 was obtained from Eric Sutton from the Air Force Research Laboratory. The HASDM density was also compared

with the accelerometer derived density for both CHAMP and GRACE, obtained from Eric Sutton, by calculating the CC between the two. *Note: Henceforth, the accelerometer derived density of both CHAMP and GRACE, obtained from Eric Sutton, will be referred to as Sutton's density, and the density obtained by Sean Bruinsma will be referred to as Bruinsma's density*. This was done for all the weeks for the entire mission life of CHAMP and GRACE, whenever data was available, using the same procedure that was used to calculate the CC using Bruinsma's density, discussed earlier in this section. The time span for which this was done was also the same as the one used for Bruinsma's density, however there were a few days when Sutton's density was available and Bruinsma's density was not, and vice-verse. For most of the cases, the cross correlation was higher for the former case.

The average cross correlation of all the weeks calculated for CHAMP are shown in Table 4.13, displayed under its respective solar and geomagnetic bin, along with the average CC for all the bins.

Table 4.13: Cross correlation coefficient for POE derived density with linear weighted blending technique and HASDM with Sutton's density, for a period of one week, for CHAMP. The highest value of cross correlation for each bin has been shade.

Bin	Cross Correlation	
	HASDM	POE derived density with linear weighted blending technique
Low Solar	0.905±0.054	0.925±0.042
Moderate Solar	0.923±0.049	0.936±0.041
Elevated Solar	0.938±0.045	0.945±0.050
High Solar	0.939±0.032	0.948±0.029
Quiet Geomagnetic	0.921±0.055	0.937±0.042
Moderate Geomagnetic	0.922±0.043	0.933±0.043
Active Geomagnetic	0.936±0.008	0.945±0.006
For all Bins	0.922±0.050	0.936±0.042

Similarly, the average cross correlation of all the weeks calculated for GRACE are shown in Table 4.14, displayed under its respective solar and geomagnetic bin, along with the average CC for all the bins.

Table 4.14: Cross correlation coefficient for POE derived density with linear weighted blending technique and HASDM with Sutton's density, for a period of one week, for GRACE. The highest value of cross correlation for each bin has been shaded.

Bin	Cross Correlation	
	HASDM	POE derived density with linear weighted blending technique
Low Solar	0.825±0.123	0.853±0.104
Moderate Solar	0.890±0.072	0.912±0.063
Quiet Geomagnetic	0.853±0.110	0.880±0.092
Moderate Geomagnetic	0.873±0.092	0.893±0.087
For all Bins	0.859±0.105	0.884±0.090

As seen in both Table 4.13 and Table 4.14, the highest CC for each bin and also the overall average, is for the case of POE derived density with linear weighted blending technique, which was expected based on previous results from Bruinsma's density.

4.6.1 'Bad' Weeks in Sutton's Data

As with Bruinsma's density, bad data in Sutton's density were suspected if CC was below 0.6. For CHAMP, the CCs for all the weeks were above 0.6, thus no bad data were suspected. Even if there were any bad data, it must have been restricted to a relatively shorter time period as compared to one week, since it did not bring the CC below 0.6. For GRACE, six weeks had CC below 0.6. These weeks and their respective CCs are given in the table below.

Table 4.15: List of weeks where CC was below 0.6 for HASDM and/or POE derived density with linear weighted blending technique for GRACE, when calculated using Sutton's density.

Week	Cross Correlation	
	HASDM	POE derived density with linear weighted blending technique
29th July to 4th August, 2007	0.596	0.646
23rd to 29th December, 2007	0.483	0.570
13th to 19th January, 2008	0.438	0.456
20th to 26th January, 2008	0.382	0.560
7th to 13th December, 2008	0.559	0.608
14th to 20th December, 2008	0.248	0.366

Plots were generated for all the weeks listed in Table 4.15 to aid in identifying the reason for low CC. All these plots had spikes of varying magnitude. But unlike the plots for GRACE during the 'bad' weeks, which were generated earlier in this section using Bruinsma's density (Figure 4.6 and Figure 4.7), none of the spikes for Sutton's density had an order of magnitude higher than the normal variation of density. To illustrate this, plots for three weeks (July 29, 2007, December 23, 2007, and December 14, 2008) are shown in the figures below.

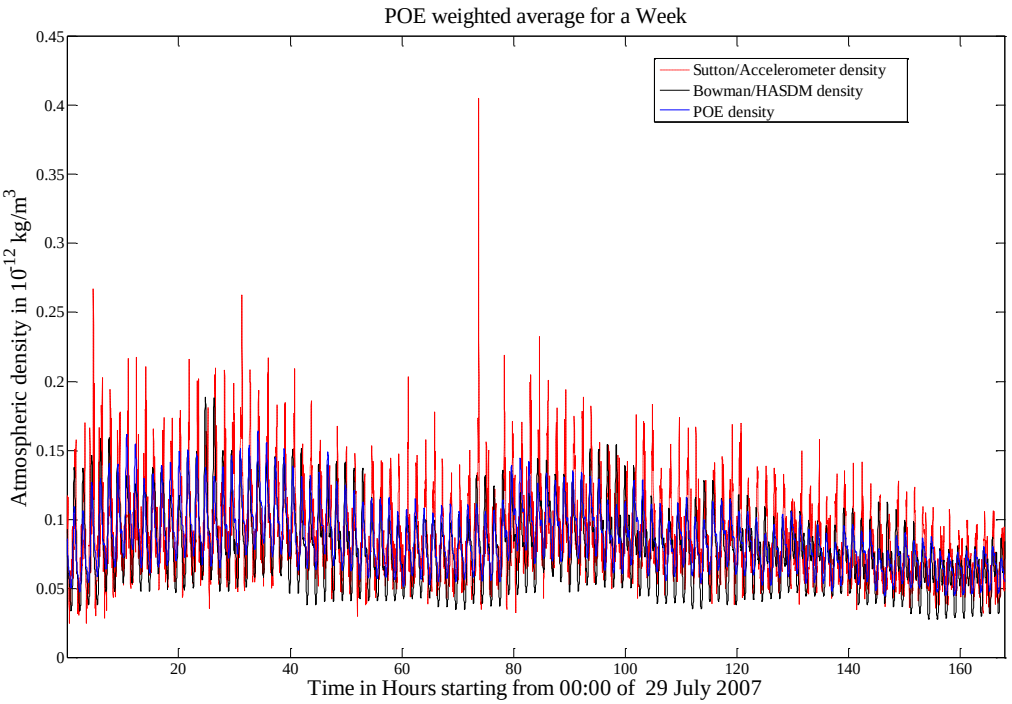

Figure 4.14: Sutton's density, precision orbit density estimates with linear weighted blending, and HASDM density, for a period of one week, from July 29, to August 4, 2007.

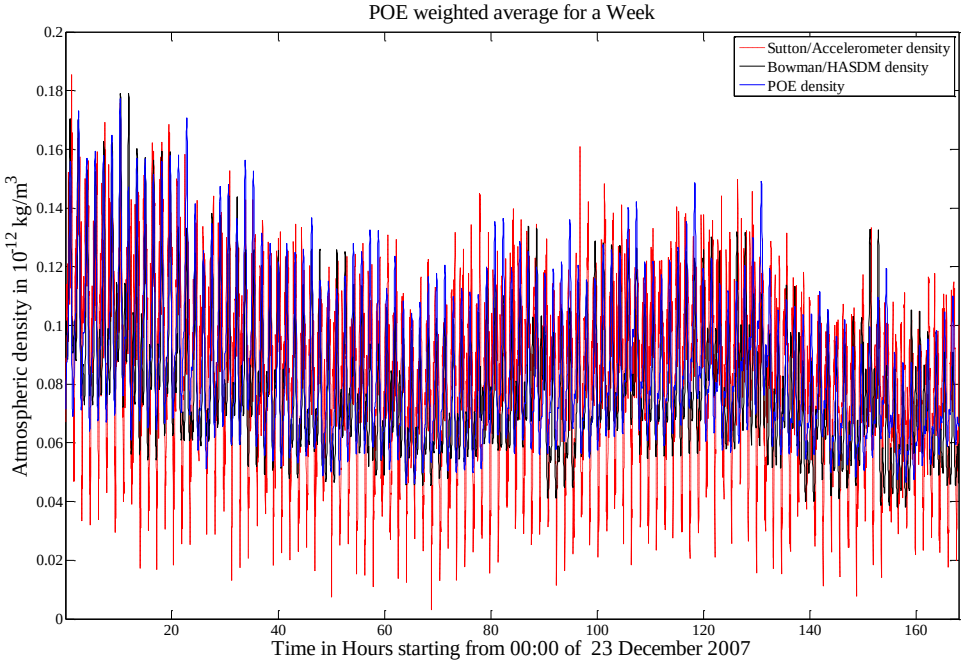

Figure 4.15: Sutton's density, precision orbit density estimates with linear weighted blending, and HASDM density, for a period of one week, from December 23 to 29, 2007.

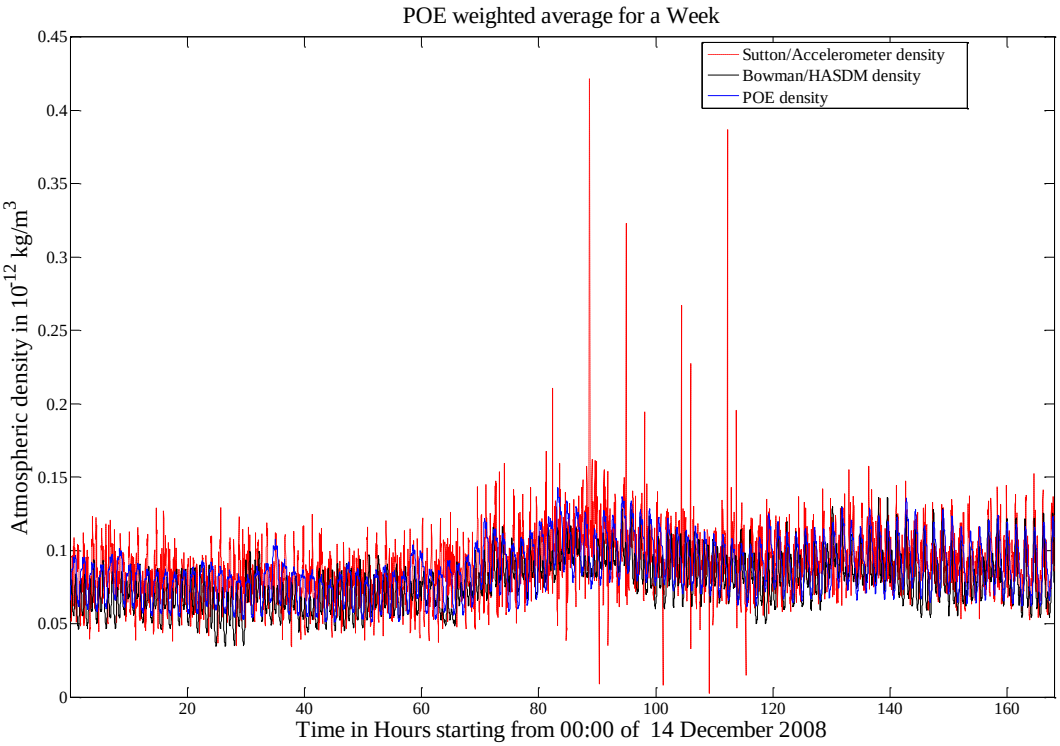

Figure 4.16: Sutton's density, precision orbit density estimates with linear weighted blending, and HASDM density, for a period of one week, from December 14 to 20, 2008.

In all three figures (Figure 4.14, Figure 4.15, and Figure 4.16), the spikes are of the same order of magnitude as the normal variation in density, even the few that are about two to four times the normal size. This is very similar to the case where some of the weeks had poor CC (below 0.6) for GRACE when compared to Bruinsma's density and no satisfactory explanation was provided. Figure 4.14 and Figure 4.8 are for the same time period, but the former is obtained using Bruinsma's density while the latter is obtained using Sutton's density. Both of them show a large spike at the same time (around 73 hours), however the magnitude of the spike on Sutton's density is less than that of Bruinsma's density. The most likely reason for poor CC for all the weeks listed in Table 4.15 is because of the presence of low magnitude spikes throughout the time span of one week. Thus none of the weeks in Table 4.15 can be discarded by claiming that the Sutton's density is performing poorly.

4.7 Comparison of Bruinsma and Sutton's Density

There are two ways to compare Bruinsma and Sutton's density. The first method is to compare the CC between each of these accelerometer derived density with HASDM and POE derived density with the linear weighted blending technique for the same period of time. Such a comparison between the two for the same weeks, after eliminating the 'bad' weeks from Bruinsma's density is shown for CHAMP and GRACE in the tables below.

Table 4.16: Cross correlation coefficient for POE derived density with linear weighted blending technique and HASDM with accelerometer derived density, for a period of one week, for CHAMP. The results shown are for using Bruinsma's density and Sutton's density for the accelerometer derived density. The highest value of cross correlation compared between the results obtained before and after removing 'bad' weeks, under the same type of densities used has been shaded for each bin (except when they are equal).

Bin	Cross Correlation			
	HASDM (Bruinsma)	HASDM (Sutton)	POE derived density with linear weighted blending technique (Bruinsma)	POE derived density with linear weighted blending technique (Sutton)
Low Solar	0.909±0.052	0.905±0.054	0.926±0.041	0.925±0.042
Moderate Solar	0.924±0.053	0.923±0.049	0.935±0.047	0.936±0.042
Elevated Solar	0.944±0.048	0.942±0.042	0.949±0.041	0.947±0.051
High Solar	0.938±0.034	0.939±0.032	0.948±0.029	0.948±0.029
Quiet Geomagnetic	0.923±0.055	0.921±0.055	0.937±0.043	0.937±0.042
Moderate Geomagnetic	0.923±0.048	0.922±0.043	0.932±0.046	0.933±0.043
Active Geomagnetic	0.942±0.013	0.936±0.008	0.950±0.007	0.945±0.006
For all Bins	0.923±0.052	0.922±0.050	0.935±0.044	0.936±0.042

Table 4.17: Cross correlation coefficient for POE derived density with linear weighted blending technique and HASDM with accelerometer derived density, for a period of one week, for GRACE. The results shown are for using Bruinsma's density and Sutton's density for the accelerometer derived density. The highest value of cross correlation compared between the results obtained before and after removing 'bad' weeks, under the same type of densities used has been shaded for each bin (except when they are equal).

Bin	Cross Correlation			
	HASDM (Bruinsma)	HASDM (Sutton)	POE derived density with linear weighted blending technique (Bruinsma)	POE derived density with linear weighted blending technique (Sutton)
Low Solar	0.820±0.133	0.826±0.125	0.843±0.121	0.852±0.106
Moderate Solar	0.896±0.068	0.891±0.073	0.913±0.064	0.913±0.063
Quiet Geomagnetic	0.852±0.188	0.853±0.112	0.874±0.107	0.880±0.093
Moderate Geomagnetic	0.878±0.090	0.873±0.092	0.892±0.087	0.893±0.087
For all Bins	0.859±0.111	0.859±0.107	0.879±0.102	0.884±0.092

In Table 4.16 and Table 4.17, the highest CC between the two types of density (Bruinsma and Sutton's density) is shaded. This only means that the accelerometer derived density whose cell is shaded has a better correlation with HASDM and POE derived density with linear weighted blending technique, and does not necessary mean that this density is more accurate than the other. For CHAMP, Bruinsma's density shows a better correlation with HASDM than Sutton's density, for all the solar and geomagnetic activity bins except the high solar activity bin. For POE derived density with linear weighted blending technique, Sutton's density has a better correlation for the overall results. For GRACE, Sutton's density shows a better correlation than Bruinsma's density for the case of POE derived density with linear weighted blending technique for all the solar and geomagnetic activity bins, except for the moderate solar activity bin where they both correlate equally well. For the case of using HASDM, Sutton's density shows better correlation than Bruinsma's density for low solar and

quite geomagnetic activity bin, and vice-versa for moderate geomagnetic activity bin, while they correlate equally well for in the remaining bins. The difference between the results of Bruinsma's density and Sutton's density is all less than 1 percent.

The other method to compare Sutton's and Bruinsma's density is to calculate the CC between the two. This is done for the entire mission life of CHAMP and GRACE for which data are available. For CHAMP, both sets of accelerometer derived density data are available from 2001 to 2009. For GRACE, both sets of accelerometer derived density data are available from 2003 to 2009. The results for CHAMP are shown in Table 4.18.

Table 4.18: Cross correlation and RMS between Sutton's density and Bruinsma's density from May 2001 to December 2009, for CHAMP. Results are calculated before removing the negative values of Bruinsma's density in the year 2002.

Time period	Cross Correlation	RMS (10^{-12} kg/m^3)
May 2001 to December 2009	0.258	6.356

Table 4.18 shows a very low CC and very high RMS between Sutton's and Bruinsma's density because Bruinsma's density had periods of very large magnitude (10^{-9} kg/m^3) negative densities in the year 2002. Two such time periods were identified; the first one was more than 36 hours between 10 AM June 10 to 11 PM June 11, 2002, and the second one was more than 17 hours between midnight of December 9 to 5 PM December 10, 2002. After removing these periods of negative densities, the CC and RMS were recalculated and the results are shown in Table 4.19.

Table 4.19: Cross correlation and RMS between Sutton's density and Bruinsma's density from May 2001 to December 2009, for CHAMP. Results are calculated after removing the negative values of Bruinsma's density in the year 2002.

Time period	Cross Correlation	RMS (10^{-12} kg/m^3)
May 2001 to December 2009	0.967	0.470

Table 4.19 shows the now improved value of CC and RMS. The CC is above 0.95 and thus there is a high correlation between Sutton's and Bruinsma's densities for CHAMP. The result for GRACE are shown in Table 4.20.

Table 4.20: Cross correlation and RMS between Sutton's density and Bruinsma's density from May 2001 to December 2009, for GRACE.

Time period	Cross Correlation	RMS (10^{-12} kg/m^3)
April 2003 to December 2009	0.991	0.042

Table 4.20 shows a high value of CC and low value of RMS. The CC is more than 0.99 and thus there is a high correlation between Sutton's and Bruinsma's densities for GRACE.

5 POE DERIVED DENSITIES FOR TerraSAR-X and ICESat

5.1 Results for TerraSAR-X

The POE derived densities were obtained for two different cases. The first method is where the area facing the Sun was calculated as a function of beta angle, where the latter was calculated at all the times when the POE was available within a 14 hour solution fit span. The average of these areas within the 14 hour fit span was used as one of the inputs in ODTK to estimate the density. The second method is where the area facing the Sun is the annual average (8.92 m^2), which was obtained in the chapter on methodology as the average of the areas facing the Sun during solstices and equinoxes.

To compare the densities obtained using these two methods, the CC and the RMS between these two densities were calculated during all the solstices and equinoxes from the time the POE data were available for TerraSAR-X. The CC and RMS were also calculated between these densities and the Jacchia-71 semi-empirical model density.

The results are displayed in the tables below. Each row is the result for a 14 hour fit span. The ones that have two dates separated by a hyphen have their period from 22:00 hours of first day to 12:00 hours of the next day, and the ones that have only one date is for a period of 10:00 hours to 24:00 hours of the same day (or equivalently 00:00 hours of the next day).

Table 5.1: Cross correlation between POE derived density obtained by using 14 hour averaged area and Jacchia-71 semi-empirical model density, POE derived density obtained by using annual averaged area and Jacchia-71 semi-empirical model density, and POE derived density obtained by using 14 hour averaged area and annual averaged area.

Year	Month and Scenario	Cross Correlation			$F_{10.7}$ (SFU)	A_p
		Variable Area vs Jacchia-71	Annual average area vs Jacchia-71	Variable Area vs Annual average area		
2007	Sept. 22-23	0.896	0.896	1.000	66.7	12
	Sept. 23	0.791	0.791	1.000	66.7	12
	Dec. 21-22	0.913	0.913	1.000	71.5	9
	Dec. 22	0.915	0.915	1.000	71.5	9
2008	March 19-20	0.843	0.843	1.000	68.4	8
	March 20	0.867	0.867	1.000	68.4	8
	June 19-20	0.966	0.966	1.000	65.2	9
	June 20	0.908	0.908	1.000	65.2	9
	Sept. 21-22	0.778	0.778	1.000	69.1	4
	Sept. 22	0.949	0.949	1.000	69.1	4
	Dec. 20-21	0.914	0.914	1.000	0	1
	Dec. 21	0.945	0.945	1.000	0	1
2009	March 19-20	0.839	0.839	1.000	68.7	4
	March 20	0.978	0.978	1.000	68.7	4
	June 20-21	0.929	0.929	1.000	71.5	5
	June 21	0.947	0.947	1.000	71.5	5
	Sept. 21-22	0.972	0.972	1.000	74.7	3
	Sept. 22	0.957	0.957	1.000	74.7	3
	Dec. 20-21	0.971	0.971	1.000	82.7	3
	Dec. 21	0.975	0.975	1.000	82.7	3
2010	March 19-20	0.982	0.982	1.000	83.5	6
	March 20	0.982	0.982	1.000	83.5	6
	June 20-21	0.977	0.977	1.000	72	4
	June 21	0.943	0.943	1.000	72	4
	Sept. 22-23	0.993	0.993	1.000	84.3	6
	Sept. 23	0.995	0.995	1.000	84.3	6
	Dec. 20-21	0.902	0.902	1.000	77.9	2

	Dec. 21	0.986	0.986	1.000	77.9	2
2011	March 19-20	0.995	0.995	1.000	92	6
	March 20	0.975	0.975	1.000	92	6
	June 20-21	0.998	0.998	1.000	96.4	7
	June 21	0.936	0.936	1.000	96.4	7
	Sept. 22-23	0.955	0.955	1.000	158.2	2
	Sept. 23	0.979	0.979	1.000	158.2	2
	Dec. 21-22	0.969	0.969	1.000	145.8	4
	Dec. 22	0.990	0.990	1.000	145.8	4

Table 5.2: Root mean square between POE derived density obtained by using 14 hour averaged area and Jacchia-71 semi-empirical model density, POE derived density obtained by using annual averaged area and Jacchia-71 semi-empirical model density, and POE derived density obtained by using 14 hour averaged area and annual averaged area.

Year	Month and Scenario	RMS (10^{-12} kg/m^3)			$F_{10.7}$ (SFU)	A_p
		Variable Area vs Jacchia-71	Annual average area vs Jacchia-71	Variable Area vs Annual average area		
2007	Sept. 22-23	0.061	0.061	0.000	66.7	12
	Sept. 23	0.052	0.052	0.000	66.7	12
	Dec. 21-22	0.052	0.052	0.000	71.5	9
	Dec. 22	0.035	0.035	0.000	71.5	9
2008	March 19-20	0.057	0.057	0.000	68.4	8
	March 20	0.057	0.057	0.000	68.4	8
	June 19-20	0.024	0.024	0.000	65.2	9
	June 20	0.024	0.024	0.000	65.2	9
	Sept. 21-22	0.044	0.044	0.000	69.1	4
	Sept. 22	0.026	0.026	0.000	69.1	4
	Dec. 20-21	0.011	0.011	0.000	0	1
	Dec. 21	0.010	0.010	0.000	0	1
2009	March 19-20	0.039	0.039	0.000	68.7	4
	March 20	0.027	0.027	0.000	68.7	4
	June 20-21	0.029	0.029	0.000	71.5	5
	June 21	0.030	0.030	0.000	71.5	5
	Sept. 21-22	0.022	0.022	0.000	74.7	3
	Sept. 22	0.023	0.023	0.000	74.7	3
	Dec. 20-21	0.017	0.017	0.000	82.7	3
	Dec. 21	0.006	0.006	0.000	82.7	3
2010	March 19-20	0.026	0.026	0.000	83.5	6
	March 20	0.022	0.022	0.000	83.5	6
	June 20-21	0.014	0.014	0.000	72	4
	June 21	0.013	0.013	0.000	72	4
	Sept. 22-23	0.007	0.007	0.000	84.3	6
	Sept. 23	0.012	0.012	0.000	84.3	6
	Dec. 20-21	0.028	0.028	0.000	77.9	2

	Dec. 21	0.005	0.005	0.000	77.9	2
2011	March 19-20	0.066	0.066	0.000	92	6
	March 20	0.061	0.061	0.000	92	6
	June 20-21	0.005	0.005	0.000	96.4	7
	June 21	0.027	0.027	0.000	96.4	7
	Sept. 22-23	0.097	0.097	0.000	158.2	2
	Sept. 23	0.085	0.085	0.000	158.2	2
	Dec. 21-22	0.103	0.103	0.000	145.8	4
	Dec. 22	0.046	0.046	0.000	145.8	4

Table 5.1 shows that the CC between POE derived density using the 14 hour averaged area and the Jacchia-71 semi-empirical model density agree with that obtained by using the annual averaged area and the Jacchia-71 semi-empirical model up to five places after the decimal point for most cases. The CC between POE derived density using the 14 hour averaged area and the annual averaged area is very close to one (the value nine exists up to at least seven places after the decimal point for all cases).

Table 5.2 shows that the RMS between POE derived density using the 14 hour averaged area and Jacchia-71 semi-empirical model density agree with that obtained by using the annual averaged area and Jacchia-71 semi-empirical model up to five places after the decimal point for most cases (and they are both less than 0.1 for all the cases). The RMS between the POE derived density using the 14 hour averaged area and the annual averaged area is very close to zero and is on the order of 10^{-18} kg/m^3.

5.1.1 Results from Start of TerraSAR-X Mission to February 2012

Similarly, the CC and the RMS between the densities obtained by using the 14 hour average area facing the Sun and the annual average area facing the Sun, were calculated for all

the available scenarios from the start of the mission life of TerraSAR-X to February 2012. CC and RMS were also calculated between these densities and the Jacchia-71 semi-empirical model density. The average CC and RMS for this duration of the mission were calculated and binned according to their solar and geomagnetic activity and are given in Table 5.3 and Table 5.4. When TerraSAR-X was launched in the year 2007, neither the solar nor geomagnetic activity were high or active, respectively until February 2012, the time up to which the TerraSAR-X data was collected for this research. The only exception being September 24, 2011 when the solar activity was high with an $F_{10.7}$ value equal to 190.4 SFU, and also April 5, 2010 when the geomagnetic activity was active with an A_p value equal to 55. Thus, unlike other solar and geomagnetic activity bins, the high solar activity bin and the active geomagnetic activity bin results for CC and RMS are based on just one day and not an average of multiple days.

Table 5.3. Cross correlation between POE derived density obtained by using 14 hour averaged area and Jacchia-71 semi-empirical model density, POE derived density obtained by using annual averaged area and Jacchia-71 semi-empirical model density, and POE derived density obtained by using 14 hour averaged area and annual averaged area.

Bin	Cross Correlation		
	Variable Area vs Jacchia-71	Annual average area vs Jacchia-71	Variable Area vs Annual average area
Low Solar	0.923±0.094	0.923±0.094	1.000±0.000
Moderate Solar	0.950±0.073	0.950±0.075	0.999±0.022
Elevated Solar	0.968±0.047	0.968±0.047	1.000±0.000
High Solar	0.991±0.000	0.991±0.000	1.000±0.000
Quiet Geomagnetic	0.940±0.083	0.939±0.084	1.000±0.016
Moderate Geomagnetic	0.916±0.095	0.916±0.095	1.000±0.000
Active Geomagnetic	0.822±0.005	0.822±0.005	1.000±0.000
For all Bins	0.936±0.085	0.936±0.086	1.000±0.015

Table 5.4. Root mean square between POE derived density obtained by using 14 hour averaged area and Jacchia-71 semi-empirical model density, POE derived density obtained by using annual averaged area and Jacchia-71 semi-empirical model density, and POE derived density obtained by using 14 hour averaged area and annual averaged area.

Bin	RMS (10^{-12} kg/m^3)		
	Variable Area vs Jacchia-71	Annual average area vs Jacchia-71	Variable Area vs Annual average area
Low Solar	0.028	0.028	0.000
Moderate Solar	0.049	0.049	0.000
Elevated Solar	0.188	0.188	0.000
High Solar	0.070	0.070	0.000
Quiet Geomagnetic	0.037	0.037	0.000
Moderate Geomagnetic	0.064	0.064	0.000
Active Geomagnetic	0.107	0.107	0.000
For all Bins	0.041	0.041	0.000

Table 5.3 shows that the CC is above 0.9 for all bins except the active geomagnetic bin. But the CC of the active geomagnetic bin is based on just one day and not an average of several days. A higher CC indicates that the correlation between the density under consideration and the Jacchia-71 density is high, and does not necessary mean that the density under consideration is performing better than the other. This is because Jacchia-71 is not the most accurate density, unlike the accelerometer derived density. However, TerraSAR-X has no accelerometer onboard. The CCs between the POE derived density obtained by using the 14 hour averaged area and the annual averaged area are all equal to one except for the moderate solar activity bin. Even for the moderate solar activity bin, the CC is very close to one.

Table 5.4 shows that the RMS is below 0.1 for all the bins except the elevated solar and active geomagnetic bins. A lower RMS indicates that the density under consideration is closer to the Jacchia-71 density, and does not necessary mean that the density under consideration is

more accurate than the other. This is because Jacchia-71 is not the most accurate density. The RMS between the POE derived density obtained by using the 14 hour averaged area and the annual averaged area all equal to zero up to three decimal places.

Similarly, the CC and the RMS for the densities obtained by using the 14 hour average area facing the Sun with the semi-empirical model density, NRLMSISE-2000, were calculated for all the available scenarios from the start of the mission life of TerraSAR-X to February 2012. The average values of CC and RMS for this duration of the mission were calculated and binned by solar and geomagnetic activity and are given in Table 5.5 and Table 5.6. Table 5.5 and Table 5.6 also have the results of CC and RMS for the densities obtained by using the 14 hour average area facing the Sun with the Jaccia-71 density, from Table 5.3 and Table 5.4, respectively.

Table 5.5. Cross correlation between POE derived density obtained by using 14 hour averaged area and NRLMSISE-2000 semi-empirical model density. The highest value of cross correlation between the first two columns for each bin has been shaded.

Bin	Cross Correlation	
	Variable Area vs Jacchia-71	Variable Area vs NRLMSISE-2000
Low Solar	0.923±0.094	0.879±0.101
Moderate Solar	0.950±0.073	0.920±0.075
Elevated Solar	0.968±0.047	0.950±0.050
High Solar	0.991±0.000	0.982±0.000
Quiet Geomagnetic	0.940±0.083	0.906±0.086
Moderate Geomagnetic	0.916±0.095	0.858±0.109
Active Geomagnetic	0.822±0.005	0.783±0.049
For all Bins	0.936±0.085	0.899±0.091

Table 5.6. Root mean square between POE derived density obtained by using 14 hour averaged area and NRLMSISE-2000 semi-empirical model density. The lowest value of RMS between the first two columns for each bin has been shaded.

Bin	RMS (10^{-12} kg/m^3)	
	Variable Area vs Jacchia-71	Variable Area vs NRLMSISE-2000
Low Solar	0.028	0.033
Moderate Solar	0.049	0.057
Elevated Solar	0.188	0.164
High Solar	0.070	0.225
Quiet Geomagnetic	0.037	0.045
Moderate Geomagnetic	0.064	0.061
Active Geomagnetic	0.107	0.063
For all Bins	0.041	0.047

Table 5.5 shows that the POE derived density has higher correlation with the Jacchia-71 density than the NRLMSISE-2000 density, for most solar and geomagnetic activity bins. Table 5.6 shows that the value of RMS between the POE derived density and the Jacchia-71 density is lower than between the POE derived density and the NRLMSISE-2000 density when the average of all the solar and geomagnetic bins is considered. This is probably because the POE derived density used the CIRA 1972 as the baseline density model and thus the POE derived density is expected to correlate better with the Jacchia based family of density models.

5.2 Results for ICESat

The POE derived densities were obtained for two different cases. The first method is where the satellite areas facing the Sun, facing the Earth, and normal to the velocity vector were calculated using the algorithm presented in Reference 78 and discussed in the chapter on methodology. The areas were calculated at each time when the POE data were available for a

total period of 30 hours, and the 30-hour averages were used as the input areas in ODTK. The second method is by using the areas which were used in Reference 50 to estimate the POE derived densities. The areas used by Arudra [Ref. 50] that are normal to the velocity vector, facing the Earth, and facing the Sun were 6.72 m^2, 9.22 m^2, and 6.97 m^2 respectively, the reason for using these values is not specified.

To compare the densities obtained using these two methods, the CC and the RMS between the two densities was calculated for each day from a solar and geomagnetic activity bin–one day with low solar and geomagnetic activity, another day with moderate geomagnetic activity, with high geomagnetic activity, with moderate solar activity, with elevated solar activity, and with high solar activity. The CC and RMS were also calculated between these densities and the Jacchia-71 semi-empirical model density.

The results are displayed in the tables below. Each row is the result for a 30-hour fit span. For all the days, the starting time is 21:00 hours (9 PM) the day before, and the ending time is 3:00 hours (3 AM) the next day, thus a total of 30-hours.

Table 5.7: Table showing the cross correlation between POE derived density obtained by using 30-hour averaged area and Jacchia-71 model density, POE derived density obtained by using area from reference 50 and Jacchia-71 model density, and POE derived density obtained by using 30-hour averaged area and area from reference 50. The baseline density model used is CIRA 1972 with BC and density correlated half lives of 1.8 and 180 minutes, respectively.

Year	Month and Day	Cross Correlation			$F_{10.7}$ (SFU)	A_p
		Variable Area vs Jacchia-71	Area from reference 50 vs Jacchia-71	Variable Area vs Area from reference 50		
2008	October 17th	0.588	0.562	0.997	70	2
2007	October 3rd	0.592	0.562	0.997	67.3	17
2005	May 30th	0.589	0.562	0.994	94.9	90
2006	February 28th	0.587	0.562	0.997	77.1	4
2003	October 29th	0.598	0.562	0.993	152.7	11
2003	March 9th	0.576	0.562	0.995	279.1	204

Table 5.8: Table showing the root mean square between POE derived density obtained by using 30-hour averaged area and Jacchia-71 model density, POE derived density obtained by using area from reference 50 and Jacchia-71 model density, and POE derived density obtained by using 30-hour averaged area and area from reference 50. The baseline density model used is CIRA 1972 with BC and density correlated half lives of 1.8 and 180 minutes, respectively.

Year	Month and Day	RMS (10^{-12} kg/m^3)			F10.7 (SFU)	Ap
		Variable Area vs Jacchia-71	Area from reference 50 vs Jacchia-71	Variable Area vs Area from reference 50		
2008	October 17th	0.160	0.150	0.017	70	2
2007	October 3rd	0.160	0.150	0.017	67.3	17
2005	May 30th	0.135	0.150	0.028	94.9	90
2006	February 28th	0.160	0.150	0.017	77.1	4
2003	October 29th	0.135	0.150	0.029	152.7	11
2003	March 9th	0.136	0.150	0.027	279.1	204

Table 5.7 shows that the CC between the POE derived density estimate using the 30-hour averaged area and the Jacchia-71 model density differ insignificantly with that obtained by using the area from reference 50 and the Jacchia-71 model density for all the cases. The POE derived density estimate using 30-hours averaged area as input shows higher correlation than using areas from reference 50 for all solar and geomagnetic activity bins. A higher CC indicates that the correlation is high between the density under consideration and the Jacchia-71 density, but does not necessary mean that the density under consideration is performing better than the other. This is because Jacchia-71 is not the most accurate density, unlike the accelerometer derived density. But ICESat has no accelerometer onboard. A better way to compare the densities estimated using the two different sets of areas is by calculating the CC between the two, which is also presented in Table 5.7. The CC between the densities estimated using the two different sets of areas are all above 0.99, thus exhibiting high correlation.

Table 5.8 shows that the RMS between POE derived density using the 30-hour averaged area and the Jacchia-71 model density differ insignificantly with that obtained by using the area from reference 50 and the Jacchia-71 model density for all the cases.

Since the CC for all the days examined in Table 5.7 is low, further investigation to determine the reason for low CC was done. The first step is to examine the density plots. The density plots for two days, one corresponding to high solar and active geomagnetic activity (October 29, 2003), and the other corresponding to low solar and quiet geomagnetic activity (October 17, 2008) are shown in Figure 5.1 and Figure 5.2.

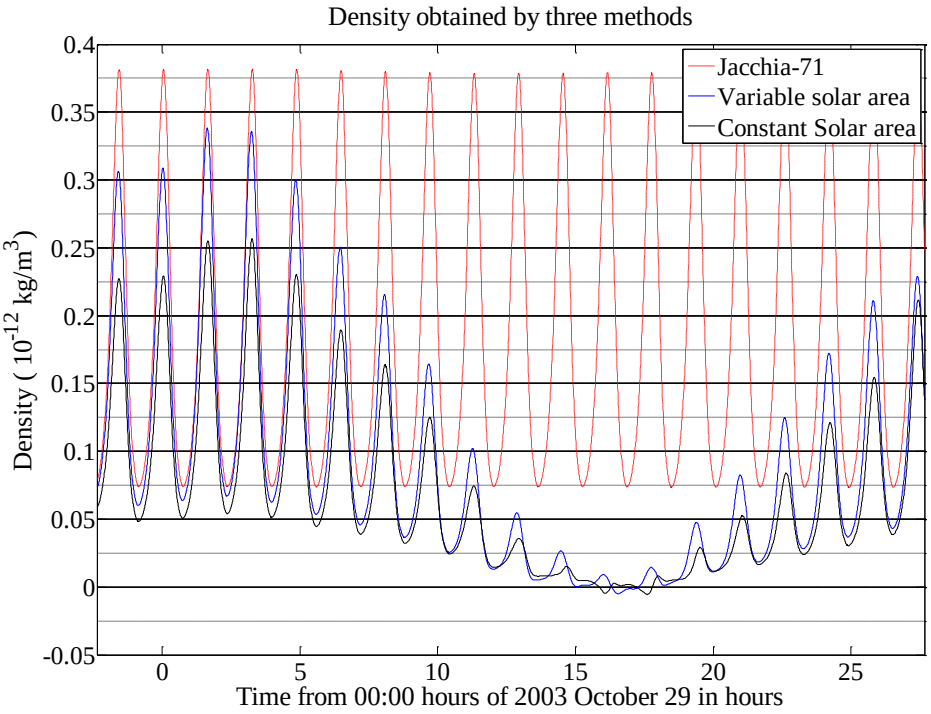

Figure 5.1: Density plots for 30-hour span on October 29, 2003 (high solar and active geomagnetic activity).

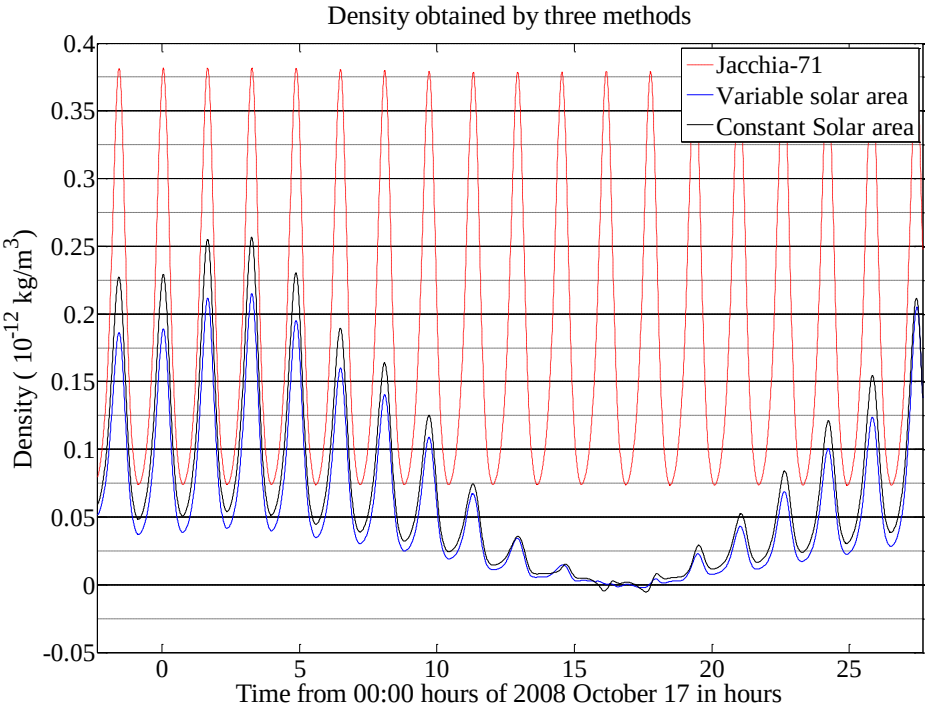

Figure 5.2: Density plots for 30-hour span on October 17, 2008 (low solar and quiet geomagnetic activity).

In both Figure 5.1 and Figure 5.2, not only do the POE derived densities underestimate the density values as compared to the Jacchia-71 density by a large amount, the central portion of the plots indicated negative density, which is physically impossible. The region where the POE derived density values dip to very low positive values and negative values (from about 10:00 hours to 19:00 hours in both the plots) does not exhibit a clear diurnal variation like the plot from the Jacchia-71 model. This anomalous behavior of the POE derived density estimates is the cause for the low CC between the POE derived densities and Jacchia-71 model densities. This anomalous behavior requires further investigation.

To see how the areas facing the Sun, Earth, and the plane normal to the velocity vector vary along the path of the satellite, plots of the areas for October 29, 2003 and October 17, 2008 are shown in Figure 5.3 and Figure 5.4, along with the density plots on the top.

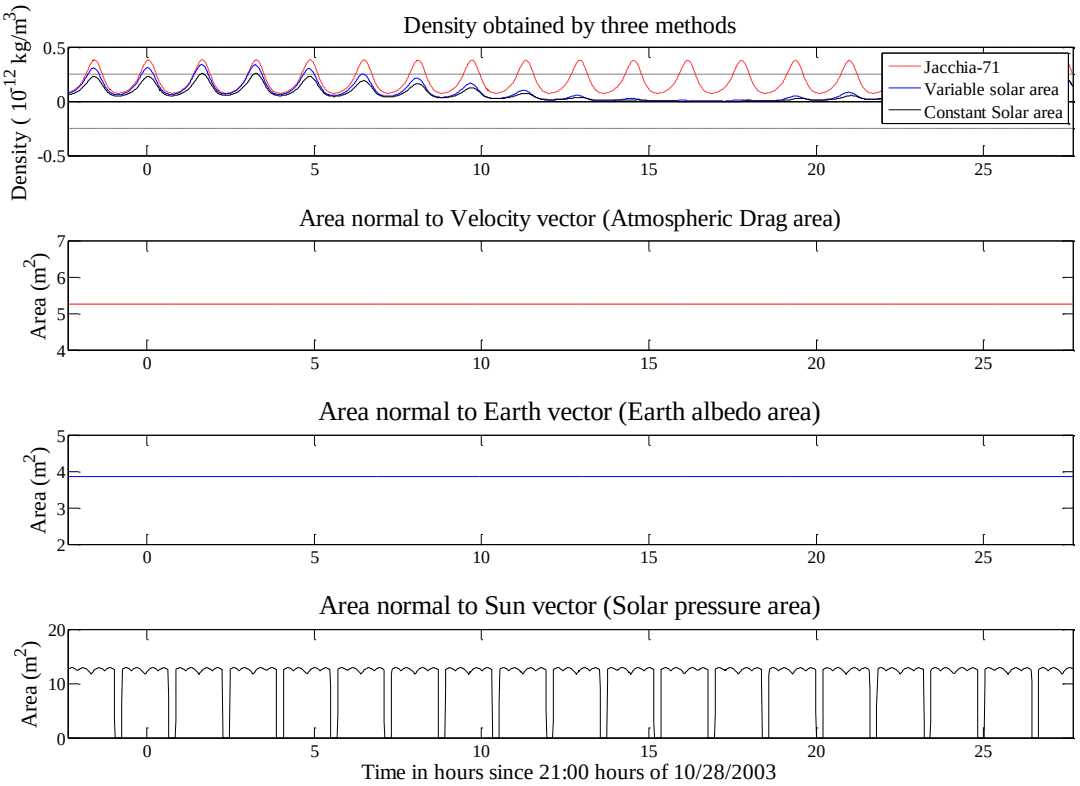

Figure 5.3: Variation of area facing the plane normal to the velocity vector, the Earth, and the Sun along the path of ICESat for a period of 30-hours on October 29, 2003.

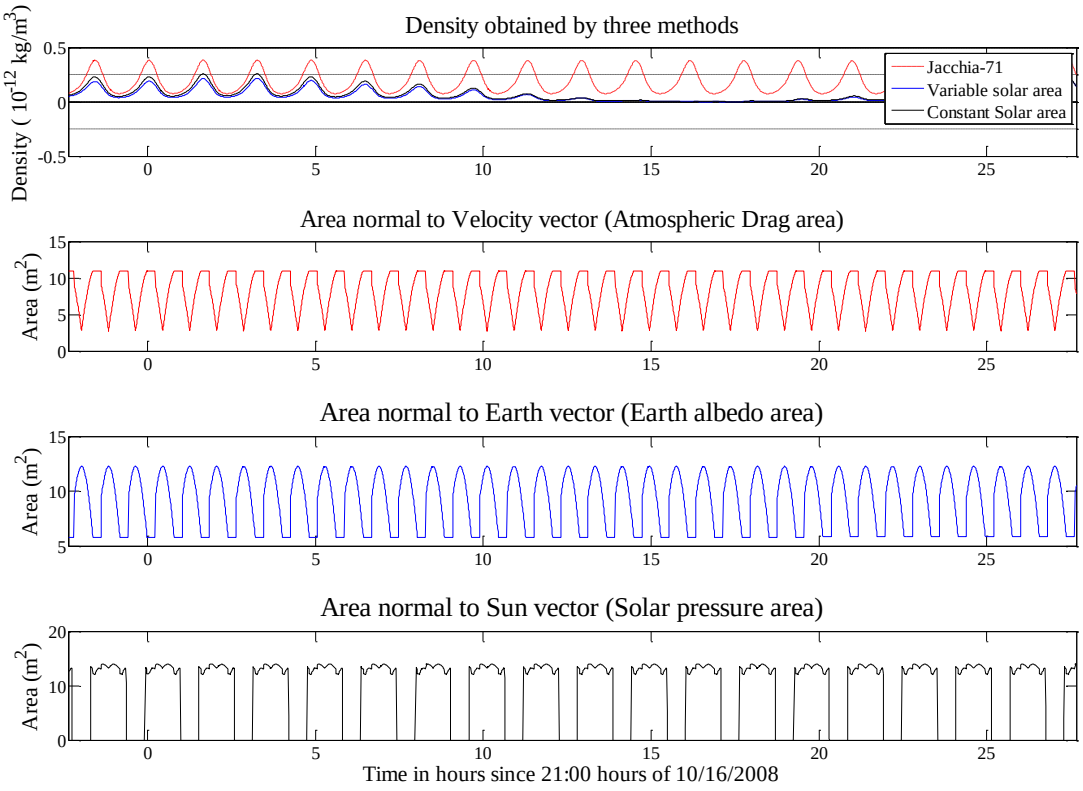

Figure 5.4: Variation of area facing the plane normal to the velocity vector, the Earth, and the Sun along the path of ICESat for a period of 30-hours on October 17, 2008.

In Figure 5.3, one can see variation of areas normal to the Sun vector, while the area facing the plane normal to the velocity vector as well as the area facing the Earth remains at a constant value. This is because the beta angle is greater than 55 degrees during this period (end of October 2003) and therefore the solar panels do not track the Sun and thus the area facing these two remain the same. But the area facing the Sun continues to change as the satellite orbits around the Earth. However, in Figure 5.4, the area facing the Sun vector, area facing the plane normal to the velocity vector, and the area facing the Earth all vary with time. This is because the beta angle is about -31 degrees during this period (mid October 2008) and therefore

ICESat is operating in the airplane mode and the solar panels track the Sun and thus all three areas vary with respect to time.

POE derived densities were also estimated for all the days given in Table 5.7 but without estimating the BC. CC and RMS were calculated between the two densities as shown in Table 5.7 and Table 5.8. However, the results were no different than those given in Table 5.7 and Table 5.8, thus estimating or not estimating the BC has no effect on the POE derived densities for ICESat for the days examined in Table 5.7. As mentioned earlier in the chapter on methodology, the drag coefficient used was 2.6. A drag coefficient of 2.0 and 3.0 were also used to estimate POE derived densities, but the results still showed very low positive values and negative values (from about 10:00 hours to 19:00 hours in both the plots), similar to Figure 5.1 and Figure 5.2. So drag coefficient is not the cause for the negative POE derived densities.

6 SUMMARY, CONCLUSIONS, AND FUTURE WORK

6.1 Summary

Atmospheric drag is the most uncertain non-conservative force acting on a low Earth orbiting satellite. The existing atmospheric density models are not accurate enough to model the variations in density that significantly affect the drag on satellites since drag is directly proportional to atmospheric density.

In this research, POE are used as measurements in an optimal orbit determination technique to estimate corrections to existing atmospheric density models. These corrections improve the drag estimates, which in turn improve orbit determination and prediction and also provide a better understanding of the upper atmosphere.

The POE are used as measurements in a sequential measurement and filtering scheme using the Orbit Determination Tool Kit (ODTK) software, which provides the orbit determination. ODTK has five atmospheric density models inbuilt, which are used as baseline atmospheric density models to which corrections are made in the orbit determination. The density models are Jacchia 1971, Jacchia-Roberts, CIRA 1972, MSISE 1990, and NRLMSISE 2000. The user can specify the ballistic coefficient correlated half-life and density correlate half-life. These half-lives are usually given values of 1.8, 18, or 180 minutes.

The POE derived densities are validated by comparing them with accelerometer derived densities, for satellites which have accelerometers onboard, such as CHAMP and GRACE. The trend in the variation is compared quantitatively by calculating the cross correlation between the two densities, and the magnitude is compared by calculating the root mean square between the two. Accelerometer derived densities are densities derived from accelerometer

measurements of satellites. Sean Bruinsma of CNES has derived the densities from accelerometers present onboard CHAMP and GRACE satellites and Eric Sutton of the United States Air Force Research Laboratory has done the same. While the accelerometer derived density derived by Sutton is used for some of the study in this research, all the studies make use of accelerometer density derived by Bruinsma. The details are given in the appropriate sections.

The effect of different functions of geomagnetic planetary amplitude (a_p) as inputs in orbit determination to estimate atmospheric density was investigated. The three different functions of input are 3-hourly a_p step functions, linear interpolated a_p functions, and a_p osculating spline functions. These three different types of functions were used as inputs for three different combinations of BC and density correlated half-life of 1.8, 18, and 180 minutes in ODTK, and POE derived density was estimated for both CHAMP and GRACE. The POE derived densities were compared with the accelerometer derived densities by calculating the CC and RMS.

To create continuous data sets of POE derived densities that span a period of one week two different methods were investigated. The first one was to blend the 14 hour POE derived densities in their overlap periods using the linear weighted blending technique. The second method was to blend the same overlap periods using the linear weighted blending technique for the position vectors of the POE, and then use it as measurements in the optimal orbit determination technique to estimate the densities. Both of them were compared with Bruinsma's accelerometer derived density by calculating their cross correlation. After preliminary studies, the former method showed a higher correlation with the accelerometer derived densities and so the former method was used to create continuous data sets of POE derived densities that span a period of one week. CIRA 1972 was used as the baseline

atmospheric density model and a BC correlated half-life of 1.8 minutes and density correlated half-life of 180 minutes were used as inputs in ODTK to generate these POE derived density estimates. These one week continuous POE derived densities showed better correlation with both Bruinsma's and Sutton's accelerometer derived densities than HASDM densities, for both CHAMP and GRACE.

The average cross sectional area of the satellite that is normal to the velocity vector, the area facing the Sun, and the area facing the Earth, had to be determined so that these areas can be used to estimate the atmospheric drag, solar radiation pressure, and Earth radiation pressure (infrared and Earth albedo), respectively. This was done for both TerraSAR-X and ICESat.

For TerraSAR-X, the area normal to the velocity vector was assumed be a constant and equal to the frontal area, and the area facing the Earth was also assumed to be constant. However, the area facing the Sun varied with time. The average area facing the Sun for a period of 14 hours and also the annual average area were calculated and used to calculate the POE derived densities. The POE derived densities were calculated by using CIRA 1972 as the baseline atmospheric density model and using a BC and density correlated half-life of 1.8 and 180 minutes, respectively. The POE derived densities calculated using these two different average areas facing the Sun were found to be very similar. Since TerraSAR-X does not have an accelerometer onboard, the POE derived densities could not be compared with accelerometer derived densities, but instead were compared with Jacchia-71 densities since this was also one of the outputs from ODTK. The POE derived densities were also compared with NRLMSISE-2000 densities, but the results showed a lower correlation than the case when the former was compared with Jacchia-71 densities. This is probably because the POE derived

density used CIRA 1972 as the baseline density model and thus the POE derived density is expected to correlate better with the Jacchia family of density models.

The attitude of ICESat as a function of beta angle was given in the literature and so was the average area of each side of the satellite when it was modeled as a rectangular box with two solar panels. This information was used to estimate the 30-hour average areas normal to the velocity vector, facing the Earth, and facing the Sun, for ICESat. The POE derived densities using these areas were estimated by ODTK and compared with Jacchai-71 density model. CIRA 1972 was used as the baseline atmospheric density model and a BC and density correlated half-life of 1.8 and 180 minutes, respectively, were used as inputs in ODTK.

6.2 Conclusions

Based on the results obtained by performing this research, the following conclusions are drawn.

1. Using a_p spline functions as input performs better than linear interpolated a_p functions and 3-hourly a_p step functions for both CHAMP and GRACE.
2. When a_p spline functions are used as the input, the best value of CC corresponds to the baseline density model, CIRA 1972, with BC and density correlated half-life combination of 1.8-18 minutes, for CHAMP.
3. When a_p spline functions are used as the input, the best value of RMS corresponds to the baseline density model, CIRA 1972, with BC and density correlated half-life combination of 1.8-180 minutes, for CHAMP.

4. When a_p spline functions are used as the input, the best value of both CC and RMS corresponds to the baseline density model, CIRA 1972, with BC and density correlated half-life combination of 1.8-180 minutes, for GRACE.
5. POE derived density found using the linear weighted blending technique in the density overlap regions shows higher correlation with Bruinsma's accelerometer derived density than the POE derived densities obtained using linear weighted blending of POE as measurements in ODTK for all the solar and geomagnetic bins, for both CHAMP and GRACE. Thus, the former is used to create continuous data sets.
6. POE derived density found using the linear weighted blending technique in the density overlap regions shows higher correlation with both Bruinsma's and Sutton's accelerometer derived density than the HASDM densities for all the solar and geomagnetic bins for both CHAMP and GRACE.
7. For CHAMP, POE derived density with the linear weighted blending technique exhibits a better correlation with Sutton's density than Bruinsma's density for the overall results.
8. For GRACE, POE derived density with linear weighted blending technique exhibits a better correlation with Sutton's density than Bruinsma's density for all the solar and geomagnetic activity bins except for the moderate solar activity bin where they both correlate equally well. This observation is also true for the overall results.
9. For TerraSAR-X, the CC between the POE derived densities obtained by using the 14 hour average area facing the Sun and the annual average area facing the Sun with

the Jacchia-71 model densities are greater than 0.9 for all bins except the active geomagnetic bin.

10. For TerraSAR-X, the CC between POE derived density obtained by using the 14 hour averaged area and the annual averaged area all are equal to one, except for the moderate solar activity bin where the CC is very close to one. The RMS between the two are all equal to zero up to three decimal places This shows that either one of the areas can be used as input without a significant difference in the estimated densities.
11. For TerraSAR-X, the CC between POE derived density obtained by using the 14 hour averaged area and the Jacchia-71 model density is higher than the CC between the former and the NRLMSISE-2000 density.
12. Even though the variation of different 30-hour averaged areas for ICESat was calculated and used in the OD to estimate the POE derived densities, the densities still showed negative values. Further examination is required to explain this phenomenon.

6.3 Future Work

There is still scope for further research into the topics that were covered in this thesis. Some of the suggested future work is given this section.

6.3.1 Creating Continuous Data Sets for Other Satellites

Continuous data sets with a period of one week were created for CHAMP and GRACE whenever the POE data was available. The next task is to do the same for other satellites such as TerraSAR-X, ICESat, and other satellites for which POE data are available. This is to create a database of POE derived densities for use in thermosphere modeling and other applications.

6.3.2 Using the Jacchia-Bowman Atmospheric Density Model as the Baseline Density Model

ODTK has only five baseline density models and they use a_p inputs that are available once every 3 hours and $F_{10.7}$ which are available on a daily basis. Since solar and geomagnetic activity are available with higher temporal resolutions, including direct measurement of EUV flux from satellites, using an atmospheric density model that uses these new types of measurements as inputs might yield better results if used as a baseline density model to which corrections are made. Such a model is the Jacchia-Bowman 2008 model and its implementation into ODTK might provide better POE derived density estimates.

6.3.3 Attitude of TerraSAR-X

The attitude of TerraSAR-X used in this research was based on several assumptions. The exact attitude of TerraSAR-X can be determined from the quaternion file available from the GFZ potsdam website, but due to lack of documentation the file was not used in this research. Using exact dimensions of TerraSAR-X would also give better results but this is not available. If these information becomes available then using them to determine the areas facing the Sun, the Earth, and normal to the velocity vector, and using them as inputs in an optimal orbit determination scheme to estimate density is suggested as future work.

6.3.4 TanDEM-X

TanDEM-X (TerraSAR-X add on Digital Elevation Measurement) is a satellite that is flying in tandem with TerraSAR-X. This satellite is very similar to TerraSAR-X and more information can be found in Reference 81. Once the POE data are available from GFZ for TanDEM-X, the POE derived densities along its trajectory could be calculated. Since neither

TerraSAR-X nor TanDEM-X have accelerometers onboard, comparing the POE derived density between these two would yield interesting results since they are at the same altitude and flying in formation.

6.3.5 Estimating Drag Coefficient for TerraSAR-X and ICESat

Even though a rough estimate of drag coefficient for TerraSAR-X was used in this research, an improved estimate needs to be used in the future. An accurate estimate of drag coefficient for ICESat is certainly required and should be a function of beta angle since the attitude of ICESat is a function of the beta angle as well. This drag coefficient should also account for the rotation of solar panels as they track the Sun in their orbit.

6.3.6 ANDE

Atmospheric Neutral Density Experiment (ANDE) is a pair of twin spherical satellites launched on July 30, 2009, whose mission is specifically designed to study the thermospheric neutral density at an altitude of 350 km. Information about this satellite and the mission is from Reference 82. This mission is handled by the United States Naval Research Laboratory (NRL). One of the satellites is active (named Castor) and the other is passive (named Pollux), both of which are fitted with retroreflectors so that they can be tracked by satellite laser ranging. Pollux reentered soon after its last observation on March 28, 2010. Castor also has GPS and instruments to measure ion and neutral winds and temperature, internal and skin temperature, and electron density and temperature. One of the main scientific objectives is to measure total atmospheric density. Once the POE data are available, they can be used as measurements in an optimal orbit determination scheme to obtain POE derived densities, which can then be compared with density measured by the satellites (and perhaps published or made available to

academic research by NRL). The fact that these are spherical satellites greatly simplifies the drag coefficient calculation.

REFERENCES

1. S. Bruinsma and R. Biancale, "Total Density Retrieval with STAR," *First CHAMP Mission Results for Gravity, Magnetic and Atmospheric Studies*, eds. C. Reigber, H. Luhr, P. Schwintzer, Springer, Berlin, 2003, pp. 192-199.
2. R. S. Nerem, J. M. Forbes, E. K. Sutton, and S. Bruinsma, "Atmospheric Density Measurements Derived from CHAMP/STAR Accelerometer Data," *Advances in the Astronautical Sciences*, Vol. 116, AAS 03-621, Univelt, 2003, pp. 1879-1898.
3. B. D. Tapley, J. C. Ries, S. Bettadpur, M. Cheng, "Neutral Density Measurements from the Gravity Recovery and Climate Experiment Accelerometers," *Journal of Spacecraft and Rockets*, Vol. 44, No. 6, 2007, pp. 1220-1225.
4. D. A. Vallado, *Fundamentals of Astrodynamics and Applications*, Microcosm Press, El Segundo, CA, 3rd Edition, 2007.
5. A. C. Tribble, *The Space Environment: Implications for Spacecraft Design*, Princeton University Press, Princeton, New Jersey, 2003.
6. D. D. Knipp, *Understanding Space Weather and the Physics Behind It*, The McGraw-Hill Companies, Inc., U.S.A, 2011.
7. C. A. McLaughlin, "Upper Atmospheric Phenomena and Satellite Drag," *Advances in the Astronautical Sciences*, Vol. 123, AAS 05-315, Univelt, 2005, pp. 989-996.
8. L. G. Jacchia, *Revised Static Models for the Thermosphere and Exosphere with Empirical Temperature Profiles*, SAO Special Report No. 332, Smithsonian Institution Astrophysical Observatory, Cambridge, MA, 1971.
9. C. E. Roberts, Jr., "An Analytic Model for Upper Atmosphere Densities Based upon Jacchia's 1970 Models," *Celestial Mechanics*, Vol. 4, Issue 3-4, December 1971, pp. 368-377.
10. COSPAR Working Group IV, *COSPAR International Reference Atmosphere*, Akademie-Verlag, Berlin, 1972.
11. A. E. Hedin, "Extension of the MSIS Thermosphere Model into the Middle and Lower Atmosphere," *Journal of Geophysical Research*, Vol. 96, 1991, pp. 1159-1172.

12. J.M. Picone, A. E. Hedin, D. P. Drob, "NRLMSISE-00 Empirical Model of the Atmosphere: Statistical Comparisons and Scientific Issues," *Journal of Geophysical Research*, Vol. 107, No. A12, 2002.

13. B. R. Bowman, W. K. Tobiska, F. A. Marcos, C. Valladares, "The JB2006 empirical thermospheric density model," *Journal of Atmospheric and Solar-Terrestrial Physics* 70 (2008) 774-793, Elsevier Publications.

14. B. R. Bowman, W. K. Tobiska, F. A. Marcos, C. Y. Huang, C. S. Lin, W. J. Burke, "A New Empirical Thermospheric Density Model JB2008 Using New Solar and Geomagnetic Indices," AIAA 2008-6438, *AIAA/AAS Astrodynamics Specialist Conference*, Honolulu, HI, August 2008.

15. G. V. Groves, "Seasonal and Latitudinal Models of Atmospheric Temperature, Pressure and Density, 25 to 100 km," AFCRL-70-0261, 1970.

16. M. F. Storz, B. R. Bowman, Major J. I. Branson, S. J. Casali, and W. K. Tobiska, "High Accuracy Satellite Drag Model (HASDM)," *Advances in Space Research*, Vol. 36, Issue 12, 2005, pp. 2497-2505.

17. B. Bowman, F. A. Marcos, and M. J. Kendra, "A Method for Computing Accurate Atmospheric Density Values from Satellite Drag Data," *Advances in the Astronautical Sciences*, Vol. 119, AAS 04-173, Univelt, 2004, pp. 1117-1134.

18. B. Bowman, "The Semiannual Thermospheric Density Variation from 1970 to 2002 Between 200-1100 km," *Advances in the Astronautical Sciences*, Vol. 119, AAS 04-174, Univelt, 2004, pp. 1135-1154.

19. P. J. Cefola, R. J. Proulx, A. I. Nazarenko, and V. S. Yurasov, "Atmospheric Density Correction Using Two Line Element Sets as the Observation Data," *Advances in the Astronautical Sciences*, Vol. 116, AAS 03-626, Univelt, 2003, pp. 1953-1978.

20. V. S. Yurasov, A. I. Nazarenko, P. J. Cefola, and K. T. Alfriend, "Results and Issues of Atmospheric Density Correction," *Journal of the Astronautical Sciences*, Vol. 52, No. 3, July-September 2004, pp. 281-300.

21. V. S. Yurasov, A. I. Nazarenko, K. T. Alfriend, and P. J. Cefola, "Reentry Time Prediction Using Atmospheric Density Corrections," *Journal of Guidance, Control, and Dynamics*, Vol. 31, No. 2, March-April 2008, pp. 282-289.

22. M. P. Wilkins, C. A. Sabol, P. J. Cefola, and K. T. Alfriend, "Improving Dynamic Calibration of the Atmosphere," *Advances in the Astronautical Sciences*, Vol. 127, AAS 07-185, Univelt, 2007, pp. 1257-1272.

23. M. P. Wilkins, C. A. Sabol, P. J. Cefola, and K. T. Alfriend, "Validation and Application of Corrections to the NRLMSISE-00 Atmospheric Density Model," *Advances in the Astronautical Sciences*, Vol. 127, AAS 07-189, Univelt, 2007, pp. 1285-1304.

24. M. P. Wilkins, C. A. Sabol, P. J. Cefola, and K. T. Alfriend, "Practical Challenges in Implementing Atmospheric Density Corrections to the NRLMSISE-00 Model," *Advances in the Astronautical Sciences*, Vol. 124, AAS 06-170, Univelt 2006, pp. 1113-1130.

25. S. R. Mance, C. A. McLaughlin, F. G. Lemoine, D. D. Rowlands, and P. J. Cefola, "GEOSAT Follow-On Precision Orbit Improvement Through Drag Model Update," *Advances in the Astronautical Sciences*, Vol. 134, AAS 09-105, Univelt, 2009, pp. 43-62.

26. E. Doornbos, H. Klinkrad, and P. Visser, "Use of Two-Line Element Data for Thermosphere Neutral Density Model Calibration," *Advances in Space Research*, Vol. 41, 2008, pp. 1115-1122.

27. E. A. Rhoden, J. M. Forbes, and F. A. Marcos, "The Influence of Geomagnetic and Solar Variability on Lower Thermospheric Density," *Journal of Atmospheric and Solar-Terrestrial Physics*, Vol. 62, 2000, pp. 999-1013.

28. R. Konig and K. H. Neumayer, "Thermospheric Events in CHAMP Precise Orbit Determination," *First CHAMP Mission Results for Gravity, Magnetic and Atmospheric Studies*, eds. C. Reigber, H. Luhr, P. Schwintzer, Springer, Berlin, 2003, pp. 112-119.

29. S. Bruinsma and R. Biancale, "Total Densities Derived from Accelerometer Data," *Journal of Spacecraft and Rockets*, Vol. 40, No. 2, March-April 2003, pp. 230-236.

30. S. Bruinsma, S. D. Tamagnan and R. Biancale, "Atmospheric Densities Derived from CHAMP/STAR Accelerometer Observations," *Planetary and Space Science*, Vol. 52, 2004, pp. 297-312.

31. S. Bruinsma, and G. Thuillier, "The DTM-2000 empirical thermosphere model with new data assimilation and constraints at lower boundary: accuracy and properties," *Journal of Atmospheric and Solar Terrestrial Physics*, Vol. 65, 2003, pp. 1053-1070.

32. C. Berger, R. Biancale, M. Ill, F. Barlier, 1998. Improvement of the empirical thermospheric model DTM: DTM94-comparative review on various temporal variations and prospects in space geodesy applications. J. Geod. 72, 161–178.

33. A. E. Hedin, "MSIS-86 Thermospheric Model," *Journal of Geophysical Research,* Vol. 92, NO. A5, May 1987, pp. 4649-4662.

34. E. Doornbos, H. Klinkrad, and P. Visser, "Atmospheric Density Calibration Using Satellite Drag Observations," *Advances in Space Research,* Vol. 36, 2005, pp. 515-521.

35. J. van den Ijssel, P. Visser, and R. Haagmans, "Determination of Non-Conservative Accelerations from Orbit Analysis," *Earth Observation with CHAMP Results from Three Years in Orbit,* eds. C. Reigber, H. Luhr, P. Schwintzer, J. Wickert, Springer, Berlin, 2005, pp. 95-100.

36. J. van den IJssel and P. Visser, "Determination of Non-Gravitational Accelerations from GPS Satellite-to-Satellite Tracking of CHAMP," *Advances in Space Research,* Vol. 36, 2005, pp. 418-423.

37. J. van den IJssel and P. Visser, "Performance of GPS Accelerometry: CHAMP and GRACE," *Advances in Space Research,* Vol. 39, 2007, pp. 1597-1603.

38. O. Montenbruck, T. van Helleputte, R. Kroes, and E. Gill, "Reduced Dynamic Orbit Determination Using GPS Code and Carrier Measurements," *Aerospace Science and Technology,* Vol. 9, 2005, pp. 261-271.

39. C. A. McLaughlin and B. S. Bieber, "Neutral Density Determined from CHAMP Precision Orbits," *Advances in the Astronautical Sciences,* Vol. 129, AAS 07-260, Univelt, 2008, pp. 167-186.

40. C. A. McLaughlin, A. Hiatt, and B. S. Bieber, "Comparison of Total Density Derived from CHAMP Precision Orbits and CHAMP Accelerometer," *Advances in the Astronautical Sciences,* Vol. 130, AAS 08-177, Univelt, 2008, pp. 1193-1206.

41. C. A. McLaughlin, A. Hiatt, T. Lechtenberg, "Precision Orbit Derived Total Density," *Journal of Spacecraft and Rockets,* Vol. 48, No.1, January-February 2011, pp. 166-174.

42. A. Hiatt, C. A. McLaughlin, and T. Lechtenberg, "Deriving Density Estimates Using CHAMP Precision Orbit Data for Periods of High Solar Activity," *Advances in the Astronautical Sciences,* Vol. 134, AAS 09-104, Univelt, 2009, pp. 23-42.

43. A. Hiatt, “Deriving Atmospheric Density Estimates Using Satellite Precision Orbit Ephemerides,” M.S. Thesis, University of Kansas, 2009.

44. T. Lechtenberg, “Derivation and Observability of Upper Atmospheric Density Variations Utilizing Precision Orbit Ephemerides,” M.S. Thesis, University of Kansas, 2010.

45. Infoterra GmbH, “TerraSAR-X: First Commercial 1m Radar Satellite,” 2010, Last Accessed: April 10, 2010, http://terrasar.de/terrasar-x.html.

46. E. Fattig, C. A. McLaughlin, T. Lechtenberg, “Comparison of Density Estimation for CHAMP and GRACE Satellites,” AIAA 2010-7976, *2010 AIAA/AAS Astrodynamics Specialist Conference and Exhibit*, Toronto, ON, CA, August 2010.

47. C. A. McLaughlin, T. Lechtenberg, E. Fattig, “Estimating Density Using Precision Satellite Orbits From Multiple Satellites,” Astrodynamics 2010, Vol. 139 of *Advances in the Astronautical Sciences*, 2010, AAS 10-307, pp. 3229-3246

48. E. Fattig, “Comparison of Precision Orbit Derived Density Estimates for CHAMP and GRACE Satellites,” M.S. Thesis, University of Kansas, 2011.

49. C. A. McLaughlin, E. Fattig, D. Mysore Krishna, T. Locke, and P. M. Mehta, "Time Periods of Anomalous Density for GRACE and CHAMP,” Astrodynamics 2011, Vol. 142 of *Advances in the Astronautical Sciences*, 2011, AAS 11-613, pp. 3299-3310.

50. A. K. Arudra, “Atmospheric Density Estimation Using Satellite Precision Orbit Ephemeride,” M.S. Thesis, University of Kansas, 2011.

51. Mysore Krishna, D. and C. A. McLaughlin, “Combining Precision Orbit Derived Density Estimates,” Astrodynamics 2011, Vol. 142 of *Advances in the Astronautical Sciences*, 2011, AAS 11-475, pp. 3229-3246.

52. J. Kim, “Bridging methods for the JB2006 and NRLMSISE-00 thermospheric density models in the altitude range of 140 km through 200 km,” M. S. Thesis, Department of Aerospace Engineering, Pennsylvania State University, August, 2008.

53. J. Kim, D. B. Spencer, T. J. Kane, J. Urbina, "A blending technique in thermospheric density modeling,” AIAA/AAS Astrodynamics Specialist Conference and Exhibit, AIAA, Honolulu, Hawaii, 18-19 August, 2008.

54. J. Kim, D. B. Spencer, T. J. Kane, J. Urbina, "Thermospheric density model blending techniques: Bridging the gap between satellites and sounding rockets," Radio Science, Vol. 44, RSO 22, 2009.

55. B. D. Tapley, B. E. Schutz, and G. H. Born, *Statistical Orbit Determination*, Elsevier Academic Press, Amsterdam, 2004.

56. J. R. Wright, "Real-Time Estimation of Local Atmospheric Density," *Advances in the Astronautical Sciences*, Vol. 114, AAS 03-164, Univelt, 2003, pp. 927-950.

57. J. R. Wright and J. Woodburn, "Simultaneous Real-Time Estimation of Atmospheric Density and Ballistic Coefficient," *Advances in the Astronautical Sciences*, Vol. 119, AAS 04-175, Univelt, 2004, pp. 1155-1184.

58. C. A. McLaughlin, A. Hiatt, E. Fattig and T. Lechtenberg, "Ballistic Coefficient and Density Estimation," *Advances in Astronautical Sciences*, Vol. 134, AAS 09-439, Univelt, 2009, pp23-42.

59. P. M. Mehta., and C. A. McLaughlin., "Density and Ballistic Coefficient Estimation Revisited," Astrodynamics 2011, Vol. 142 of *Advances in the Astronautical Sciences*, 2011, AAS 11-609, pp. 3247-3264.

60. Torrence, M., "CHAMP," CHAMP Satellite Information, NASA, Last Accessed: February 1, 2012, http://ilrs.gsfc.nasa.gov/satellite_missions/list_of_satellites/cham_general.html.

61. Torrence, M., "GRACE-A, -B," GRACE-A Satellite Information, NASA, Last Accessed: February 1, 2012, http://ilrs.gsfc.nasa.gov/satellite_missions/list_of_satellites/graa_general.html.

62. Torrence, M., "TerraSAR-X," TerraSAR-X Satellite Information, NASA, Last Accessed: February 1, 2012, http://ilrs.gsfc.nasa.gov/satellite_missions/list_of_satellites/tsar_general.html.

63. Torrence, M., "ICESat," ICESat Satellite Information, NASA, Last Accessed: February 1, 2012, http://ilrs.gsfc.nasa.gov/satellite_missions/list_of_satellites/ices_general.html.

64. R. Konig, S. Zhu, C. Reigber, K. H. Neumayer, H. Meixner, R. Galas, G. Baustert, "CHAMP Rapid Orbit Determination for GPS Atmospheric Limb Sounding," *Advances in Space Research*, Vol. 30, No. 2, 2002, pp. 289-293.

65. G. Michalak, G. Baustert, R. Konig, C. Reigber, "CHAMP Rapid Science Orbit Determination: Status and Future Prospects," *First CHAMP Mission Results for Gravity, Magnetic and Atmospheric Studies*, eds. C. Reigber, H. Luhr, P. Schwintzer, Springer, Berlin, 2003, pp. 98-103

66. R. Konig, G. Michalak, K. H. Neumayer, S. Y. Zhu, H. Meixner, C. Reigber, "Recent Developments in CHAMP Orbit Determination at GFZ," *Earth Observation with CHAMP Results from Three Years in Orbit*, eds. C. Reigber, H. Luhr, P. Schwintzer, J. Wickert, Springer, Berlin, 2005, pp. 65-70.

67. R. Konig, G. Michalak, K. H. Neumayer, S. Zhu, "Remarks on CHAMP Orbit Products," *Observation of the Earth System from Space*, eds. J. Flury, R. Rummel, C. Reigber, M. Rothacher, G. Boedecker, U. Schreiber, Springer, Berlin, 2006, pp. 17-26

68. O. Montenbruck and E. Gill, *Satellite Orbits: Models, Methods, and Applications*, Springer-Verlag, Berlin, 2001.

69. J. R. Wright, "Optimal Orbit Determination," *Advances in the Astronautical Sciences*, Vol. 112, AAS 02-192, Univelt, 2002, pp. 1123-1134, http://www.agi.com/downloads/support/productSupport/literature/pdfs/whitePapers/optimal_od.pdf.

70. Analytical Graphics, Inc., "Orbit Determination Tool Kit Help," *Orbit Determination Tool Kit*, Version 5.1.3.

71. J. R. Wright, "Orbit Determination Tool Kit Theorems and Algorithms," *Analytical Graphics, Inc.*, 2007.

72. D. A. Vallado., R. S. Hujsak., T. M. Johnson., J. H. Seago., and J. W. Woodburn., "Orbit Determination Using ODTK Version 6," *European Space Astronomy Center (ESA/ESAC)*, Madrid, Spain, May 2010.

73. S. Tanygin, J. R. Wright "Removal of Arbitrary Discontinuities in Atmospheric Density Modeling*," Advances in the Astronautical Sciences,* Vol. 119 II, AAS 04-175, Univelt, 2004, pp. 1185-1196.

74. B. R. Bowman, F. A. Marcos, K. Moe, M. M. Moe, "Determination of Drag Coefficient Values for CHAMP and GRACE Satellites Using Orbit Drag Analysis," *Advances in the Astronautical Sciences*, Vol. 129, AAS 07-259, Univelt, 2008, pp. 147-166.

75. P. Bourke, “Cross Correlation,” August 1996, Last Accessed: February 20, 2011, http://local.wasp.uwa.edu.au/~pbourke/miscellaneous/correlate/.

76. Anon., “TerraSAR-X–Germany’s radar eye in space, German Aerospace Center (DLR), Last Accessed: August 18, 2011, http://www.dlr.de/eo/en/desktopdefault.aspx/tabid-5725/9296_read-15979/.

77. Personal correspondence with Dr. Reinhard Wolders, AED7, ASTRIUM: An EADS Company, November 16, 2010.

78. C. E. Webb, “Radiation Force Modeling for ICESat Precision Orbit Determination,” PhD Dissertation, Department of Aerospace Engineering, The University of Texas at Austin, May, 2007.

79. Anon., “ICESat/GLAS,” Center for Space Research, University of Texas, NASA Goddard, Greenbelt, MD, Last Accessed: March 20, 2012, http://www.csr.utexas.edu/glas/

80. L. H. Sentman, "Free molecule flow theory and its application to the determination of aerodynamic forces,” *Lockheed Missile and Space Co.*, LMSC-448514, AD 265-409, Sunnyvale, CA, 1961.

81. Torrence, M., “TanDEM-X,” TanDEM-X Satellite Information, NASA, Last Accessed: February 1, 2012, http://ilrs.gsfc.nasa.gov/satellite_missions/list_of_satellites/tand_general.html

82. Noll, C., “ANDE,” ANDE Satellite Information, NASA, Last Accessed: February 1, 2012, http://ilrs.gsfc.nasa.gov/satellite_missions/list_of_satellites/andp_general.html.